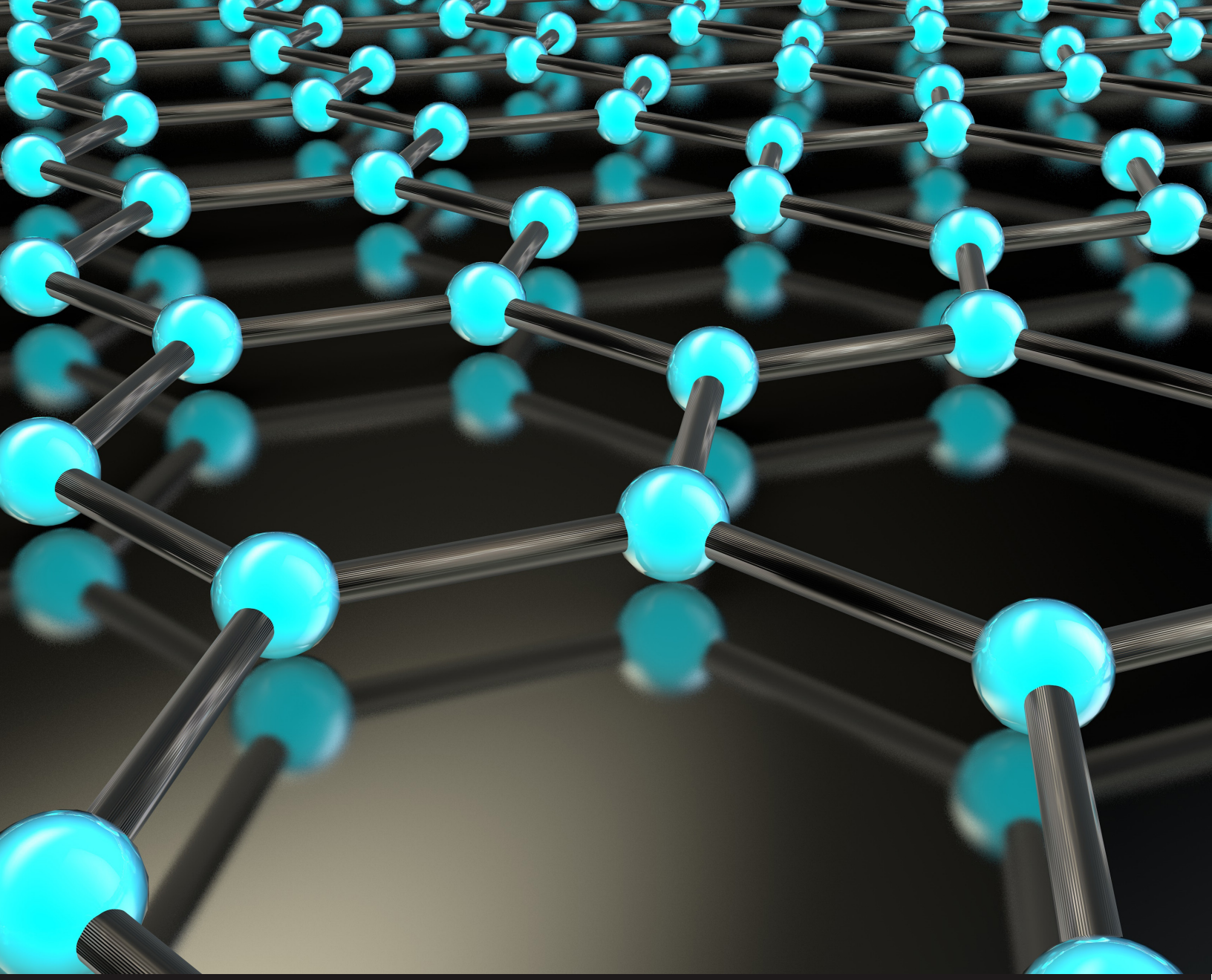

Unlocking the Mysteries of Complex Nanoscale Systems

ARTICLE COLLECTION

WILEY Analytical Science

Sponsored by:

BRUKER

Comprehensive Nanomechanical and Nanoelectrical Research

Bruker's Dimension XR scanning probe microscope (SPM) systems incorporate decades of research and technological innovation to deliver the utmost performance, functionality, and capability in nanoscale investigation. The extreme research (XR) family of SPMs for FastScan® and Icon® AFM platforms provides unique packaged solutions for nanomechanical, nanoelectrical, and nanoelectrochemical characterization.

Quantification of materials in air, fluid, and electrical or chemically reactive environments has never been easier:

- Correlate nanomechanics characterization to bulk DMA and nanoindentation with **NEW** AFM-nDMA mode
- Correlate electrical spectra in every pixel to mechanical property measurements with **NEW** DataCube modes

Your research deserves the very best that AFM technology has to offer!

Visit www.bruker.com/DimensionXR, email productinfo@bruker.com or call +1.805.967.1400 for more information.

Contents

Introduction

Analysis of complex systems at the nanoscale is an ever-growing area of research. Nanoscale systems are extremely small, often measuring less than 100 nanometers in size and yet the amount of new information being uncovered at that scale is vast. Specialized techniques and technologies are giving researchers the tools to uncover and better understand these systems in the development and utilization of advanced materials.

One approach to analyzing complex systems at the nanoscale uses nanomechanical testing equipment within electron microscopes. These systems typically perform mechanical tests, such as indentation, scratch, and tensile at the nanoscale within a scanning electron microscope (SEM) or transmission electron microscope (TEM) where temperature and pressure can be carefully controlled. Another useful technique is atomic force microscopy (AFM), which uses a tiny cantilever to measure the force between the sample and the tip of the cantilever, allowing for the analysis of surface topography, material properties, and chemical interactions. AFM can also be combined with spectroscopy (commonly known as AFM-IR), which involves the use of light to quantitatively study the structure, composition, and properties of molecules. In this regard, AFM and combined techniques are powerful tools for studying the structure of nanoscale systems.

This article collection begins with a study on a new method for creating 3D helical plasmonic nanostructures from 2D plasmene nanosheets. The process involves a micro-spatula-based strategy to scrape substrate-supported plasmene, which forms various complex helical nanostructures with controlled dimensions. Additionally, Shi, Q. et al. (2023) describe how FIB-based lithography on free-standing plasmene produces 3D nanospirals.

Next, Panchal, V. et al. (2022) report two precision nanomechanical characterization techniques, AFM-based PeakForce quantitative nanomechanical mapping and nanoindentation-based dynamical mechanical analysis, which are used to compare the modulus and viscoelastic properties of organic polymers used in organic electronics.

Rejhon, M. et al. (2023) shows that epitaxial graphene films grown on silicon carbide can significantly increase the hardness and yield point of the material. At low to high loads, the hardness of the material increases up to 100% and 30%, respectively. Even at deep indentations of 175 nm, the hardness of the material increases by up to 30%. The increase in mechanical properties is explained by the formation of a sp3 diamene structure under pressure.

Peña-Alcántara, A. et al. (2023) discusses the use of a polymer semiconductor/elastomer blend to create mechanically stretchable electronic devices with high fracture strain. The effects of the molecular weight of both the polymer and elastomer on the blend morphology, and mechanical, and electrical properties are explored. AFM-based nanomechanical images are used to gain a better understanding of the blend film morphology. Results from the blend films show a maximum strain at fracture of 640% ± 20%. This study provides insight into appropriate polymer selections for stretchable semiconducting thin films that possess excellent mechanical and electrical properties.

Finally, Nguyen, C.-P. T. et al. (2023) discusses the nanomechanical properties of domain walls in lead titanate ($PbTiO_3$), a prototypical ferroelectric material. Using atomic force microscopy (AFM)-based methods, researchers found variations in elastic moduli in the area around the 90° domain walls extending up to 100 nm into the adjacent domains. They also found local domain wall hardness and plastic and elastic deformation energies.

Overall, the analysis of complex systems on the nanoscale is an ever-evolving field. New technologies and techniques are being developed to study these systems, allowing for greater insight into their structure and behavior. As research continues, our understanding of nanoscale systems will grow, leading to new applications and discoveries.

Through the methods and applications presented in this article collection, we hope to share some of the research and discoveries that today's advanced technologies and techniques are making in the world of complex nanoscale systems. For more information, we encourage you to visit Bruker to learn more and explore options to enhance your research.

Róisín Murtagh
Editor at Wiley Analytical Science

References

Shi, Q., Dong, D., Gervinskas, G., Lin, H., Sikdar, D., Jia, B., Walia, S., Sriram, S., Bhaskaran, M., Yap, L. W., Cheng, W., Soft Plasmene Helical Nanostructures. *Adv. Mater. Technol.* 2023, 2201866. https://doi.org/10.1002/admt.202201866

Panchal, V., Dobryden, I., Hangen, U. D., Simatos, D., Spalek, L. J., Jacobs, I. E., Schweicher, G., Claesson, P. M., Venkateshvaran, D., Mechanical Properties of Organic Electronic Polymers on the Nanoscale. *Adv. Electron. Mater.* 2022, 8, 2101019. https://doi.org/10.1002/aelm.202101019

Rejhon, M., Zhou, X., Lavini, F., Zanut, A., Popovich, F., Schellack, L., Witek, L., Coelho, P., Kunc, J., Riedo, E., Giant Increase of Hardness in Silicon Carbide by Metastable Single Layer Diamond-Like Coating. *Adv. Sci.* 2023, 10, 2204562. https://doi.org/10.1002/advs.202204562

Peña-Alcántara, A., Nikzad, S., Michalek, L., Prine, N., Wang, Y., Gong, H., Ponte, E., Schneider, S., Wu, Y., Root, S. E., He, M., Tok, J. B., Gu, X., Bao, Z., Effect of Molecular Weight on the Morphology of a Polymer Semiconductor–Thermoplastic Elastomer Blend. *Adv. Electron. Mater.* 2023, 2201055. https://doi.org/10.1002/aelm.202201055

Nguyen, C.-P. T., Schoenherr, P., Seidel, J., Intrinsic Mechanical Compliance of 90° Domain Walls in PbTiO3. *Adv. Funct. Mater.* 2023, 33, 2211906. https://doi.org/10.1002/adfm.202211906

ADVANCED MATERIALS TECHNOLOGIES
www.advmattechnol.de

Soft Plasmene Helical Nanostructures

*Qianqian Shi, Dashen Dong, Gediminas Gervinskas, Han Lin, Debabrata Sikdar, Baohua Jia, Sumeet Walia, Sharath Sriram, Madhu Bhaskaran, Lim Wei Yap, and Wenlong Cheng**

Plasmene is recently defined as 2D arrays of plasmonic nanoparticles, which could be fabricated by the bottom-up self-assembly approach and demonstrated a wide range of applications in sensing, energy harvesting, nanophotonics and encryption. Here, this work further demonstrates a 3D helical plasmonic nanostructures that can be fabricated from 2D plasmene nanosheet. Inspired by chocolate curls-making process, a micro-spatula-based strategy is developed to selectively scrape substrate-supported plasmene to free space, which spontaneously folds the plasmene nanosheet into various complex helical nanostructures with controlled dimensions. 3D nanospirals can also be obtained by focus ion beam (FIB)-based lithography on free-standing plasmene. Helical plasmene structures are robust, exhibiting elastic mechanical properties and chiral optical response. This methodology represents a versatile fabrication route combining both bottom-up and top-down approaches to create soft plasmonic helical structures for potential applications in next-generation flexible nanophotonic devices.

1. Introduction

Plasmene, a 2D monolayer nanosheet assembled from constituent plasmonic nanoparticle building blocks, was introduced by our research group back in 2014.[1–3] It is a new class of advanced materials combining tailorable organic ligands and inorganic building blocks that can be finely tuned with arbitrary size and shapes,[4] demonstrating unique structure-dependent properties such as gap-depended plasmonics,[1] n-doping or p-doping like properties,[5] transmutable optical and structural properties,[6] asymmetrical ion transport properties,[7] and inter/intra-plasmonic coupling.[8] While a focused ion beam (FIB) is able to program milling sites and milling depths precisely to obtain several 3D plasmene origami structures,[1,9] helical plasmonic structures have not yet been achieved.

On the other hand, helical structures from plasmonic nanomaterials have recently attracted intense research due to their unique chiral optical properties.[10–16] For instance, a gold helix square lattice can block the circular polarization with the same handedness as the helices while transmit the other.[11] Hybrid nanoscrolls from MoS_2 or WS_2 and plasmonic Ag nanoparticles exhibited up to 500 times

Q. Shi, D. Dong, L. W. Yap, W. Cheng
Department of Chemical & Biological Engineering
Faculty of Engineering
Monash University
Clayton, Victoria 3800, Australia
E-mail: Wenlong.cheng@monash.edu

D. Dong, S. Walia, S. Sriram, M. Bhaskaran
Functional Materials and Microsystems Research Group
and the Micro Nano Research Facility
RMIT University
Melbourne, Victoria 3001, Australia

D. Dong, S. Walia, S. Sriram, M. Bhaskaran
School of Engineering
RMIT University
Melbourne, Victoria 3001, Australia

The ORCID identification number(s) for the author(s) of this article can be found under https://doi.org/10.1002/admt.202201866.

DOI: 10.1002/admt.202201866

G. Gervinskas
Monash Ramaciotti Centre for Cryo-Electron Microscopy
Monash University
Clayton, Victoria 3800, Australia

H. Lin, B. Jia
School of Science
RMIT University
Melbourne, Victoria 3000, Australia

H. Lin, B. Jia
The Australian Research Council (ARC) Industrial Transformation Training
Centre in Surface Engineering for Advanced Materials (SEAM)
RMIT University
Melbourne, Victoria 3000, Australia

D. Sikdar
Department of Electronics and Electrical Engineering
Indian Institute of Technology Guwahati
Guwahati 781039, India

S. Sriram, M. Bhaskaran
ARC Centre of Excellence for Transformative Meta-Optical Systems
RMIT University
Melbourne, Victoria 3000, Australia

increased photosensitivities in comparison with the normal nanosheets.[16] Using DNA origami as a template, it has been reported that a 3D helix structure from AuNPs-tubular DNA origami showed controllable optical chirality.[15]

It is noteworthy to mention that the reported state-of-the art methods to fabricate these complex 3D plasmonic helical structures are heavily rely on top-down lithography[11,17–23] and bottom-up self-assembly.[15,16,24–31] The former may enable well-defined 3D structures, but it often involves multiple materials, complex processing methods, and/or requires additional sacrificial layers; while the latter typically leads to chiral plasmonic structures in solution with finely adjustable internal structural programming by the virtue of specific molecules or biomolecules, but often suffers poor control over the overall structures.

Here, we report a chocolate curl-inspired approach to fabricate different 3D helical kirigami (a 3D designed structure from "cutting" and "folding" a 2D material) simply by selectively micro-scraping silicon substrate-supported plasmene nanosheets. While this fabrication process does not involve any templates, sacrificial layers or chemicals, different nanoscale kirigami including helix, scrolls and 3D spiral could be obtained. In brief, a 2D plasmene was first fabricated on silicon substrate by our developed air-water interfacial self-assembly method.[1,3] Then, a chisel like micro-spatula with a flat and sharp end blade was carefully positioned at an oblique angle to the edge of plasmene nanosheet to scrape it with a controlled speed. This has led to spontaneous formation of chiral plasmonic nanostructures including helix and scrolls. The structural parameters of the resulting helical plasmonic kirigami, such as overall dimensions and shapes, could be tuned by controlling the nanosheet thickness, constituent building blocks, the scraping speed, and the motion of the micro-spatula. 3D nanospirals can be obtained by applying FIB-based lithography on free-standing plasmene nanosheet and subsequently manipulation with a micro-needle. The obtained nanohelix and 3D nanospiral displayed elastic mechanical properties in the compression and dragging tests, respectively. Furthermore, we observed chiral plasmonic response from a single helix with a reflectance dissymmetric factor (g_r) of 0.17 toward circularly polarized light (CPL) illumination.

2. Results and Discussion

2.1. Soft Plasmene Helix

Using gold nanocubes (Au NCs) as the model building blocks, we first prepared plasmene nanosheets on the silicon substrate by the air-water interfacial self-assembly following our previously reported protocol.[1,3] Briefly, Au NCs were synthesized by a seed-mediated method and functionalized with hydrophobic thiolated polystyrene (PS) via Au-S covalent bonding. The PS-capped Au NC chloroform solution was then dropped onto a sessile droplet sitting on the silicon substrate. Upon the full evaporation of chloroform and water, a continuous plasmene nanosheets formed as confirmed by scanning electron microscope (SEM) characterization (Figure S1, Supporting Information).

Next, a top-down micro-scraping lithography was used to selectively peeling off the bottom-up grown plasmene on silicon, as illustrated in (**Figure 1**a). To achieve this, a motor-controlled Picoprobe (PT-14-6705) tip was mounted inside a FEI Helios Nanolab FIB SEM chamber and the rounded Picoprobe tip was milled into a blade shape with a sharp edge. The Picoprobe blade-like tip was then positioned to the edge of plasmene nanosheet at an oblique angle (α in Figure 1a) to the supporting silicon (Figure S2, Supporting Information), simultaneously with the tip blade plane inclined at a small angle (β in Figure 1a) to the plasmene. By horizontally moving the stage along the *x*-axis, the plasmene nanosheets could be cut and peeled off from the supporting silicon substrate. This micro-scraping lithographic process led to the spontaneous formation of 3D plasmonic kirigami nanostructures such as helix (Figure 1b). By controlling the scraping distance, we could obtain plasmonic helix with the length ranging from~3–26 µm, as shown in Figure 1c. The helical structure fabrication is repeatable, as evidenced by numbers of helix replica using the same cutting parameters (Figure S3, Supporting Information).

We attributed the formation of nanohelix to the mechanical property of plasmene and the applied shear force during the oblique cutting process.[32,33] According to our previous report, plasmene has a Young's modulus of ≈1 GPa,[1] which endows it with strong mechanical strength for manipulation. In the initial state of cutting, the blade edge was inserted between the plasmene and the substrate, and caused a concentrated shear force on plasmene. This leads to a plastic deformation of plasmene in the primary deformation zone (insert in Figure 1a). As the tip moving forward, the co-existed chip–tool interface friction caused an additional shear force in the secondary deformation zone that is adjacent to the blade surface, which gave rise to a gradual deformation of the sheared plasmene. As a result, plasmene moved and curled continuously along the rake face as the micro-spatula moving forward, forming a chocolate curl-like nanostructure.[34]

It is worth mentioning that the blade edge was inclined at a small angle to the supporting substrate (β in Figure 1a), therefore, there are three forces in our system: cutting force (F_c), feed force (F_f), and radial force (F_r) (insert in Figure 1b).[35] The resulted force (F) can be represented by

$$F = \sqrt{F_c^2 + F_f^2 + F_r^2} \tag{1}$$

where the former two forces determine the length and diameter of the helix structure, while F_r determines the rolling direction of plasmene (γ), which leads to a helical shape flowed at sideways direction in Au NC plasmene.

We further applied the same oblique cutting technique to a Janus NC-star plasmene that was fabricated using a surface symmetry breaking method.[36] Interestingly, we observed the formation of larger scroll nanostructures (Video S1, Supporting Information), which differs from the nanohelix obtained from Au NC plasmene. SEM images of the fabricated nanoscrolls in top-view and tilted-view indicated a gradual number of layers increase from ½ to 5 as increasing scraping distance (Figure 1d).

The formation of large scroll nanostructures could be attributed to the shapes of plasmene-constituent building blocks, thickness and mechanical property of plasmenes, as well as the resulted force (F). Compared to Au NC plasmene, Janus

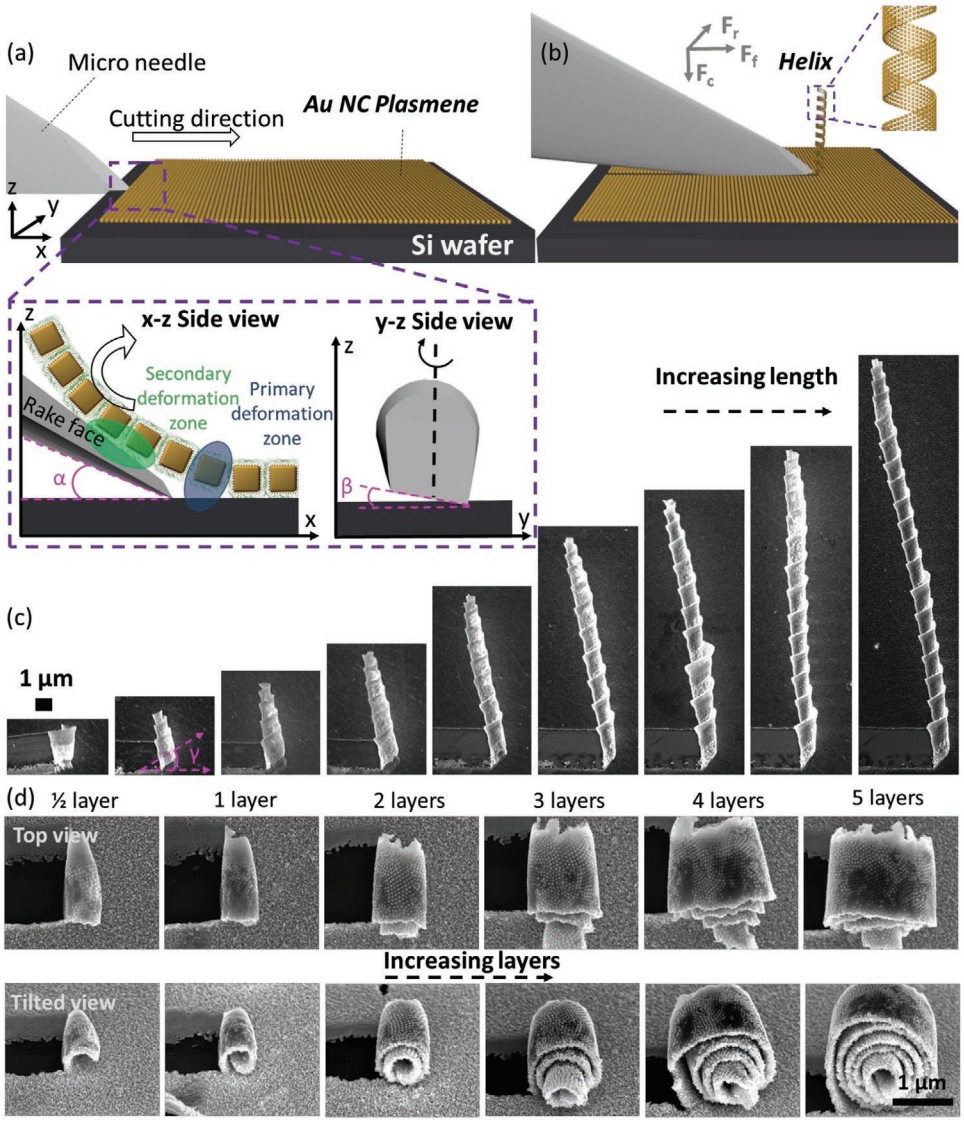

Figure 1. a,b) Schematic illustration of the fabrication of a plasmene helix via a micro-spatula-based strategy. Inserts represent the deformation process of a plasmene helix, and the side view of the micro-spatula blade in the *x*–*z* plane and *y*–*z* plane. The blade edge was initially parallel to the supporting silicon, but before mounting on the micro-manipulation stage, it was rotated clockwise along the axis of the blade to create an inclination angle β. SEM images of c) plasmene helix with increasing length and d) nanoscrolls with increasing numbers of layers.

NC-star plasmene has asymmetrical structure, larger thickness and greater roughness due to the nature of its unique building block morphology.[36] It is hypothesized that a larger radial force (F_r) or inclination angle β would be required for Janus NC-star plasmene to form helix structure. On the other hand, F_c, F_f, and F_r are in proportion to the cutting depth, in this case, the thickness of Janus NC-star plasmene.[35] An increased thickness gave rise to a higher F_c and F_f while thickness effect on F_r is minor in comparison to that on F_c and F_f due to the small inclination angle in our system. As a result, F_c and F_f played dominant roles in controlling the structure of chip, resulting scrolled structures with larger radius instead of helix.

We also observed such plasmene building blocks effect on helical structures (Figures S4 and S5, Supporting Information). Although helical nanostructures with similar rolling angle γ were managed to obtain by tuning the oblique cutting parameters (angle α and β), the radius of these helix were found to be different due to different shapes and sizes of the building block. Apart from the building block effect, the moving speed of the control stage was also found to affect the resulted force and control the overall structure of the chip (Figure S6 and Videos S2–S5, Supporting Information). In addition, our method also offers flexibility in positioning the micro-spatula at controlled locations and directions to "touch" and "capture" target objects on the plasmene surface (Figure S7 and Video S6, Supporting Information).

The handedness of the helical structures could be controlled by adjusting the angle β between the inclined tip edge and the plasmene (Figure S8, Supporting Information). We found that

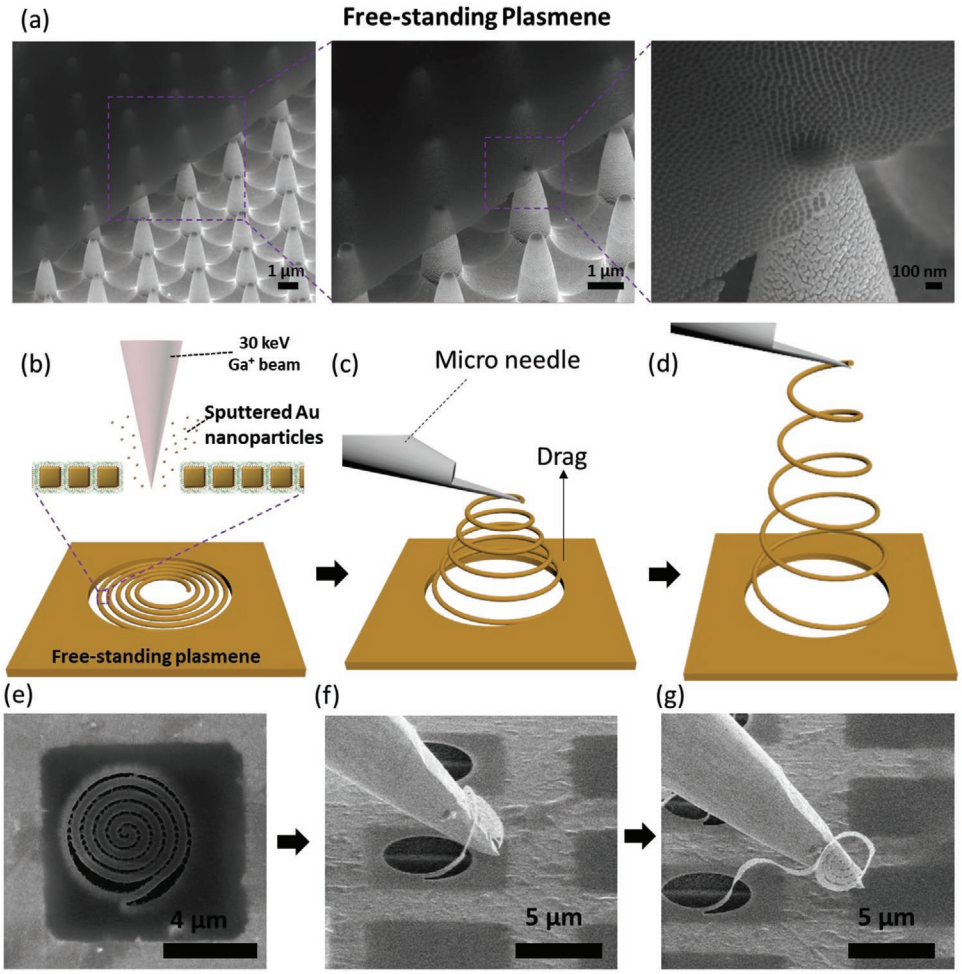

Figure 2. a) SEM images of a free-standing plasmene on an array of SiO_2 tips. Schematic illustration showing b) a spiral kirigami pattern on a free-standing plasmene and c,d) the dragging of a spiral kirigami using micro-needle. e–g) Corresponding SEM images of a spiral plasmene kirigami and dragging a soft plasmene spiral.

when the opening of inclined angle β toward the positive y-axis (with point A contacting plasmene, Figure S8, Supporting Information) and negative y-axis (with point B contacting plasmene, Figure S8, Supporting Information), left (Figures S3 and S5, Supporting Information) and right (Figure S6, Supporting Information) handedness of helical structures were typically obtained, respectively. This was due to the different direction of F_r, which determined the rolling direction of plasmene helicals.

2.2. Soft Plasmene 3D Nanospiral

The mechanical strength allows plasmene maintaining its structural integrity without any deformations/cracks even when being suspended over a substrate, such as an array of SiO_2 tips (**Figure 2**a). Inspired by the traditional Chinese paper-cutting art, we further produced soft plasmene 3D nanospiral from the free-standing plasmene by FIB-based lithography as illustrated in Figure 2b–d. In the first step, pre-designed areas of free-standing plasmene were selectively milled by exposing to high-energy gallium ion irradiation, giving a 2D kirigami pattern (Figure 2b). To prevent any structural distortion before applying mechanical force, the milling beam current and dwelling time were carefully controlled to ensure some residual connections between adjacent ribbons (Figure 2e). The obtained kirigami consists of spiral ribbons with a width of 0.36 ± 0.01 µm and a gap of 0.12 ± 0.02 µm, and an overall size of 5.6×5.2 µm. In the next step, a micro-needle with a sharp tip was used to pull the 2D spiral kirigami out of the plane (Figure 2c), forming a 3D nanospiral. Since one end of the free-standing plasmene was fixed, the tensile stress from the tip caused the kirigami to bend upward and be stretched as shown in Figure 2d. SEM images proved the successful fabrication of 2D spiral kirigami and its laterally stretching upon axial dragging by the needle (Figure 2e–g). We determined the relative length changes by analyzing SEM images recorded before and after micro-needle manipulation and found the soft plasmene spiral was stretched by ≈146%. This stretching process is reversible, which is evidenced by the Video S7, Supporting Information, indicating a spring-like elasticity of the obtained kirigami.

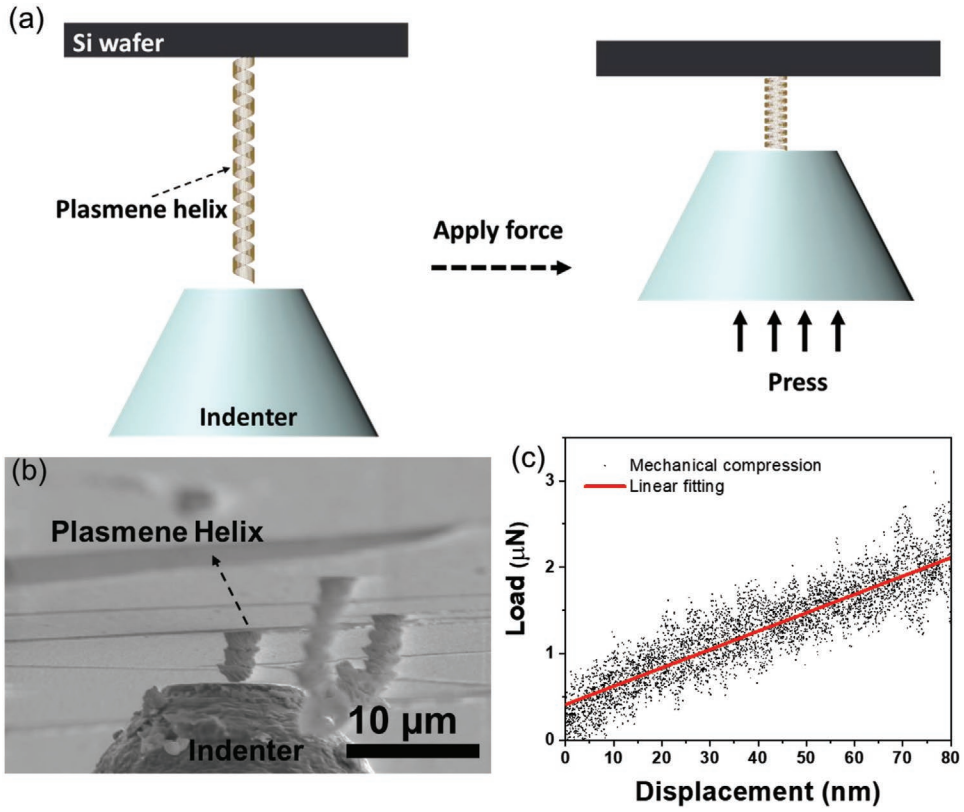

Figure 3. a) Schematic set-up of mechanical compression test on a standing plasmene helix. b) SEM image captured during the mechanical test. c) Load forces versus displacement curve for a standing plasmene helix (Au NCs were used as building blocks).

2.3. Elastic Properties of Plasmene Helix

To further measure the mechanical properties of the plasmene helix, we performed a mechanical compression test using an indenter that is positioned inside a SEM chamber. As shown in **Figure 3**a, one end of the standing plasmene helix was tethered to a silicon wafer while the other end floated freely. Then, the indenter slowly approached the free-floating end of the plasmene helix and compressed the entire 3D nanostructure. Initially, the helix was at a fully extended state and the indenter was at zero deflection, therefore the loading force is zero. Upon compression, the helix began to undergo shape change (Figure 3b) and yielded a gradual increasing force on the order of a few micronewtons (Figure 3c). We quantified the helix deformational parameters by exploiting SEM image captured during the mechanical test. The experimental result showed a linear relationship between loading force and displacement, following the known Hooke's law. The elastic coefficient of the particular standing helix was estimated to be 21.23 N m^{-1}, which further confirmed a spring like elasticity of the helical plasmene nanostructures.

2.4. Chiral Optical Properties of Plasmene Helix

We further characterized the optical chirality of the plasmene helix. The far-field optical response of a 14.8 μm standing helix (**Figure 4**a) was recorded by measuring the reflectance of CPL using an FTIR system (Bruker Vertex 70) connected to a microscope (Bruker Hyperion 2000). As shown in Figure S9, Supporting Information, the unpolarized light first passed through a linear polarizer and converted into linearly polarized light, and then traveled through a quarter waveplate and decomposed into right-handed circularly polarized (RCP) and left-handed circularly polarized (LCP) light, and finally reached the standing helix.

Figure 4b shows the reflectance spectra of a standing Au NC plasmene helix under LCP (red) and RCP (blue) illumination. Clearly, the helical structure exhibited distinct chiroptical response for LCP and RCP in the spectral range between 1.5 and 8.5 μm. Numerical simulation also confirms the differences in optical response of an Au NC plasmene helix under LCP and RCP illumination. Figure S10, Supporting Information, shows the full-wavelength simulations of an individual free-standing Au NC plasmene helix. Due to emulating the experimental setup for reflectance measurement is computationally intensive with high complexity, a transmittance spectrum is numerically simulated instead. Nevertheless, the chiral properties are well observed in the simple transmittance spectrum of a free-standing plasmene helix. Dissymmetric factor g, which represents the sensitivity of a material toward CPL, is normally defined by $g = \frac{2\Delta I}{I_L + I_r}$, where I is the intensity of the optical signal. Here, we use the reflectance intensity to calculate the reflectance dissymmetric factor g_r and plot it in Figure 4c. The absolute value of the g_r reached 0.17 at wavelength 2 μm,

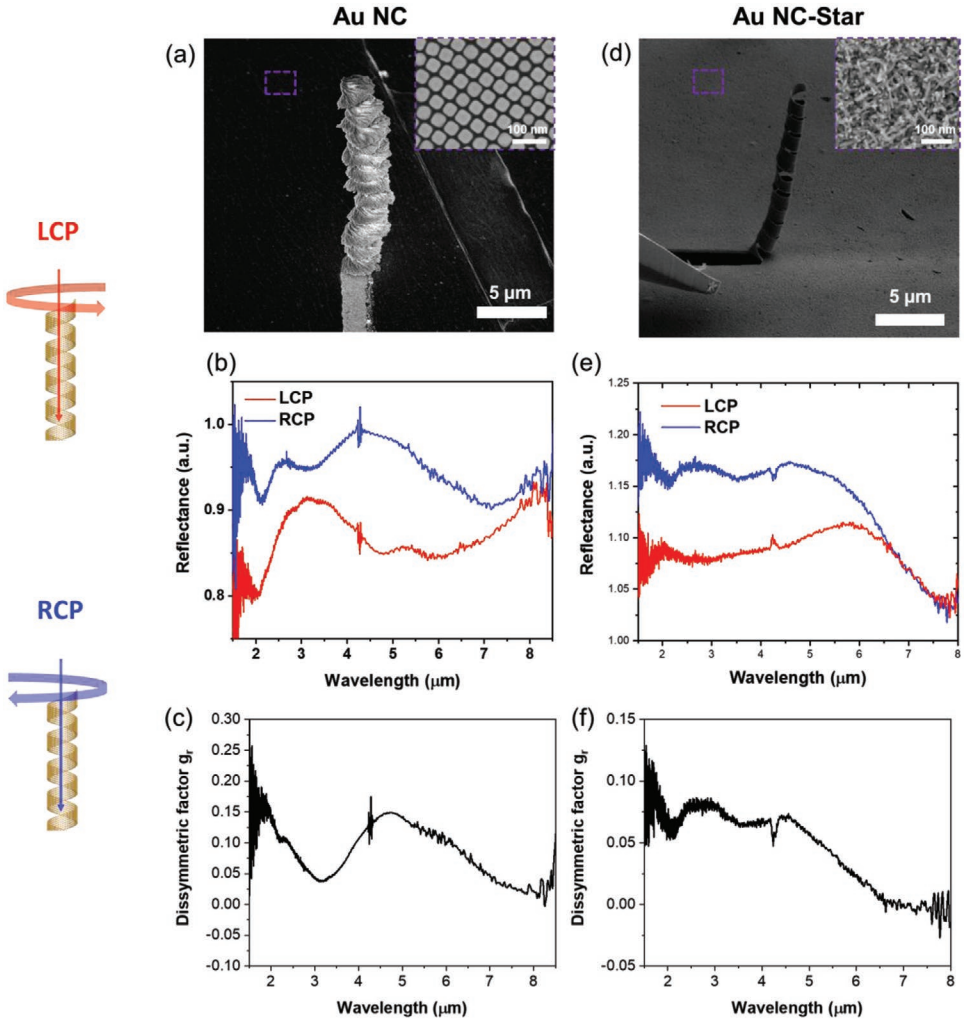

Figure 4. a) SEM images of a standing Au NC plasmene helix for PCL test. Insert shows the SEM image of the Au NC plasmene. b) Experimental reflectance spectra of a Au NC plasmene helix with polarized light. c) Reflectance dissymmetric factor versus wavelength calculated from (b). d) SEM images of a standing Janus NC-star plasmene helix for PCL test. Insert shows the SEM image of the Janus plasmene. e) Experimental reflectance spectra of a Janus thin NC-star plasmene helix with polarized light. f) Reflectance dissymmetric factor versus wavelength calculated from (e).

and 0.15 at wavelength 5 μm for a single plasmene helix. We found that the chiral reflectance properties of plasmene helix are sensitive to the shape of building blocks. As shown in Figure 4d–f, plasmene helix fabricated from Janus thin NC-star also showed well-pronounced chiroptical response toward LCP and RCP incidence, however, the g_r value was smaller than that for NC helix. This might stem from the higher light absorbance of dense spikes in the Janus plasmene helix. Simulation also depicts how the diameter and length of the plasmene helix can affect its chiroptical response as shown in Figure S11, Supporting Information. The chiroptical response for LCP and RCP changed significantly as the diameter increased, while the chirality only slightly altered when the length changed.

3. Conclusion

In summary, we have developed a nanospatula-based approach to construct 3D soft helical nanostructures from soft plasmene nanosheets. This combined top-down and bottom-up strategy enabled fabrication of a set of helical plasmonic nanostructures with reasonable control over internal and overall structural parameters. We measured the mechanical and chiral dissymmetrical optical properties from a single plasmene helix. Chiral dissymmetry in reflection g_r was found to be dependent on the morphologies of constituent building blocks. Our fabrication methodology provides a viable route to fabricate 3D soft plasmonic nanostructures with controllable morphological parameters to regulate their mechanical and optical properties, which may find novel applications in the field of flexible nanophotonics and plasmonic sensors.

4. Experimental Section

Synthesis of Au NCs: Au NCs were synthesized following a two-step seed-mediated method.[5] First, we synthesized Au seeds by adding 0.6 mL of $NaBH_4$ (0.01 M) into 0.1 mL of $HAuCl_4$ (25 mM) and 7.65 mL of CTAB (0.1 M). The solution was then incubated in a 30 °C water bath for

1 h. In the second step, a growth solution was prepared by mixing 1.6 mL of CTAB (0.1 M), 0.2 mL of $HAuCl_4$ (7 mM), 8 mL of Milli-Q water and 1.2 mL of ascorbic acid (AA) (0.1 M). Then, 5 µL of 10 times diluted seed solution was added into the growth solution and incubated in a 30 °C water bath overnight. The obtained Au NC nanoparticles was centrifuged at 7500 rpm for 10 min and re-dispersed in Milli-Q water for further use.

Fabrication of Au NC Plasmene: The Au NC plasmene was fabricated by a drying-mediated air-water interfacial self-assembly approach.[1] The Au NC nanoparticles were initially protected by CTAB surfactant, which were replaced by thiolated-PS (Mn = 50 000 g mol^{-1}) through a two-step ligand exchange method. Then, the PS-capped Au NC nanoparticles were washed with tetrahydrofuran for two times and chloroform for one time and finally re-dispersed in chloroform. Next, the PS-capped Au NC-chloroform solution was centrifuged and concentrated to ≈20 µL. 0.25 µL of the concentrated Au NC solution was then dropped on a sessile droplet sitting on the silicon substrate (or 7 µm × 7 µm holey copper grid for free-standing plasmene). Finally, a monolayered Au NC superlattice was obtained after the full evaporation of chloroform and water.

Fabrication of Janus NC-Star plasmene: Janus NC-star plasmene was fabricated following a two-step surface symmetry breaking method.[36] In the first step, the PS on the top side of Au NC plasmene was selectively removed by UV-ozone treatment for 5 min. In the second step, 5 µL of $HAuCl_4$ (0.3 M) was added on top of the Au NC plasmene, followed by adding 60 µL of HCl (1 M). After mixing the above chemicals, 30 µL of $AgNO_3$ (0.16 M) and 15 µL of AA (0.1 M) was added subsequently and mixed thoroughly with pipette after each addition. After 30 s, the Janus NC-star plasmene was obtained and rinsed with Milli-Q water for three times. Gentle sonication was then used to remove the giant impurities on the surface of Janus plasmene.

Fabrication of Spiral Kirigami: Au NC plasmene sheet on a holey copper grid was anchored on a 1 cm × 1 cm ITO glass by conductive copper tapes. The sample was then placed in FEI Helios Nanolab 600 FIB chamber. An accelerating voltage of 30 kV and an ion beam current of 9.7 pA and a dwell time of 100 µs were used to mill the plasmene to create a spiral pattern.

Fabrication of Plasmene Helix: A Picoprobe PT-14-6705-B probe tip was milled into a blade shape with sharp edge using FIB lithography before helix fabrication. The Au NC plasmene sheet on a silicon wafer was then mounted on a micro-manipulation stage that can move along three axis (*x*, *y*, and *z*). The oblique angle (α in Figure 1a) and the incline angle of the tip (β in Figure 1a) was carefully controlled to ≈45° and ≈20°, respectively, for all the samples. The tip was then loaded on an unmovable probe holder along the stage system. The whole system was then placed in FEI Helios Nanolab 600 FIB chamber with controller connection. To fabricate 3D plasmene helix, the plasmene nanosheet was first move along the *z*-axis and stop just before touching the probe. Then, the stage was moved along *z*-axis further until observing the probe oblique cutting into the plasmene nanosheet and start move the stage along *x*-axis only. By tuning the speed and the forces applied, different format of helix could then be obtained.

Characterization: The morphology of the samples was characterized through SEM (FEI Helios Nanolab 600 FIB-SEM operating at 5 kV). Mechanical compression test was carried by using a HYSITRON PI 85 SEM PicoIndenter with a 10 µm dia. flat punch, which is mounted inside a FEI Scios Dual beam FIB-SEM. Reflectance spectra of plasmene helix under CPL illumination was obtained by an FTIR system (Bruker Vertex 70) connected to a microscope (Bruker Hyperion 2000). The experimental setup of the optical characterization is demonstrated in Figure S12, Supporting Information.

Numerical Simulation: Full-wave simulations of the optical response of a free-standing plasmene helix were performed using CST Microwave Studio Suite. For an Au NC plasmene helix, unit cell (Floquet) boundary conditions were implemented along the both lateral directions with ports on the top and the bottom of the helix to obtain S-parameters to estimate reflectance and transmittance for LCP and RCP wave illumination over a specified wavelength window. For a freestanding plasmene helix, chiroptical response was clearly visible in its transmittance spectrum. Fine tetrahedral meshing with adaptive refinement was used to capture minute structural details in simulations. The plasmene helix structure was first created in a 3D graphical tool and then imported into CST to closely resemble the experimental sample details. Au NCs in the plasmene was assumed to be fully covered in polystyrene. Permittivity values of Au were taken from the literature.[37]

Supporting Information

Supporting Information is available from the Wiley Online Library or from the author.

Acknowledgements

Q.S. and D.D. contributed equally to this work. This work was performed in part at the Melbourne Centre for Nanofabrication (MCN) and the Micro Nano Research Facility at RMIT University in the Victorian Node of the Australian National Fabrication Facility (ANFF). Facilities and technical support from the RMIT Microscopy and Microanalysis Facility, a linked laboratory of Microscopy Australia, are acknowledged. This work was performed in part at the Monash Center for Electron Micron Microscopy. The authors appreciate the financial support from the Australian Research Council via Discovery Grant schemes DP200100624 and DE200101120. The authors acknowledge personnel and project funding from the Cooperative Research Centres Projects scheme. The authors acknowledge Miss Stella Aslanoglou, Dr. Beatriz Prieto-Simon, and Dr. Maria Alba for providing the SiO_2 tips array substrates. The authors also acknowledge the insightful discussions and technical support from Dr. Edwin Mayes and Dr. Sherman Wong.

Open access publishing facilitated by Monash University, as part of the Wiley - Monash University agreement via the Council of Australian University Librarians.

Conflict of Interest

The authors declare no conflict of interest.

Data Availability Statement

The data that support the findings of this study are available from the corresponding author upon reasonable request.

Keywords

3D spiral, chiral, helix, kirigami, plasmene, scroll

Received: November 4, 2022
Revised: January 16, 2023
Published online:

[1] K. J. Si, D. Sikdar, Y. Chen, F. Eftekhari, Z. Xu, Y. Tang, W. Xiong, P. Guo, S. Zhang, Y. Lu, Q. Bao, W. Zhu, M. Premaratne, W. Cheng, *ACS Nano* **2014**, *8*, 11086.
[2] W. Cheng, *Europhys. Lett.* **2017**, *119*, 48004.
[3] D. Dong, R. Fu, Q. Shi, W. Cheng, *Nat. Protoc.* **2019**, *14*, 2691.
[4] S. J. Tan, M. J. Campolongo, D. Luo, W. Cheng, *Nat. Nanotechnol.* **2011**, *6*, 268.

[5] Q. Shi, D. Sikdar, R. Fu, K. J. Si, D. Dong, Y. Liu, M. Premaratne, W. Cheng, *Adv. Mater.* **2018**, *30*, 1801118.
[6] Q. Shi, D. Dong, K. J. Si, D. Sikdar, L. W. Yap, M. Premaratne, W. Cheng, *ACS Nano* **2018**, *12*, 1014.
[7] S. Rao, K. J. Si, L. W. Yap, Y. Xiang, W. Cheng, *ACS Nano* **2015**, *9*, 11218.
[8] Q. Shi, R. Fu, D. Sikdar, T. Perera, A. S. R. Chesman, Z. Yong, Y. Lu, Y. Liu, Z. Guo, S. Gong, M. Premaratne, W. Cheng, *J. Phys. Chem. C* **2021**, *125*, 27753.
[9] K. J. Si, Y. Chen, W. Cheng, *Mater. Today* **2016**, *19*, 363.
[10] J. T. Pham, J. Lawrence, G. M. Grason, T. Emrick, A. J. Crosby, *Phys. Chem. Chem. Phys.* **2014**, *16*, 10261.
[11] J. K. Gansel, M. Thiel, M. S. Rill, M. Decker, K. Bade, V. Saile, G. von Freymann, S. Linden, M. Wegener, *Science* **2009**, *325*, 1513.
[12] M. Hentschel, M. Schäferling, X. Duan, H. Giessen, N. Liu, *Sci. Adv.* **2017**, *3*, e1602735.
[13] J. Lu, Y. Xue, N. A. Kotov, *Isr. J. Chem.* **2021**, *61*, 851.
[14] W. Wu, M. Pauly, *Mater. Adv.* **2022**, *3*, 186.
[15] X. Shen, C. Song, J. Wang, D. Shi, Z. Wang, N. Liu, B. Ding, *J. Am. Chem. Soc.* **2012**, *134*, 146.
[16] Q. Yue, L. Wang, H. Fan, Y. Zhao, C. Wei, C. Pei, Q. Song, X. Huang, H. Li, *Inorg. Chem.* **2021**, *60*, 4226.
[17] J. Kaschke, L. Blume, L. Wu, M. Thiel, K. Bade, Z. Yang, M. Wegener, *Adv. Opt. Mater.* **2015**, *3*, 1411.
[18] W. Li, Z. J. Coppens, L. V. Besteiro, W. Wang, A. O. Govorov, J. Valentine, *Nat. Commun.* **2015**, *6*, 8379.
[19] I. Sakellari, X. Yin, M. L. Nesterov, K. Terzaki, A. Xomalis, M. Farsari, *Adv. Opt. Mater.* **2017**, *5*, 1700200.
[20] J. K. Gansel, M. Latzel, A. Frölich, J. Kaschke, M. Thiel, M. Wegener, *Appl. Phys. Lett.* **2012**, *100*, 101109.
[21] J. Kaschke, M. Wegener, *Opt. Lett.* **2015**, *40*, 3986.
[22] B. Frank, X. Yin, M. Schäferling, J. Zhao, S. M. Hein, P. V. Braun, H. Giessen, *ACS Nano* **2013**, *7*, 6321.
[23] M. Esposito, V. Tasco, M. Cuscunà, F. Todisco, A. Benedetti, I. Tarantini, M. D. Giorgi, D. Sanvitto, A. Passaseo, *ACS Photonics* **2015**, *2*, 105.
[24] X. Lan, Q. Wang, *Adv. Mater.* **2016**, *28*, 10499.
[25] A. Kuzyk, R. Schreiber, Z. Fan, G. Pardatscher, E.-M. Roller, A. Högele, F. C. Simmel, A. O. Govorov, T. Liedl, *Nature* **2012**, *483*, 311.
[26] J. Cheng, G. Le Saux, J. Gao, T. Buffeteau, Y. Battie, P. Barois, V. Ponsinet, M.-H. Delville, O. Ersen, E. Pouget, R. Oda, *ACS Nano* **2017**, *11*, 3806.
[27] R.-Y. Wang, H. Wang, X. Wu, Y. Ji, P. Wang, Y. Qu, T.-S. Chung, *Soft Matter* **2011**, *7*, 8370.
[28] X. Lan, T. Liu, Z. Wang, A. O. Govorov, H. Yan, Y. Liu, *J. Am. Chem. Soc.* **2018**, *140*, 11763.
[29] C.-L. Chen, P. Zhang, N. L. Rosi, *J. Am. Chem. Soc.* **2008**, *130*, 13555.
[30] C. Song, M. G. Blaber, G. Zhao, P. Zhang, H. C. Fry, G. C. Schatz, N. L. Rosi, *Nano Lett.* **2013**, *13*, 3256.
[31] X. Lan, X. Lu, C. Shen, Y. Ke, W. Ni, Q. Wang, *J. Am. Chem. Soc.* **2015**, *137*, 457.
[32] J. G. Williams, Y. Patel, B. R. K. Blackman, *Eng. Fract. Mech.* **2010**, *77*, 293.
[33] J. G. Williams, Y. Patel, *Interface Focus* **2016**, *6*, 20150108.
[34] G. Fang, P. Zeng, *J. Mater. Process. Technol.* **2005**, *168*, 42.
[35] B. Aksu, C. Çelebi, E. Budak, *Mach. Sci. Technol.* **2016**, *20*, 495.
[36] Q. Shi, D. E. Gómez, D. Dong, D. Sikdar, R. Fu, Y. Liu, Y. Zhao, D.-M. Smilgies, W. Cheng, *Adv. Mater.* **2019**, *31*, 1900989.
[37] P. B. Johnson, R. W. Christy, *Phys. Rev. B* **1972**, *6*, 4370.

ADVANCED ELECTRONIC MATERIALS
www.advelectronicmat.de

Mechanical Properties of Organic Electronic Polymers on the Nanoscale

*Vishal Panchal, Illia Dobryden, Ude D. Hangen, Dimitrios Simatos, Leszek J. Spalek, Ian E. Jacobs, Guillaume Schweicher, Per M. Claesson, and Deepak Venkateshvaran**

Organic semiconducting polymers have attractive electronic, optical, and mechanical properties that make them materials of choice for large area flexible electronic devices. In these devices, the electronically active polymer components are micrometers in size, and sport negligible performance degradation upon bending the centimeter-scale flexible substrate onto which they are integrated. A closer look at the mechanical properties of the polymers, on the grain-scale and smaller, is not necessary in large area electronic applications. In emerging micromechanical and electromechanical applications where the organic polymer elements are flexed on length scales spanning their own micron-sized active areas, it becomes important to characterize the uniformity of their mechanical properties on the nanoscale. In this work, the authors use two precision nanomechanical characterization techniques, namely, atomic force microscope based PeakForce quantitative nanomechanical mapping (PF-QNM) and nanoindentation-based dynamical mechanical analysis (nano-DMA), to compare the modulus and the viscoelastic properties of organic polymers used routinely in organic electronics. They quantitatively demonstrate that the semiconducting near-amorphous organic polymer indacenodithiophene-co-benzothiadiazole (C16-IDTBT) has a higher carrier mobility, lower modulus, and greater nanoscale modulus areal uniformity compared to the semiconducting semicrystalline organic polymer poly[2,5-bis(3-tetradecylthiophen-2-yl) thieno[3,2-b]thiophene] (C14-PBTTT). Modulus homogeneity appears intrinsic to C16-IDTBT but can be improved in C14-PBTTT upon chemical doping.

1. Introduction

Conjugated semiconducting organic polymers and amorphous polymer dielectrics, jointly referred to in this work as organic electronic polymers, have played a pivotal role in the development of flexible and printed electronics over the last two decades.[1–3] Composed from rings and chains of carbon atoms, these materials sport a low mass density, as well as electronic, optical, and mechanical properties that are tailored through the chemical design of their constituent molecular units. Weak inter-chain van der Waals bonding within thin films of stacked conjugated organic polymers renders them soft, with intrinsically low Young's moduli several orders of magnitude smaller than conventional inorganic semiconductors such as silicon.[4] These mechanical properties, coupled with a conjugated organic polymer's ability to transport both charges and ions through their matrix, have expanded their use in new research areas such as organic bioelectronics and neural recording.[5–10]

Organic polymers such as poly(3,4-ethylenedioxythiophene) polystyrene sulfonate (PEDOT:PSS) are now a routine choice for flexible microelectrode array implants,[11] and their incorporation is known to improve electrical measurements through lower electrode impedances and higher signal-to-noise ratios. However, a recent nanoscale mechanical characterization of the PEDOT:PSS film elements used in such microelectrode arrays showed local variations over an individual probe, on a length scale of a couple of square micrometers.[12,13] This variation was

V. Panchal
Bruker UK
Banner Lane, Coventry CV4 9GH, UK

I. Dobryden, P. M. Claesson
KTH Royal Institute of Technology
School of Engineering Sciences in Chemistry, Biotechnology and Health, Department of Chemistry, Division of Surface and Corrosion Science
Drottning Kristinas väg 51, Stockholm SE-100 44, Sweden

The ORCID identification number(s) for the author(s) of this article can be found under https://doi.org/10.1002/aelm.202101019.

DOI: 10.1002/aelm.202101019

I. Dobryden
Experimental Physics, Division of Materials Science
Department of Engineering Sciences and Mathematics
Luleå University of Technology
Luleå SE-971 87, Sweden

U. D. Hangen
Bruker Nano GmbH
Dennewartstrasse 25, 52068 Aachen, Germany

D. Simatos, L. J. Spalek, I. E. Jacobs, D. Venkateshvaran
Cavendish Laboratory
University of Cambridge
JJ Thomson Avenue, Cambridge CB3 0HE, UK
E-mail: dv246@cam.ac.uk

G. Schweicher
Laboratoire de Chimie des Polymères, Faculté des Sciences
Université Libre de Bruxelles (ULB)
Boulevard du Triomphe, Brussels 1050, Belgium

down to the PSS-rich regions having a higher modulus, and the PEDOT-rich regions having a lower modulus. Insights such as this allow one to re-engineer the nanomechanical properties of the polymer elements within multielectrode arrays to ensure performance reproducibility across all electrodes in the device.

In this work, we quantify the nanomechanical properties, their spatial homogeneity, and the depth-dependent viscoelastic behavior of three well known organic electronic polymers having three different morphologies. These polymers have been successfully used in functional organic thin film transistors over the years. Their processing for device integration from solution as well as their electronic properties are well understood, and a characterization of their nanomechanical properties make them future-ready for applications in conjugated polymer-based micro and nanomechanical devices. The three polymers investigated here are, a) the semiconducting semicrystalline polymer poly[2,5-bis(3-tetradecylthiophen-2-yl) thieno[3,2-b]thiophene] abbreviated as C14-PBTTT,[14,15] b) the semiconducting near-amorphous planar-backbone donor–acceptor co-polymer indacenodithiophene-co-benzothiadiazole abbreviated as C16-IDTBT,[16–18] and c) the dielectric amorphous fluoropolymer Cytop-M from AGC Inc.[19] Our study attempts to quantify nanomechanical texture on length scales spanning several tens of nanometers to several hundred nanometers in these polymers, as such dimensions are directly applicable within micromechanical resonators. **Figure 1**a shows the chemical structures of these three organic polymers. Figure 1b displays a cross-sectional schematic of the top-gate bottom-contact organic thin film transistors measured in this work. These transistors use a Cytop-M dielectric with an active layer of either C14-PBTTT or C16-IDTBT. Figure 1c shows the typical transfer and output characteristics of a field-effect transistor based on C14-PBTTT. The saturation mobility extracted from these measurements at maximum bias is 0.1 $cm^2\ V^{-1}\ s^{-1}$. Figure 1d shows the typical transfer and output characteristics of a field-effect transistor based on C16-IDTBT. The saturation mobility extracted from these measurements at maximum bias is 1 $cm^2\ V^{-1}\ s^{-1}$.

Although the micromechanical properties of C14-PBTTT were estimated using buckling metrology several years ago, the technique operated on the scale of hundreds of microns and was thus unable to differentiate between the intra-grain Young's modulus and the grain boundary Young's modulus within the film.[20] In our effort to better understand the nanomechanical properties of the individual layers in organic field-effect transistors, we use high-resolution PeakForce quantitative nanomechanical mapping (PF-QNM) of the Young's modulus to demonstrate nanomechanical property variations in thin films of the semicrystalline polymer C14-PBTTT.[21–23] We compare these semicrystalline nanomechanical properties with those of the near-amorphous low backbone torsion polymer semiconductor C16-IDTBT, and with the amorphous polymer dielectric Cytop-M. Cytop-M is routinely deployed as a gate dielectric within organic thin film transistors as shown in Figure 1. Unlike C14-PBTTT, both C16-IDTBT and Cytop-M have a smooth topography and show greater mechanical

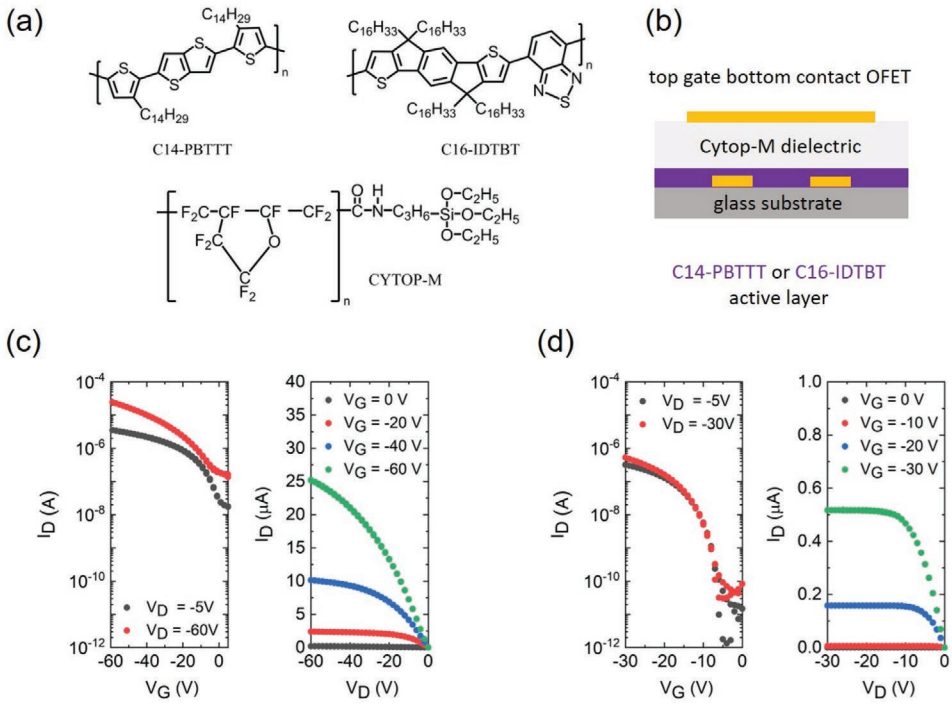

Figure 1. a) Chemical structures of the semicrystalline conjugated organic polymer C14-PBTTT, the near-amorphous conjugated organic polymer C16-IDTBT, and the amorphous fluorinated polymer Cytop-M. b) Cross-sectional schematic of a bottom-contact top-gate organic field-effect transistor architecture. c) Transfer and output characteristics of a C14-PBTTT based field-effect transistor with a Cytop-M dielectric. The channel length and width in this organic transistor was $L = 20$ μm and $W = 1$ mm, respectively. d) Transfer and output characteristics of a C16-IDTBT based field-effect transistor with a Cytop-M dielectric. The channel length and width in this organic transistor was $L = 120$ and $W = 40$ μm, respectively. The thin films of C14-PBTTT, C16-IDTBT, and Cytop-M were 50, 45, and 500 nm thick, respectively.

uniformity on the nanoscale. We finally use nanoindentation-based nanoscale dynamical mechanical analysis (nano-DMA) to draw up a comparison between the viscoelastic properties of the three organic polymers in question. The significant differences that we observe in the magnitude and nanoscale homogeneity of the mechanical properties in these materials provide crucial insights for the design of ultra-small polymer semiconductor based mechanical resonators.

2. Experimental Probes of Organic Polymer Nanomechanics

The atomic force microscope (AFM) based quantitative nanomechanical mapping of the Young's modulus, the adhesion and the deformation were performed using Bruker's Dimension IconXR. The measurements were performed with PeakForce Tapping based quantitative nanomechanical mapping (at 2 kHz) together with a laser Doppler vibrometer factory calibrated AFM probe with 30 nm tip radius and spring constant of 42.8 N m^{-1} (RTESPA-300-30), which are designed specifically for nanomechanical measurements. During the nanomechanical property mapping, the scan rate was set to 0.4 Hz, the PeakForce setpoint was 50 nN, and the scan area was set to 5 μm × 5 μm or 1 μm × 1 μm with 512 × 512 pixels. The imaging time took ≈20 min per scan. Before and after the measurements on the organic polymer samples presented in this study, the Dimension IconXR AFM was used to measure a reference sample of PDMS to confirm its known properties (see Section S1, Supporting Information). The reduced Young's moduli (E^*) reported in this work are extracted for every single pixel of the modulus maps by fitting the retract part of the force curve using the DMT model, $F_{tip} = \frac{4}{3} E^* \sqrt{Rd^3} + F_{adh}$, which takes into account the force on the tip (F_{tip}), the tip-sample adhesion force (F_{adh}), tip end radius (R), and tip-sample separation (d).[21–23]

Additional confirmatory nanomechanical measurements were carried out on semicrystalline C14-PBTTT samples using a Dimension FastScan AFM (Bruker, USA). The measurements were conducted using a Tap300DLC probe with a diamond-like carbon tip coating. The actual spring constant, calibrated with the thermal calibration method, was 54.3 N m^{-1}. The tip outer radius was evaluated using a titanium roughness sample (RS-12M) and was ≈9–10 nm. The PeakForce setpoint was set to 98 nN. The scan rate in this case was 1.88 Hz.

Since confinement and nanostructuring are known to impact the measured mechanical properties of organic polymers, it is crucial to specify the thickness of the organic polymer films when specifying their measured modulus.[24] In this study, the thickness of the three organic electronic polymers were chosen in keeping with their routine deposition parameters and dimensions used in organic field-effect transistors. The thin films of C14-PBTTT, C16-IDTBT, and Cytop-M reported here were 50, 45, and 500 nm thick, respectively. The thickness was estimated using a combination of an AFM and a DektakXT stylus profilometer. The error on these measurements was ≈5%. The organic thin films were spin-coated from solution onto very low surface roughness Si/SiO_2 substrates. Since the methods used to deposit the films also affect the measured elastic properties,[25,26] it is also important to connect the measured values with the chosen film growth procedures (see Section S2, Supporting Information).

The topography, modulus, adhesion, and deformation documented in this work were extracted from the measured force curves between the AFM cantilever tip and the sample surface during measurement and plotted using the Gwyddion software with little to no data post-processing. Other than selecting a color palette and choosing an appropriate scale bar, no post-processing was done on the maps of the modulus, adhesion, and deformation. A correction to the modulus map was made to remove artefacts arising from horizontal line scanning only if necessary. Such minimal data surgery ensures a high level of data integrity as well as an ability to draw comparisons across the three polymers with confidence. In the case of the topography alone, Gwyddion's Align Rows feature was used with the median method to remove artefacts related to line scanning.

Nanoindentation-based nano-DMA on the three polymer films was performed using Bruker's Hysitron TI 980 TriboIndenter equipped with a Performech II controller. The thin film samples were mechanically clamped to the Hysitron stage without the need for additional sample preparation. The indentation experiments were performed using a cube corner indenter, the sharp geometry of which allows deforming a minimum sample volume to avoid substrate effects on the thin film measurement. Seeing as some of the organic films studied here are only ≈50 nm thick, the measurements using the TriboIndenter are done close to the instrument's working limits on sample thickness. The indentation tests shown in this work were performed with a standard 10 mN nano-DMA III transducer, but the actual load applied on the soft surface was typically only a few μN. During a nano-DMA examination, a relatively small sinusoidal load is superimposed over the quasi-static load applied to the probe. The resulting sinusoidal displacement signal-associated phase lag, together with the transducer calibration, are used to calculate the stiffness (k_s) and damping of the sample (C_s). Once the stiffness and damping of the materials are known, the dynamic moduli E' and E'' as well as tan δ are calculated according to the equations, $E' = \frac{k_s \sqrt{\pi}}{2\sqrt{A}}$, $E'' = \frac{\omega C_s \sqrt{\pi}}{2\sqrt{A}}$ and $\tan\delta = \frac{\omega C_s}{k_s}$. The storage modulus, E', is the in-phase or real component of the modulus while the loss modulus, E'', is the out-of-phase or imaginary component. E' describes the material's elastic response while E'' describes the material's viscous response. In the equations, A is the projected contact area and ω is the angular oscillation frequency. tan δ is simply the ratio of the two dynamic moduli. We performed the dynamic indentation experiments at 20 Hz with a dynamic amplitude of 2 nm and the film properties were determined at small penetration depths of few nanometers. The stiff Si/SiO_2 substrates used reduces the displacement amplitude at larger depths, increasing the scattering in the measured parameters E', E'', and tan δ. Small penetration depths are necessary to avoid the limitations of pile-up which inadvertently affect the use of the Oliver Pharr procedure to estimate the modulus through indentation measurements on polymers.[27]

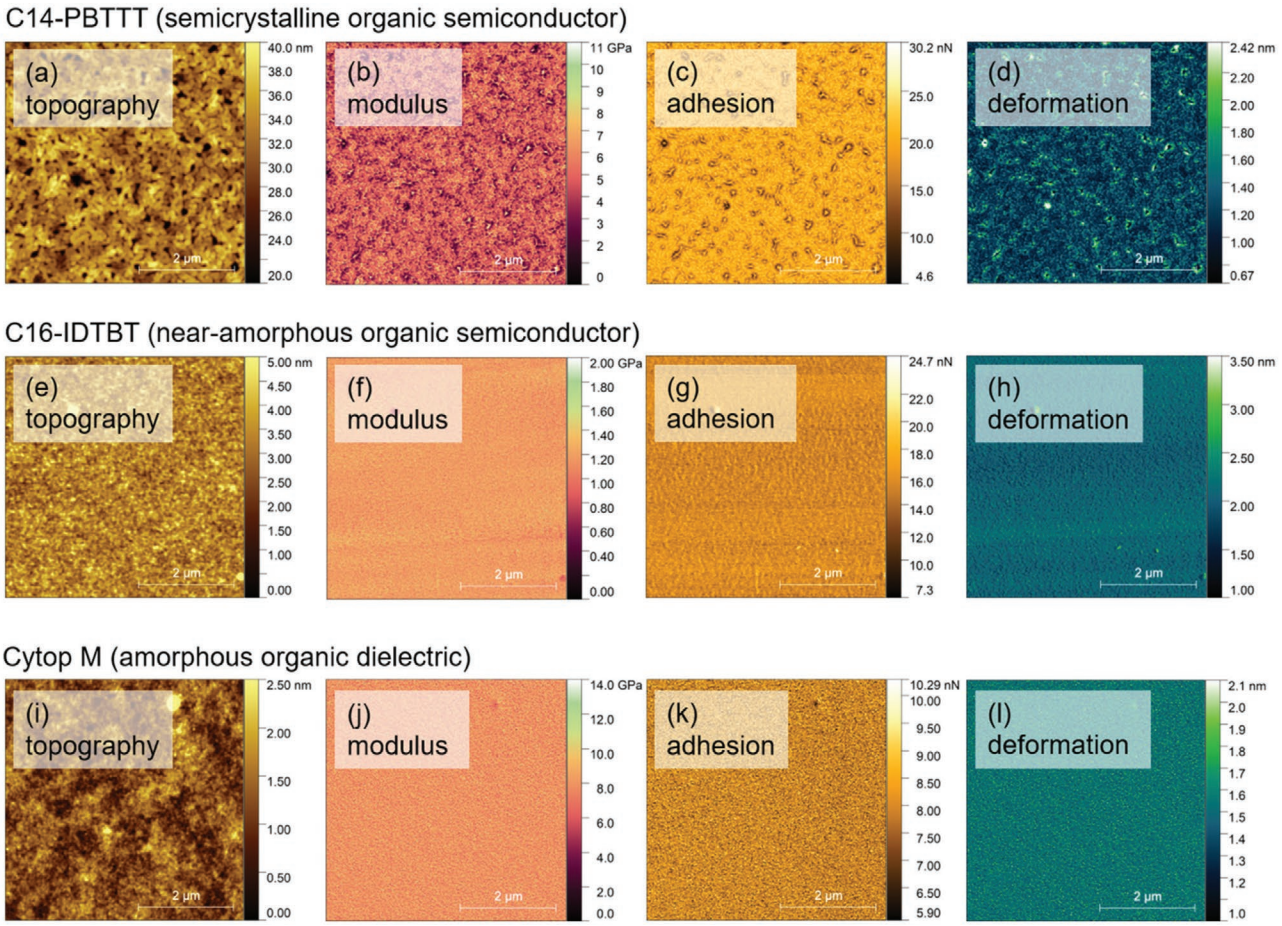

Figure 2. Topography, modulus, adhesion, and deformation in three organic electronic polymers, namely, C14-PBTTT (a–d), C16-IDTBT (e–h), and Cytop-M (i–l).

3. Results and Discussion

The nanomechanical properties of the organic electronic polymers measured using PF-QNM and their viscoelastic properties measured using nanoindentation are described in succession below.

3.1. PeakForce QNM Based Nanomechanical Characterization

Spatial maps of the topography, modulus, adhesion, and deformation over a 5 µm x 5 µm scan area in C14-PBTTT, C16-IDTBT, and Cytop-M measured using PF-QNM are shown in **Figure 2**. As seen in this materials overview figure, large terraces of C14-PBTTT with voids in between the crystallites are evident from its topography. The modulus of C14-PBTTT follows these crystallites and displays significant non-uniformity. On the other hand, both the near-amorphous C16-IDTBT and the amorphous Cytop-M have smooth surfaces and show a high level of uniformity in their maps of topography and modulus at the current image resolution and scanned image size. The average values of the topographical roughness and modulus, together with the adhesion and deformation for the three different polymers are tabulated in **Table 1** together with their RMS variations. C16-IDTBT and Cytop-M show an RMS topographical roughness <0.55 nm. C14-PBTTT on the other hand is significantly rougher. The measured average modulus over the scan area of 5 µm × 5 µm was 4.8 GPa for C14-PBTTT but came with a much greater RMS variation of nearly 30% in comparison with C16-IDTBT and Cytop-M. C16-IDTBT was the softest material of the three polymers with an average modulus of only 1.2 GPa, accompanied by a very high spatial uniformity as seen in its RMS variation of less than 10% the average value. The measured softness in the C16-IDTBT films is reflected in relatively larger values of the surface deformation of the film. Cytop-M shows the highest average modulus of the three polymers with a spatial uniformity larger than C14-PBTTT but

Table 1. Average values of roughness, modulus, adhesion, and deformation in the three organic electronic polymers, C14-PBTTT, C16-IDTBT, and Cytop-M measured over 5 µm × 5 µm.

Polymer	RMS roughness [nm]	Modulus [GPa]	Adhesion [nN]	Deformation [nm]
C14-PBTTT	3.21	4.80 ± 1.29	19.33 ± 2.36	1.25 ± 0.23
C16-IDTBT	0.55	1.17 ± 0.13	15.67 ± 1.43	2.07 ± 0.17
Cytop-M	0.39	7.91 ± 1.02	7.99 ± 0.71	1.53 ± 0.11

significantly smaller than C16-IDTBT. The adhesion of the three polymers C14-PBTTT, C16-IDTBT, and Cytop-M shows a trend that decreases jointly with the degree of crystallinity and the level of roughness in the film, with the rough semicrystalline sample C14-PBTTT having the highest adhesion and the amorphous flat Cytop-M sample having the lowest adhesion. Accurate estimates of the surface adhesion in these polymers are contingent on a complete removal of any residual solvent in the film prior to measurement.

Previous studies on polythiophenes such as C14-PBTTT have shown that a higher crystallinity within the organic polymer film leads to both a higher charge carrier mobility as well as a larger modulus.[20] This intuitive relationship between the crystallinity, charge carrier mobility, and modulus, is not immediately apparent in C16-IDTBT and is discussed further below.

Both C14-PBTTT and C16-IDTBT have high charge carrier mobilities approaching 1 cm^2 V^{-1} s^{-1},[16,28,29] although the underlying charge transport mechanisms are different in the two materials. C14-PBTTT is ordered within its semicrystalline regions, with interdigitated alkyl side chains that enhance structural rigidity to facilitate charge transport along the π–π stacking direction in addition to transport along the twisted polymer backbone.[28] In the case of C16-IDTBT however, its ultralow backbone-torsion permits fast transport along the polymer spine that is not impeded by the lack of alkyl side chain order.[16] This is fundamentally why the two materials sport very different morphologies but still possess appreciable charge carrier mobilities. To help connect this existing picture with the mechanical properties of the two polymers, **Figure 3** shows high-resolution data on the topography and modulus maps over an area of 1 μm^2 for semicrystalline C14-PBTTT

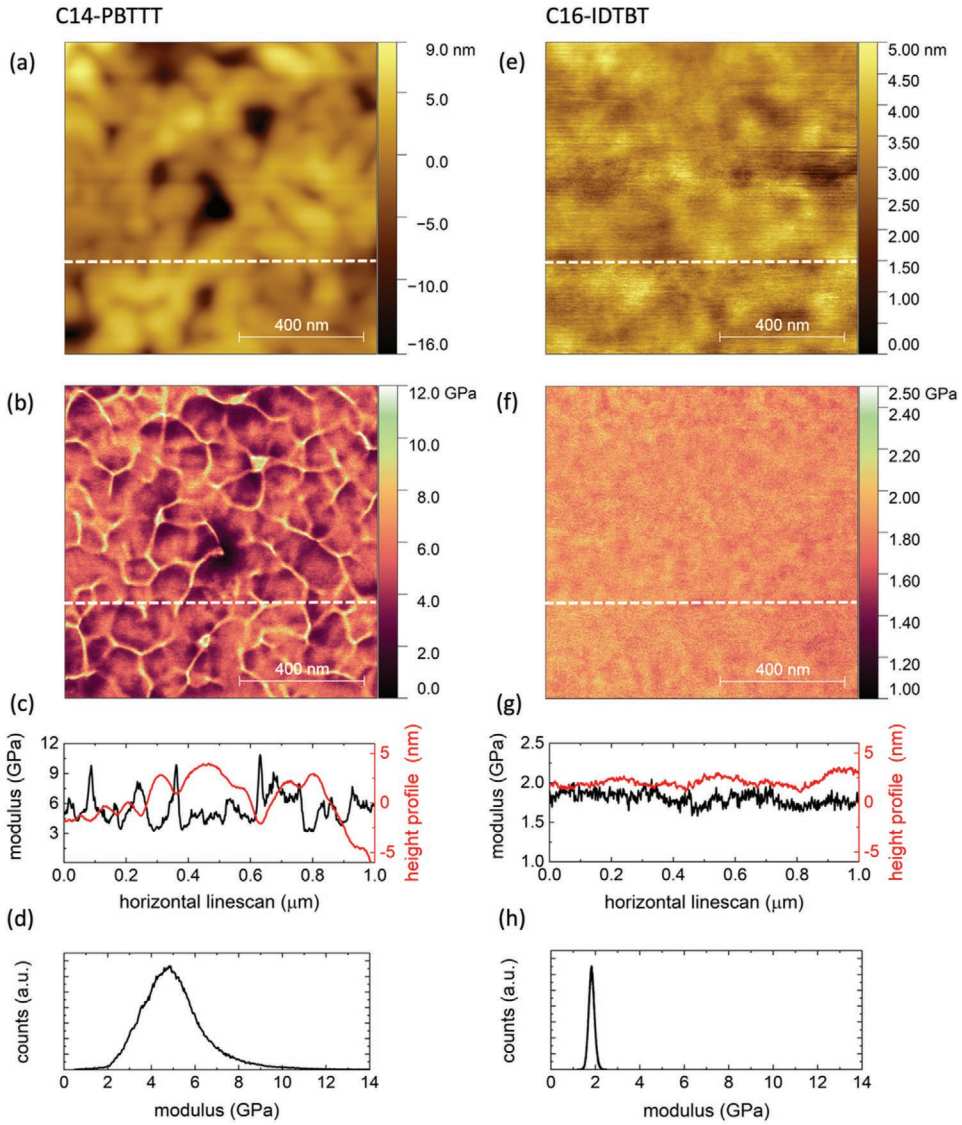

Figure 3. (a–d) are the topography, modulus, modulus, and topographical line scans along the dotted white lines, and modulus histogram over 1 μm × 1 μm, in C14-PBTTT respectively. (e–h) are the topography, modulus, modulus, and topographical line scans along the dotted white lines, and modulus histogram over 1 μm × 1 μm, in C16-IDTBT respectively.

and for near-amorphous C16-IDTBT. Figure 3a maps the individual grains and grain boundaries between the crystallites in C14-PBTTT. In Figure 3b, the corresponding spatial modulus is plotted, demonstrating clearly that the uniformity is broken at the grain boundaries. The same is visualized in Figure 3c which plots a line scan along the dotted white line of Figure 3b. Figure 3c also includes a line scan of the height topography, shown in red, along the white dotted line of Figure 3a showing that the modulus peaks at the topographical grain boundaries. The significant difference in the line scans of the topography and the modulus in Figure 3c is additional confirmation that the measured features are not influenced by the tip itself. Figure 3d plots a histogram of the moduli measured over the 512 × 512 pixels covering the area of 1 μm^2. The measured average modulus is 5.1 ± 1.6 GPa but displays large variations across the area as seen through the width of the histogram. These properties are in stark contrast to the topography and modulus of C16-IDTBT shown in Figures 3e and 3f, respectively. The topographical image clarity depends on the type of probe used, its radius, the surface force applied, and the dimension of the features on the film. Using the current cantilever tip with tip radius of 30 nm (designed primarily for nanomechanical measurements and hence stiffer than conventional AFM probes), the topography appears blurry on scanned areas of a square micron and under. This is on account of limited lateral resolution, but also because the C16-IDTBT surface is very smooth. It has a topographical roughness much smaller than the deformation on the surface during measurement. The soft surface is hence potentially flattened during the measurement. One should keep in mind that the topography and the modulus are coupled in these measurements as they are quantities read out from the same force curve. The topographical scans shown in this work are for the case where large forces are applied to the surface, as opposed to conventional AFM measurements that do not require simultaneous surface indentation. Under these conditions and at high-resolution, these films are smooth, and show little spatial variation in the modulus. A modulus line scan along the white dotted line of Figure 3f is shown in Figure 3g together with its accompanying topographical line scan. This line scan demonstrates a high level of lateral uniformity in the modulus, even though the topography registers a broader undulation. The fact that the grain size of C16-IDTBT is well below the diameter of the cantilever tip,[30] places a limit on the nanoscale variations that can be imaged using our current setup, and on the length scale that we report uniformity over. Figure 3h documents the comparably narrow modulus histogram of C16-IDTBT over the 1 μm^2 scanned area, demonstrating little spatial variation with an average value of 1.8 ± 0.1 GPa. Despite being smooth and near-amorphous, the width of the modulus histogram for C16-IDTBT is well below that of Cytop-M, which is fully amorphous but comparatively smooth (see Section S3, Supporting Information).

On first assessment, it may seem as though the modulus values measured on the 1 μm^2 areas are larger than those measured on 5 μm × 5 μm areas (Figure 2 and Table 1). In the case of C14-PBTTT, the modulus values agree within the error bars. In the case of C16-IDTBT on the other hand, the average modulus goes from 1.2 GPa measured over 5 μm × 5 μm to 1.8 GPa measured over 1 μm × 1 μm. An additional measurement that we performed on an area of 5 μm × 2.5 μm a week earlier to that documented in Figure 1, but which again confirmed the spatial homogeneity (narrow modulus histogram) on the probed length scales in C16-IDTBT showed an average modulus value of 2 GPa (see Section S4, Supporting Information). Repeated measurements on several areas in various C16-IDTBT films have confirmed that the value of its nanoscale modulus, measured a few weeks after fabrication and upon ambient air exposure, sits between 1 and 2 GPa. The narrow modulus histogram in C16-IDTBT remains a universal feature in the repeated measurements.

Improved spatial homogeneity in the modulus of the semicrystalline polymer C14-PBTTT can be achieved upon chemical doping. A recent study on the semiconducting polymer P3HT, containing both amorphous and crystalline domains, showed that chemical doping tends to soften the crystalline domains.[31] The doped crystalline domains in P3HT show a reduced modulus, and their co-existence with amorphous domains in the film causes the spatial modulus histogram in doped P3HT to show a double peak feature.[31] C14-PBTTT films have large semicrystalline terraces, and when chemically doped, shows a spatial modulus histogram that has a single peak. **Figure 4**a shows a comparison of the spatial modulus measured on a pristine C14-PBTTT film compared with a C14-PBTTT film that was chemically doped to high conductivities up to 1000 S cm^{-1} using an ion exchange based doping process (see Section S5, Supporting Information).[32] The pristine C14-PBTTT film has a low conductivity of ≈10^{-5} S cm^{-1} at low lateral bias and under no applied gate voltage. This intrinsic value is on account of C14-PBTTT's unintentional doping in oxygen. The diminished contrast in the measured modulus within the doped C14-PBTTT film shows that the individual domains are uniformly reduced in the average modulus. Doping also leads to a reduction in the modulus at the grain boundaries, as seen in Figure 4b that compares modulus line scans in pristine C14-PBTTT with doped C14-PBTTT along the white dotted lines of Figure 4a. Figure 4c compares the spatial modulus histograms of pristine C14-PBTTT, doped C14-PBTTT, and C16-IDTBT. In addition to a reduced average modulus of 3.36 ± 1.03 GPa, doping of semicrystalline C14-PBTTT also leads to higher spatial uniformity, reflected in a narrower width of the modulus histogram. Although this represents an improvement over pristine C14-PBTTT, the homogeneity is still less than that measured in C16-IDTBT. C16-IDTBT cannot be efficiently doped using the same ion exchange procedure on account of its near-amorphous character. The cause for a reduced modulus in C14-PBTTT upon doping may be down to a few factors. One factor accounts for an expansion of the lamellae upon dopant incorporation within the film, which reduce alkyl side chain van der Waals interactions and reduce the attractive Coulombic interaction between planes of dopant ions and polarons.[32] A second factor may be down to a small number of residual solvent molecules that are incorporated in the film during the ion-exchange doping procedure.

In performing the nanomechanical measurements on C14-PBTTT and on C16-IDTBT, we processed the films using our optimized protocol that ensures high charge carrier mobilities within field-effect transistors.[16,28] Devices made from C14-PBTTT are known to show high mobilities immediately

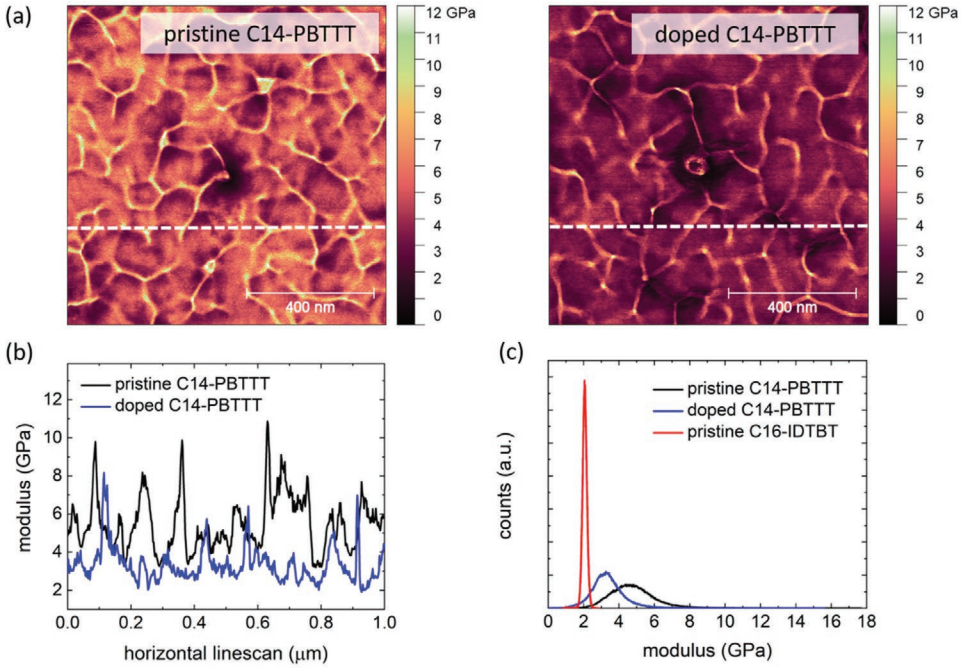

Figure 4. a) Comparison between the areal modulus over 1 μm × 1 μm in pristine C14-PBTTT and in doped C14-PBTTT, b) modulus line scans along the dotted white lines in pristine C14-PBTTT and in doped C14-PBTTT, and c) comparison between the modulus histograms measured over 1 μm × 1 μm in pristine C14-PBTTT, in doped C14-PBTTT and in C16-IDTBT.

after fabrication but degrade over a span of days to weeks upon air exposure.[15,28,33,34] The degradation of C14-PBTTT in air is seen through a gradually diminishing on-current, a gradually reducing mobility, and an increasing off-current in transistors fabricated from it.[15,28,33,34] C16-IDTBT on the other hand, requires a few days of air exposure to stabilize its high mobility after which it remains air stable for months.[35] Hence, to probe the nanomechanical properties of C14-PBTTT and doped C14-PBTTT in their high mobility configuration, the measurements on them were carried out within the first week from fabrication. The measurements on C16-IDTBT on the other hand, were measured a few weeks after fabrication to allow sufficient time for the polymer film to stabilize its electronic properties in air. This process ensures that trap healing in C16-IDTBT is complete within the film at the time of estimating its modulus (see Section S6, Supporting Information). A comprehensive study on how the mechanical properties in C14-PBTTT age when left in air over several weeks is an investigation that goes beyond the current work. This said, preliminary measurements hint at there being a modest change in C14-PBTTT after several weeks (see Sections S7 and S8, Supporting Information). This change potentially accompanies its electronic degradation over the same period. The role of humidity upon air exposure in these films is not known at this time, but detrimental effects have been observed previously in organic–inorganic semicrystalline films where the degradation mechanism begins at the grain boundaries.[36,37] All told, the fact that C16-IDTBT sports a high mobility despite its near-amorphous morphology in addition to a spatially homogeneous modulus that is comparatively low, makes this donor–acceptor co-polymer semiconductor a candidate for truly flexible organic microelectronics and electromechanical devices.[38]

3.2. TriboIndenter-Based Nanoscale Viscoelastic Property Characterization as a Complementary Characterization Tool to PeakForce QNM

Nanoindentation based mechanical measurements complement the mechanical properties determined by AFM-based PF-QNM. Although the contact mechanics between the tip and the sample are similar in both approaches, the sensor characteristics are different. An exploration of a larger field of parameters can thus be made by employing both techniques side by side. The larger dimension of the indenter in nanoindentation permits its force and displacement measurement to be calibrated utilizing standards from NIST which remain even when tips are changed. The tips are typically manufactured from diamond and their shape remains unchanged upon tip cleaning. A nanoindenter (NI) has built-in routines to calibrate a complex (non-spherical) tip including its apex and its pyramid base described by a 6-parameter area function. The nanoindenter tip is mounted on a stylus and typically penetrates the tested material while the AFM tip is mounted on a cantilever and operates in a regime of elastic deformation of the sample surface. While a sharp tip is advantageous for both instruments to reduce the adhesion forces when in contact and obtain high spatial resolution maps, a blunt tip radius is necessary for accurate mechanical measurements to focus on the repulsive forces of the surface. A small sideways motion of the tip on an AFM cantilever could be a concern for large deformations, however in nanoindentation, the tip dragging laterally on the surface is <0.5 nm, out of the 60 nm vertical motion. Characteristic differences between the nanoindenter and the AFM used in this work are summarized in **Table 2**.

Table 2. Comparison between the salient characteristics of nanoindentation and AFM.

Parameter	Nanoindentation	AFM
Tip radius	50 nm	30 nm
Frequency range	0.1–300 Hz	0.1 Hz to 6 MHz
Force noise floor	30 nN	Few piconewtons
Max force during experiment	Few micronewtons	80 nN

Bruker's TI 980 nanoindenter used in the present experiments was equipped with a sharp diamond indenter tip with a cube corner geometry and a radius of ≈50 nm. The tip shape was calibrated by routines described in the instrument's user manual and in ISO14577 for the depth range between 5 and 150 nm. Indentation experiments were performed on virgin positions of each polymer sample. The tip oscillated at a frequency of 20 Hz with an amplitude of ≈2 nm while approaching the sample. The surface of the sample was determined at the displacement position at which the contact stiffness began rising. The amplitude and phase of the oscillation was measured by a lock-in amplifier and then analyzed following earlier work.[39–41]

The mechanical properties of the polymers investigated in this work, determined as a function of penetration depth, are shown in **Figure 5**. The properties of the thin polymer films on the hard substrate can be discussed starting from a penetration depth of 5 nm—the lower end of calibration of the tip shape. The sharp cube corner indenter allows measuring the properties of the polymer without a pronounced substrate effect and the film properties of each sample should be read from the plateau region starting above 5 nm. The hardness peak at low penetration depth is often called skin effect—attributing higher properties to the surface skin of polymers—there are however other effects to be considered before the observation can be attributed to a different cross-linking of polymers in the skin. Hardness is understood as the average stress in the contact zone and can be overestimated because the adhesive forces that act in the contact zone are not fully measurable with the indenter-force-sensor. Moreover, the material experiences the highest strain rates at the initial penetration depth and a strain rate sensitive polymer requires higher stresses to be deformed at higher strain rates. The measured nanomechanical parameters using the indenter are typically lower than the measurements performed with the AFM. The difference is linked to the different frequency regime of testing namely, 2 kHz on the AFM versus 20 Hz on the nanoindenter. Nevertheless, at 20 Hz, the viscoelastic properties are probed with higher fidelity, as the polymer's tactile response upon slow tapping can be measured more accurately.

Figure 5a shows a comparison between the hardness of the polymers as a function of penetration depth studied under nanoindentation. The overall trend as measured by the AFM continues to be preserved in this regime of low tapping at 20 Hz, with the exception that the doped polymer C14-PBTTT is the least hard. The slight rise in the hardness of C16-IDTBT at higher penetration depths as seen in Figure 5a is possibly because the film retains more residual solvent in its bulk during processing, thus causing substrate effects to kick in earlier. Figure 5b–d shows a comparison between the viscoelastic

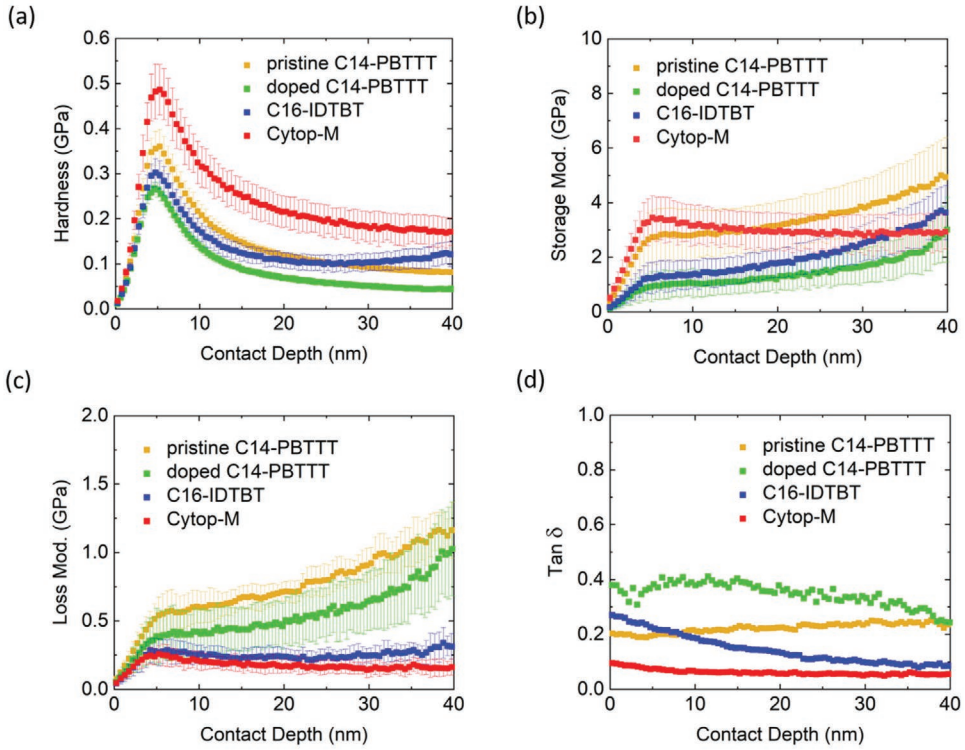

Figure 5. Nanoscale dynamical mechanical analysis of pristine C14-PBTTT, doped C14-PBTTT, C16-IDTBT and Cytop-M performed using Bruker's TI 980 TriboIndenter. a) Hardness, b) storage modulus, c) loss modulus, and d) tan δ.

properties, that is, the storage modulus, loss modulus, and the loss tangent, tan δ, of the polymers in question. Cytop-M, being an order of magnitude thicker than the other organic polymer films at a thickness of 500 nm, shows the most robust measured plateaus arguably because substrate effects do not kick in at these penetration depths. The loss tangent tan δ is the highest for the doped C14-PBTTT film. This observation leads one to understand that although the doping process causes an increase in conductivity which is a positive for electrical applications, it is accompanied by higher viscoelastic/mechanical losses, a property that needs to be considered when deploying such doped polymers in mechanical resonators. Furthermore, a higher tan δ at the surface of the doped C14-PBTTT film illustrates that the viscous response is more important at low contact depths than it is for pristine C14-PBTTT. Since the tan δ curves for pristine C14-PBTTT and doped C14-PBTTT approach each other at higher contact depths, it appears that the bulk is not affected to the same extent by doping, or that substrate effects are observed. The reduction in the tan δ of C16-IDTBT as a function of contact depth suggests that the indenter probe squeezes the film, displacing the residual solvent in the bulk under the probe in the process. This causes a reduction in the viscoelastic losses as the film is compacted under the probe tip.

In addition to film penetration, the nanoindenter was also used in its sensitive scanning probe microscopy mode to map the topographical differences between pristine C14-PBTTT and doped C14-PBTTT. Using this nanoindenter-based scanning probe microscopy mode, the topographical roughness as measured in the two films using the AFM were reconfirmed (see Section S9, Supporting Information).

4. Conclusions

Micromechanical and electromechanical devices built using organic electronic polymers necessitate a greater understanding of the active layer's mechanical properties on the grain-scale and the nanoscale. In this work, we use precision instrumentation techniques to compare the nanomechanical properties of organic polymers that commonly constitute the layers in a polymer thin film transistor. We contrast two well-known organic polymer semiconductors on the grounds of their mobility, morphology, modulus, modulus homogeneity, and their low-frequency viscoelastic response. Our study focuses primarily on quantifying nanomechanical texture on length scales spanning several tens of nanometers to several hundred nanometers, as these dimensions are directly applicable within micromechanical resonators. On said length scales, the high-mobility organic polymer C16-IDTBT shows a greater spatial homogeneity in its modulus compared with the high-mobility organic polymer C14-PBTTT. As C14-PBTTT can be chemically doped efficiently, we studied the influence of doping on the modulus and showed that the process is accompanied by a lower average modulus with improved spatial homogeneity compared to its pristine counterpart. Although doping increases the electrical conductivity of the film, its mechanical losses also increase. The latter is a finding that needs to be accounted for in electromechanical devices based on conductive organic polymers.

Supporting Information

Supporting Information is available from the Wiley Online Library or from the author.

Acknowledgements

D.V. acknowledges the Royal Society for funding in the form of a Royal Society University Research Fellowship (Royal Society Reference No. URF\R1\201590). D.V. is thankful to Henning Sirringhaus for having facilitated this work by providing a cleanroom and a nitrogen glovebox deposition facility to deposit the high purity organic thin films analyzed in this study. D.V. is also thankful to Iain McCulloch for having supplied C14-PBTTT and C16-IDTBT used in this work. D.S. acknowledges support from the Sensor CDT and the Engineering and Physical Sciences Research Council (Grant No. EP/L015889/1). G.S. acknowledges postdoctoral fellowship support from the Belgian National Fund for Scientific Research (FNRS).

Conflict of Interest

The authors declare no conflict of interest.

Author Contributions

V.P., I.D., and U.D.H. contributed equally to this work. V.P. and I.D. performed the PeakForce Quantitative Nanomechanical Mapping measurements on the three organic polymers using a Bruker Dimension IconXR AFM and a Bruker FastScan AFM. U.D.H. performed the viscoelastic characterization using Bruker's TI 980 TriboIndenter. D.S. and D.V. fabricated the organic polymer thin films and devices used in this study and engaged in regular discussions on the interpretation of the experimental measurements. L.J.S. acted as a sounding board for the ideas presented in the paper, engaged in regular discussions on the interpretation of the experimental measurements and provided regular critical feedback on the manuscript. G.S. and I.E.J. contributed to discussions and experimental work on the doping properties of organic semiconductors. P.M.C. and D.V. coordinated and supervised the collaboration between KTH Stockholm and the University of Cambridge. D.V. conceived the idea of measuring and comparing the nanoscale properties of organic semiconducting polymers and wrote the final manuscript together with U.D.H.

Data Availability Statement

The data that support the findings of this study are available from the corresponding author upon reasonable request.

Keywords

nanomechanics, organic electronics, organic field-effect transistors, organic semiconducting polymers, young's modulus

Received: September 22, 2021
Revised: October 27, 2021
Published online: November 25, 2021

[1] S. Chung, K. Cho, T. Lee, *Adv. Sci.* **2019**, *6*, 1801445.
[2] U. Zschieschang, H. Klauk, *J. Mater. Chem. C* **2019**, *7*, 5522.

[3] D. Corzo, G. Tostado-Blázquez, D. Baran, *Front. Electron.* **2020**, *1*, 594003.
[4] S. E. Root, S. Savagatrup, A. D. Printz, D. Rodriquez, D. J. Lipomi, *Chem. Rev.* **2017**, *117*, 6467.
[5] Y. Liu, J. Liu, S. Chen, T. Lei, Y. Kim, S. Niu, H. Wang, X. Wang, A. M. Foudeh, J. B.-H. Tok, Z. Bao, *Nat. Biomed. Eng.* **2019**, *3*, 58.
[6] D. Khodagholy, J. N. Gelinas, T. Thesen, W. Doyle, O. Devinsky, G. G. Malliaras, G. Buzsáki, *Nat. Neurosci.* **2015**, *18*, 310.
[7] J. E. Chung, H. R. Joo, J. L. Fan, D. F. Liu, A. H. Barnett, S. Chen, C. Geaghan-Breiner, M. P. Karlsson, M. Karlsson, K. Y. Lee, H. Liang, J. F. Magland, J. A. Pebbles, A. C. Tooker, L. F. Greengard, V. M. Tolosa, L. M. Frank, *Neuron* **2019**, *101*, 21.
[8] K. A. Ludwig, J. D. Uram, J. Yang, D. C. Martin, D. R. Kipke, *J. Neural Eng.* **2006**, *3*, 59.
[9] A. Carnicer-Lombarte, S.-T. Chen, G. G. Malliaras, D. G. Barone, *Front. Bioeng. Biotechnol.* **2021**, *9*, 622524.
[10] Z. Ma, S. Li, H. Wang, W. Cheng, Y. Li, L. Pan, Y. Shi, *J. Mater. Chem. B* **2019**, *7*, 173.
[11] E. Musk, Neuralink, *J. Med. Internet Res.* **2019**, *21*, e16194.
[12] M. Sanviti, A. Alegria, D. E. Martínez-Tong, *ChemRxiv* **2021**, https://doi.org/10.26434/chemrxiv.14135315.v1.
[13] L. Ouyang, C.-C. Kuo, B. Farrell, S. Pathak, B. Wei, J. Qua, D. C. Martin, *J. Mater. Chem. B* **2015**, *3*, 5010.
[14] D. M. DeLongchamp, R. J. Kline, E. K. Lin, D. A. Fischer, L. J. Richter, L. A. Lucas, M. Heeney, I. McCulloch, J. E. Northrup, *Adv. Mater.* **2007**, *19*, 833.
[15] I. McCulloch, M. Heeney, M. L. Chabinyc, D. DeLongchamp, R. J. Kline, M. Colle, W. Duffy, D. Fischer, D. Gundlach, B. Hamadani, R. Hamilton, L. Richter, A. Salleo, M. Shkunov, D. Sparrowe, S. Tierney, W. Zhang, *Adv. Mater.* **2009**, *21*, 1091.
[16] D. Venkateshvaran, M. Nikolka, A. Sadhanala, V. Lemaur, M. Zelazny, M. Kepa, M. Hurhangee, A. J. Kronemeijer, V. Pecunia, I. Nasrallah, I. Romanov, K. Broch, I. McCulloch, D. Emin, Y. Olivier, J. Cornil, D. Beljonne, H. Sirringhaus, *Nature* **2014**, *515*, 384.
[17] W. M. Zhang, J. Smith, S. E. Watkins, R. Gysel, M. McGehee, A. Salleo, J. Kirkpatrick, S. Ashraf, T. Anthopoulos, M. Heeney, I. McCulloch, *J. Am. Chem. Soc.* **2010**, *132*, 11437.
[18] X. Zhang, H. Bronstein, A. J. Kronemeijer, J. Smith, Y. Kim, R. J. Kline, L. J. Richter, T. D. Anthopoulos, H. Sirringhaus, K. Song, M. Heeney, W. Zhang, I. McCulloch, D. M. DeLongchamp, *Nat. Commun.* **2013**, *4*, 2238.
[19] D. Simatos, L. J. Spalek, U. Kraft, M. Nikolka, X. Jiao, C. R. McNeill, D. Venkateshvaran, H. Sirringhaus, *APL Mater.* **2021**, *9*, 041113.
[20] B. O'Connor, E. P. Chan, C. Chan, B. R. Conrad, L. J. Richter, R. J. Kline, M. Heeney, I. McCulloch, C. L. Soles, D. M. DeLongchamp, *ACS Nano* **2010**, *4*, 7538.
[21] T. J. Young, M. A. Monclus, T. L. Burnett, W. R. Broughton, S. L. Ogin, P. A. Smith, *Meas. Sci. Technol.* **2011**, *22*, 125703.
[22] P. M. Claesson, I. Dobryden, G. Li, Y. He, H. Huang, P.-A. Thoren, D. B. Haviland, *Phys. Chem. Chem. Phys.* **2017**, *19*, 23642.
[23] R. Garcia, *Chem. Soc. Rev.* **2020**, *49*, 5850.
[24] S. E. Root, N. E. Jackson, S. Savagatrup, G. Arya, D. J. Lipomi, *Energy Environ. Sci.* **2017**, *10*, 558.
[25] H.-C. Tien, Y.-W. Huang, Y.-C. Chiu, Y.-H. Cheng, C.-C. Chueh, W.-Y. Lee, *J. Mater. Chem. C* **2021**, *9*, 2660.
[26] B. D. Vogt, *J. Polym. Sci. Part B: Polym. Phys.* **2018**, *56*, 9.
[27] D. Tranchida, S. Piccarolo, J. Loos, A. Alexeev, *Macromolecules* **2007**, *40*, 1259.
[28] I. McCulloch, M. Heeney, C. Bailey, K. Genevicius, I. MacDonald, M. Shkunov, D. Sparrowe, S. Tierney, R. Wagner, W. Zhang, M. L. Chabinyc, R. J. Kline, M. D. McGeehee, M. F. Toney, *Nat. Mater.* **2006**, *5*, 328.
[29] J.-F. Chang, M. C. Gwinner, M. Caironi, T. Sakanoue, H. Sirringhaus, *Adv. Funct. Mater.* **2010**, *20*, 2825.
[30] C. Cendra, L. Balhorn, W. Zhang, K. O'Hara, K. Bruening, C. J. Tassone, H.-G. Steinrück, M. Liang, M. F. Toney, I. McCulloch, M. L. Chabinyc, A. Salleo, C. J. Takacs, *ACS Macro Lett.* **2021**, *10*, 1306.
[31] H. Maddali, K. L. House, T. J. Emge, D. M. O'Carroll, *RSC Adv.* **2020**, *10*, 21454.
[32] I. E. Jacobs, Y. Lin, Y. Huang, X. Ren, D. Simatos, C. Chen, D. Tjhe, M. Statz, L. Lai, P. A. Finn, W. G. Neal, G. D'Avino, V. Lemaur, S. Fratini, D. Beljonne, J. Strzalka, C. B. Nielsen, S. Barlow, S. R. Marder, I. McCulloch, H. Sirringhaus, *Adv. Mater.* **2021**, 2102988.
[33] M. L. Chabinyc, R. A. Street, J. E. Northrup, *Appl. Phys. Lett.* **2007**, *90*, 123508.
[34] P. Boufflet, Y. Han, Z. Fei, N. D. Treat, R. Li, D.-M. Smilgies, N. Stingelin, T. D. Anthopoulos, M. Heeney, *Adv. Funct. Mater.* **2015**, *25*, 7038.
[35] M. Nikolka, I. Nasrallah, B. Rose, M. K. Ravva, K. Broch, A. Sadhanala, D. Harkin, J. Charmet, M. Hurhangee, A. Brown, S. Illig, P. Too, J. Jongman, I. McCulloch, J.-L. Bredas, H. Sirringhaus, *Nat. Mater.* **2017**, *16*, 356.
[36] W.-C. Liao, B. H. Liu, C.-C. Leu, *Appl. Surf. Sci.* **2020**, *507*, 1450782.
[37] I. Mela, C. Puudel, M. Anaya, G. Delport, K. Frohna, S. Macpherson, T. A. S. Doherty, A. Scheeder, S. D. Stranks, C. F. Kaminski, *Adv. Funct. Mater.* **2021**, *31*, 2100293.
[38] Y. Zheng, G.-J. N. Wang, J. Kang, M. Nikolka, H.-C. Wu, H. Tran, S. Zhang, H. Yan, H. Chen, P. Y. Yuen, J. Mun, R. H. Dauskardt, I. McCulloch, J. B.-H. Tok, X. Gu, Z. Bao, *Adv. Funct. Mater.* **2019**, *29*, 1905340.
[39] S. A. S. Asif, K. J. Wahl, R. J. Colton, *Rev. Sci. Instrum.* **1999**, *70*, 2408.
[40] S. A. S. Asif, K. J. Wahl, R. J. Colton, *J. Mater. Res.* **2000**, *15*, 546.
[41] S. A. S. Asif, K. J. Wahl, R. J. Colton, O. L. Warren, *J. Appl. Phys.* **2001**, *90*, 1192.

ADVANCED SCIENCE Open Access
www.advancedscience.com

Giant Increase of Hardness in Silicon Carbide by Metastable Single Layer Diamond-Like Coating

*Martin Rejhon, Xinliu Zhou, Francesco Lavini, Alessandra Zanut, Filip Popovich, Lorenzo Schellack, Lukasz Witek, Paulo Coelho, Jan Kunc, and Elisa Riedo**

Silicon carbide (SiC) is one of the hardest known materials. Its exceptional mechanical properties combined with its high thermal conductivity make it a very attractive material for a variety of technological applications. Recently, it is discovered that two-layer epitaxial graphene films on SiC can undergo a pressure activated phase transition into a sp^3 diamene structure at room temperature. Here, it is shown that epitaxial graphene films grown on SiC can increase the hardness of SiC up to 100% at low loads (up to 900 µN), and up to 30% at high loads (10 mN). By using a Berkovich diamond indenter and nanoindentation experiments, it is demonstrated that the 30% increase in hardness is present even for indentations depths of 175 nm, almost three hundred times larger than the graphene film thickness. The experiments also show that the yield point of SiC increases up to 77% when the SiC surface is coated with epitaxial graphene. These improved mechanical properties are explained with the formation of diamene under the indenter's pressure.

1. Introduction

Graphene has shown great potential for mechanical applications due to its exceptional mechanical properties.[1–5] Recent investigations of mechanically exfoliated monolayer graphene membranes by atomic force microscopy (AFM) showed extremely high in-plane stiffness (≈1 TPa) and membrane strength ≈100 GPa.[1] However, experiments on graphene grown by chemical vapor deposition (CVD) on a copper substrate showed no increase in hardness of the graphene coated copper substrate.[6] Regarding the stiffness of substrates coated with graphene, no increase has been detected for exfoliated graphene on SiO_2 substrates,[7] while a 5% increase has been measured for copper coated with CVD compared to bare copper.[6] For a copper substrate coated with graphene, a mild increase in bearing capacity has been shown during the initial elastic regime at low loads.[8]

Very recently it has been reported that two-layer epitaxial graphene grown on silicon carbide (SiC) can undergo a room temperature, pressure activated phase transition from sp^2 to sp^3 hybridization. This phase transition dramatically changes the elastic properties of the graphene/SiC system under pressure.[7,9–11] In particular, purely elastic ångström indentation (Å-indentation) measurements indicated a surface stiffness comparable to diamond, while no investigations on the plastic behavior have been performed.[7,9,10,12]

Silicon carbide is considered one of the best materials for protection against high-speed impacts and for body armor applications[13] due to its extreme hardness, strength, and high thermal conductivity. Considering the technological interest in the exceptional mechanical properties of SiC, second only to diamond, here, we investigate how the hardness of a SiC substrate can be further improved when SiC is coated with an atomically thin and thermally conductive epitaxial graphene film. In particular, we conduct Berkovich hardness indentation tests on monolayer (1L) epitaxial graphene films grown on the Si-face of SiC(0001),[14] where a typical buffer carbon layer (BfL) sits in between graphene and SiC[14] (see 1L/BfL/SiC in **Figure 1**a); in addition, we investigate H-terminated SiC(0001) coated with 2L quasi-free-standing epitaxial graphene films[15,16] (see 2L/H-SiC in Figure 1a), and finally we compare the results with a bare SiC(0001) substrate, see the Experimental Section for

M. Rejhon, X. Zhou, F. Lavini, A. Zanut, F. Popovich, L. Schellack, E. Riedo
Department of Chemical and Biomolecular Engineering
Tandon School of Engineering
New York University
Brooklyn, NY 11201, USA
E-mail: elisa.riedo@nyu.edu

L. Witek, P. Coelho
Division of Biomaterials
Department of Molecular Pathobiology
New York University College of Dentistry
New York, NY USA

J. Kunc
Charles University
Faculty of Mathematics and Physics
Institute of Physics
Ke Karlovu 5, Prague 2, Prague CZ-121 16, Czech Republic

E. Riedo
Department of Physics
New York University
Brooklyn, NY 11201, USA

The ORCID identification number(s) for the author(s) of this article can be found under https://doi.org/10.1002/advs.202204562

DOI: 10.1002/advs.202204562

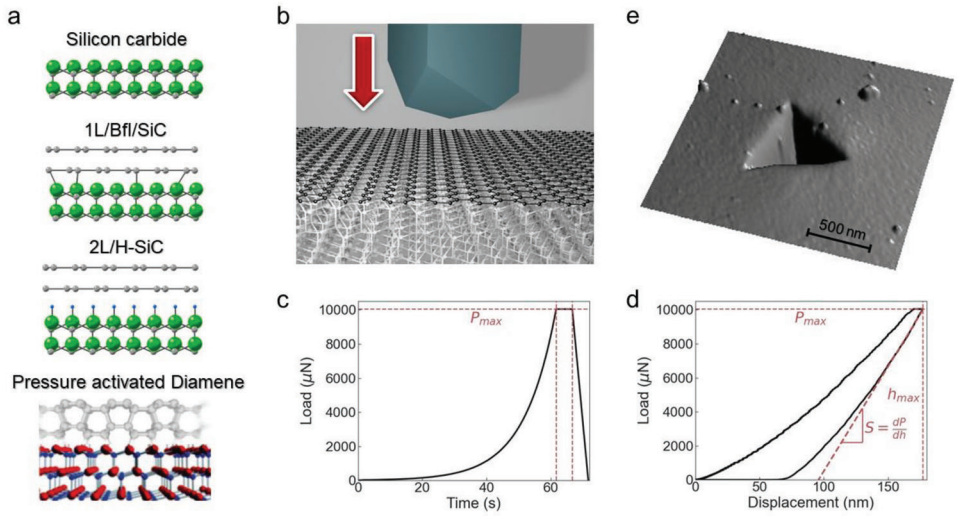

Figure 1. Nanoindentation experiment. a) Schemes of the investigated samples, namely bare silicon carbide, one epitaxial graphene on the carbon buffer layer on silicon face of SiC, and quasi free-standing bilayer graphene on silicon face of SiC after hydrogen intercalation, and the scheme of pressure activated diamene structure.[9,11] b) Scheme of the nanoindentation experiments with a diamond Berkovich tip. c) Nanoindentation experiment consists of three stages, first loading part with the constant strain rate, second stage when the maximal load is held and the third unloading stage while the load is linearly decreased. d) The obtained load-displacement curve from the nanoindentation experiment. e) Residual imprint on the surface after nanoindentation experiment.

more details on the samples. The experiments show up to 100% increase in hardness, and 80–50% increase in elastic modulus when SiC is coated with 1 L epitaxial graphene plus buffer layer, or with 2 L quasi-free-standing graphene compared to bare SiC at low loads (up to 900 μN). This increase levels off to ≈30% when indentation loads are 10 mN, and indentations depths reach 175 nm. Furthermore, we demonstrate that the minimum pressure leading to residual plastic indents, i.e., the yield point, increases by 77% when SiC is coated with epitaxial graphene films. These results can be explained by the pressure activated sp^2 to sp^3 phase transition occurring in two-layer epitaxial graphene on SiC when a Berkovich tip indents the system and forms a diamond layer, called diamene[11] (Figure 1a). Importantly, previous Å-indentation measurements indicated that diamene was ultra-stiff, however the indentations used to determine the stiffness of diamene were <1 Å.[7,9,10] Here, we show that the atomically thin diamene layer can improve the mechanical properties of SiC even at high loads, corresponding to indentations three hundred times larger than the graphene film thickness. Furthermore, this work suggests that the phase transition can occur also over large areas for large indenters, here at least μm^2 areas. These findings are promising for future applications in high-impact protective coatings, body armors production, and for use in aeronautics, aerospace, and automobile industry.

2. Results and Discussion

The hardness H and elastic modulus E of bare and graphene coated 6H-SiC (0001) substrates are investigated by indentation experiments using a Hysitron TI 950 Triboindenter with a diamond Berkovich indenter, applying loads in the range between 300 μN and 10 mN (Figure 1b). During the indentation experiments, the indenter is brought into contact with the surface of the investigated sample while increasing the normal force at a constant rate until a given maximum load is achieved, then the maximum load is held for a certain amount of time, and in the final stage, the load is decreased linearly with time, see Figure 1c. In the experiments, the load and the indentation depth are measured and recorded simultaneously. During the loading part, the Berkovich indenter induces elastic and/or plastic deformations; during the unloading part, the elastic deformation can be fully restored (Figure 1d), therefore a residual imprint of the indenter shape on the sample surface (Figure 1e) remains only if plastic deformations occur during the loading part. The hardness is estimated from the unloading part of the indentation curves using the Oliver–Pharr method[17] (see Experimental Section) and plotted as a function of the applied load in **Figure 2**a. The corresponding load displacement curves are shown in the supplementary information (see Figures S2–S4, Supporting Information). The indenter shape and the indentation projected area needed for the Oliver–Pharr method[17] are calibrated based on the known hardness of the bare SiC sample, which is 30 GPa[18–21] (see Experimental Section and Supporting Information). For example, Shaffer et al.[21] obtained a hardness of ≈30 GPa along the c-axis using a Knoop indenter, and Henshall et al.[20] obtained hardness values of ≈30 GPa in the (0001) direction using a Berkovich indenter. In Figure 2a, along with the results on bare SiC, we also report the measured hardness of graphene coated SiC samples, namely 1L/BfL/SiC and 2L/H-SiC (see Figure 1a). The measurements show higher values of hardness in graphene coated SiC compared to bare SiC(0001) in the whole range of investigated loads. Very importantly, at loads lower than 500 μN, the load-indentation curves do not indicate any plastic deformation in the case of 1L/Bfl/SiC(0001) and 2L/H-SiC(0001), as can be seen in Figure 2b (more curves can be found in Figures S2–S4, Supporting Information), showing a higher ability of graphene coated SiC to withstand higher pressures before yielding. These results are attributed to the local formation of diamene,[9,10] induced by the

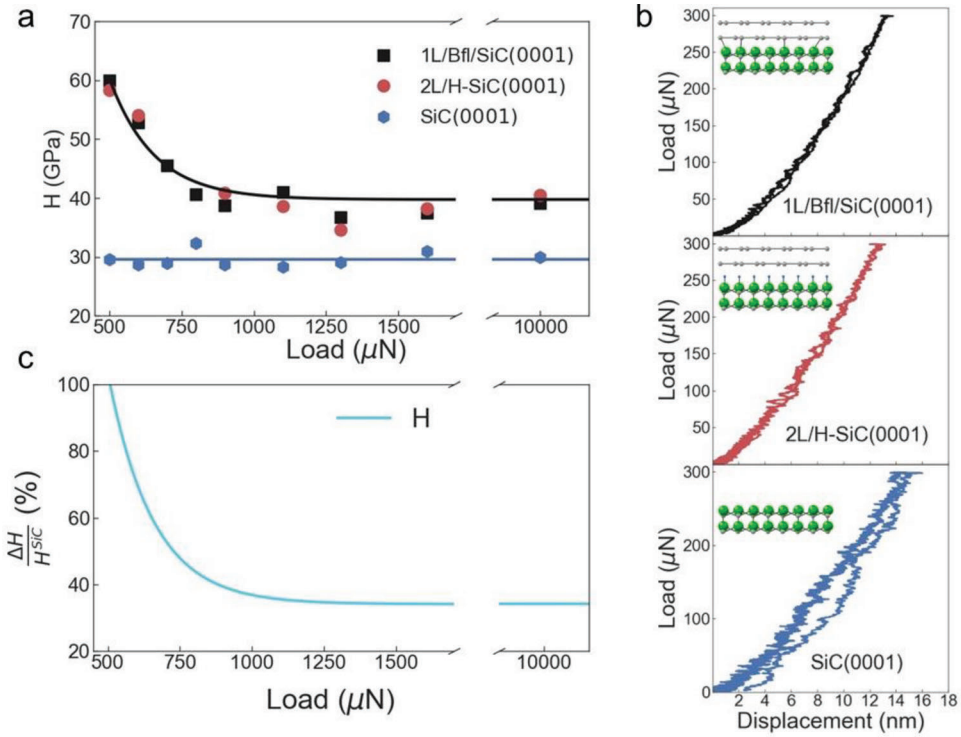

Figure 2. Hardness determined by Oliver-Pharr method. a) Average hardness dependency on the applied load for different samples. Experimental average data are shown as markers and solid lines represent fit with an exponential decay function as a guide for the eye. b) The load displacement curves at 300 μN showing no plastic deformation in case of SiC samples coated with epitaxial graphene. c) The percentage change in hardness between graphene coated and bare SiC.

pressure activated sp^2 to sp^3 phase transition in the two graphitic layers under the indenter. This 2D diamond-like structure on SiC increases the resistance of SiC to yield compared to bare SiC, resulting in higher hardness. On the other hand, previous theoretical work[9] predicts no graphene-diamene phase transition at room temperature for >3 L. Indeed, we find that when SiC is coated with 10 L of epitaxial graphene, the hardness decreases of ≈88% compared to bare SiC. This is also in agreement with previous studies that did not show any improvement in the hardness of copper when coated with only one layer of CVD graphene.[6] The increased hardness of the 1L/Bfl/SiC(0001) system is consistent with a coating harder than the SiC substrate.[22] The hardness of the graphene/SiC composite structure decreases with increasing loads, reaching a plateau value of ≈40 GPa at 10 mN loads, a value which is 30% larger than the hardness of bare SiC at the same load and closer to the hardness of diamond, i.e., 60–150 GPa.[23] Furthermore, compared to bare SiC, the hardness of 1L/Bfl/SiC(0001) and 2L/H-SiC(0001) at lower loads, e.g. 500 μN, displays an incredible increase of up to 100%, compared to bare SiC, reaching values of 60 GPa (see Figure 2c). Importantly, previous experiments indicated that diamene was ultra-stiff; however, the indentations used to determine the stiffness of diamene were <1 Å. On the other hand, here, we show that the atomically thin diamene layer can improve the mechanical properties of SiC even at high loads, corresponding to indentations of ≈175 nm, i.e., almost three hundred times larger than the graphene film thickness. Furthermore, the measurements show improved hardness and stiffness even when using a large Berkovich indenter, as opposed to a 10 nm AFM indenter used in previous studies,[9,10] suggesting that the phase transition can occur over large areas, in this work areas up to μm^2 have been probed, as shown in Figure 1e.

The hardness values presented in Figure 2 have been obtained using the Oliver–Pharr method, to confirm these results, we also perform AFM measurements of the projected area of the residual indentations at selected loads of 900, 1100, 1300, 1600, and 10 mN (see **Figure 3**a). In particular, in the range between 900 and 1600 μN, for which the projected area of the residual indentations is well defined in the AFM maps, we evaluate hardness and elastic modulus for all samples (see Figure 3b,c). By comparing the results in Figures 2, and 3 it is clear that the two methods give consistent hardness results. Regarding the elastic modulus, we find that the Young's modulus of SiC coated with epitaxial graphene is ≈750 GPa when the load is 900 μN, while at the same load the Young's modulus of bare SiC is 400 GPa, in agreement with values reported in literature.[19,24] At larger loads, the difference between bare and graphene coated SiC decreases, showing only a 30% increase at 10 mN. The large increase in indentation elastic modulus up to ≈0.7 TPa for graphene coated SiC, at loads as large as 1 mN, is quite surprising considering that at these loads the indenter penetrates 30–40 nm, a depth ≈60 times larger than the thickness of the graphene film. To investigate the stress distribution in the samples, we conducted finite element simulations of the plastic deformation of bare silicon carbide and silicon carbide covered with a five angstroms thick diamond film; the results are reported in Figure S12 (Supporting Information).

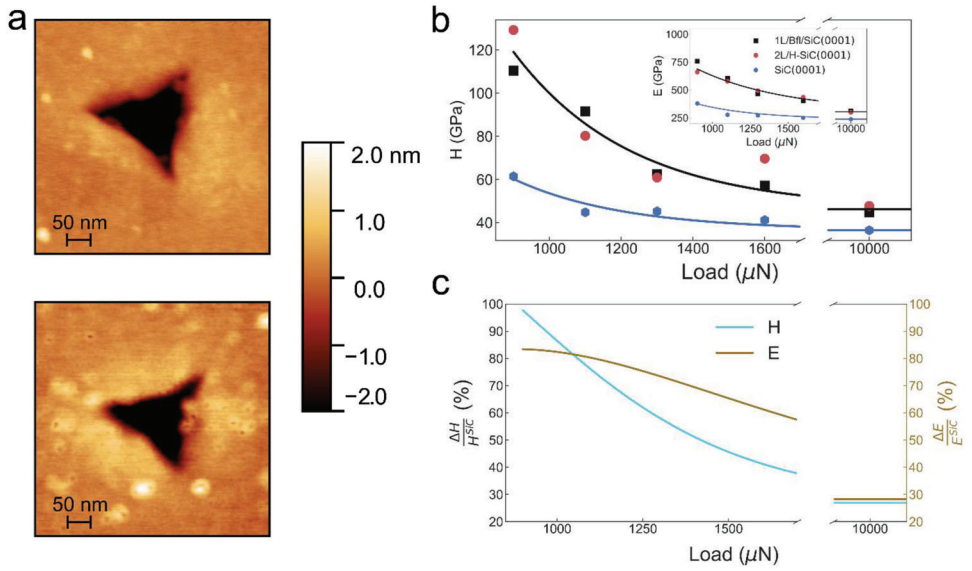

Figure 3. Hardness and Young's modulus determined by AFM imaging of residual indentations. a) Images of residual indentations on the surface of a bare SiC sample and 2L/H-SiC sample for a load of 1600 μN. b) Hardness evaluated from the AFM topographical images of residual indentations for different samples in the range between 900 and 1600 μN, and 10 mN. The determined Young's modulus is shown in the inset. Experimental data are shown as markers and solid lines represent fit with an exponential decay function as a guide for the eye. c) The percentage change in hardness (blue line) and Young's modulus (gold line) between graphene coated and bare SiC.

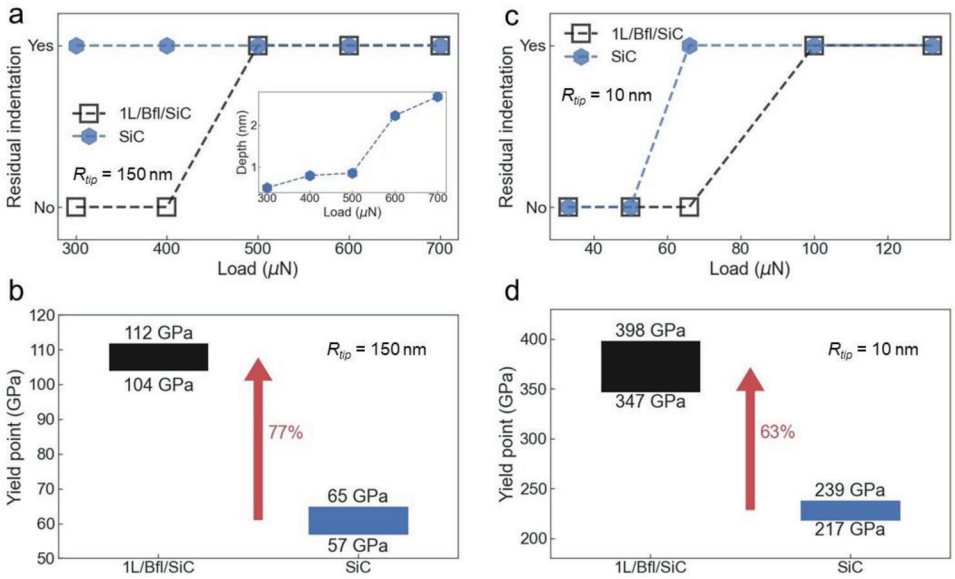

Figure 4. Onset of plastic deformation and yield point. a) Presence of residual indentations after triboindentation tests with Berkovich tip (R = 150 nm) on bare SiC(0001) and 1L/Bfl/SiC(0001) samples in the applied load range between 300 and 700 μN. b) Calculated yield point from the Figure 4a showing an increase of ≈77% for 1L/Bfl/SiC sample compared to bare SiC. c) Presence of residual indentations after nanoindentation tests with a diamond AFM tip with radius of 10 nm in the range of applied load between 35 and 140 μN. d) Corresponding yield point for AFM nanoindentation tests showing an increase of ≈63% for 1L/Bfl/SiC sample compared to bare SiC.

Furthermore, we investigate the presence of residual indentations at low loads (300–700 μN) on the surface of bare SiC(0001) and graphene coated SiC to determine the onset of plastic deformation. Interestingly, we observe residual indentations on the surface of bare SiC for all loads, while no residual indentations are present on the surface of 1L/Bfl/SiC at loads 300 and 400 μN (see **Figure 4**a), in perfect agreement with the behavior of the load displacement curves (see Figure 2b). The first residual indentation is visible on the surface of 1L/Bfl/SiC only after indentation experiments at 500 μN. Figure 4b shows the corresponding calculated yield points Y, defined as the pressure at which the sample starts to undergo a plastic deformation, and obtained from the

values of the maximum load without a residual indentation and the minimum load with a residual indentation on the sample's surface using the following equation:

$$Y = \frac{1}{\pi}\left(\frac{6F_Y E_r^2}{R^2}\right)^{\frac{1}{3}} \quad (1)$$

where R is the radius of the indenter and E_r is the relative elastic modulus. The yield point varies between the 57 GPa and 65 GPa for bare SiC, while for graphene coated SiC, the yield point is between 104 and 112 GPa, corresponding to an astonishing increase of ≈77% compared to bare SiC. To study the role of the indent size, we perform nanoindentation experiments when the sample surface is indented with a diamond AFM tip with a radius of 10 nm. Figure 4c shows that for this indenter size, residual indentations appear at 58 ± 8 µN for bare SiC, while the 1L/Bfl/SiC sample begins to yield at 83 ± 17 µN, resulting into a yield point between 217 and 239 GPa for bare SiC, and between 347 and 398 GPa for 1L/Bfl/SiC. The values of yield point obtained with a smaller indenter (10 nm) are significantly higher than those obtained with a larger indenter (150 nm), in agreement with previous studies,[25] this effect may be driven by a difference in the gradient of deformation outside the indenters, and the need for more geometrically necessary dislocations in the case of sharper indenters.[26] However, for both indenter sizes the percentage increase in yield point for 1L/Bfl/SiC compared to bare SiC exhibits similar values, specifically 77% for the triboindenter experiment (150 nm radius), and 63% for the AFM nanoindentation experiment (10 nm).

To corroborate the finding that under a localized load 1L graphene plus buffer layer undergoes a phase transition to a diamond-like structure, we used a conductive AFM (c-AFM) probe to apply a local load and simultaneously measure the electronic current flowing through the AFM tip-sample contact, see **Figure 5**. We expect an increase in resistivity (decrease of current) when the load is enough high to activate the graphene-diamene phase transition. As can be seen in Figure 5, the current increases with increasing normal force (because the contact areas increase with load) until the normal force reaches 175 nN. Then the current decreases with increasing force until reaching the maximal force of 250 nN. The same behavior occurs during the unloading part with a peak at 200 nN. These results demonstrate that for a diamond AFM tip having a radius ≈10 nm, the phase transition occur ≈175 nN. We also remark that this phase transition is metastable. Based on our previous studies and the above reported c-AFM measurements, diamene formation is pressure-induced and once pressure is released the created sp^3 hybridization switch back into sp^2 hybridization.

3. Conclusion

In conclusion, motivated by the recent discovery of a room temperature pressure activated phase transition of epitaxial graphene into a sp^3 diamene structure, we have investigated the hardness of single crystal SiC coated with epitaxial graphene films. We find that when SiC is coated with 10L of epitaxial graphene, the hardness decreases of ≈88% compared to bare SiC. However, when SiC is coated with a 1 L epitaxial graphene plus a graphene-like buffer layer, or two graphene layers (in this case the SiC surface is passivated with hydrogen), we observe a dramatic increase in hardness. Precisely, we observe that coating SiC with 1L graphene plus buffer layer can increase the hardness of up to 100% at low loads (between 500 and 900 µN) compared to bare SiC, increasing from 30 to 60 GPa, a value approaching the hardness of diamond. This increase in hardness falls off at high loads, reaching a plateau value of 30% at 10 mN. The experiments also show that the yield point and onset of plastic deformations in SiC increases up to 77% when the SiC surface is coated with epitaxial graphene. These findings shed light on the formation of diamene under the indenter's pressure. In particular, we show that the atomically thin diamene layer can improve hardness of SiC even at high loads, corresponding to indentations of ≈175 nm, i.e., almost 300 times larger than the graphene film thickness. This work opens new possibilities for designing ultra-hard and ultra-light thermally conductive coatings for SiC to improve its mechanical performances for applications such as body armors, high-impact protective coatings, and for use in aeronautics, aerospace, and automobile industry.

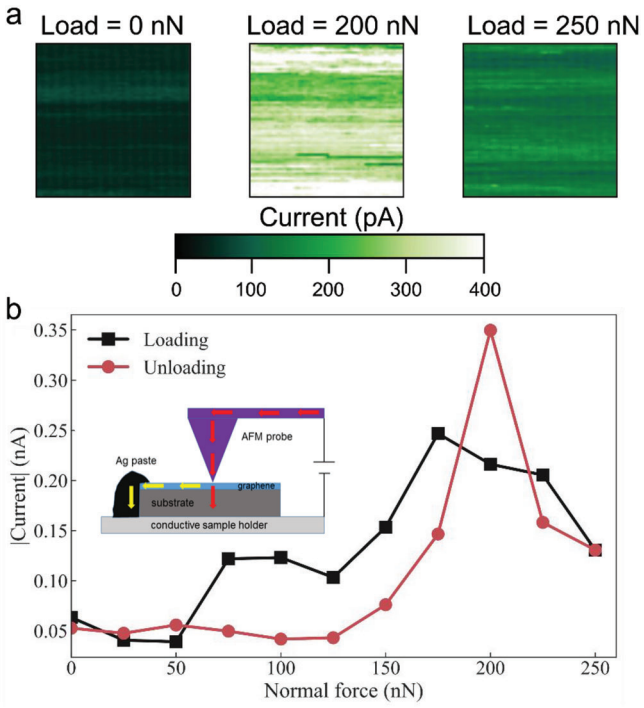

Figure 5. C-AFM measurements. a) c-AFM maps taken at loads of 0, 200, and 250 nN on a 1L/Bfl/SiC(0001) sample with a bias of −4 mV. b) The current signal (average current values measured in 1 nm^2 squares similar to the ones shown in (a)) versus normal force, measured with c-AFM on a 1L/Bfl/SiC(0001) sample during loading the AFM tip (black squares and curve) and unloading the AFM tip (red circles and curve). The sample was biased at −4 mV. In the inset we show a cartoon of the experimental setup.

4. Experimental Section

Preparation of Epitaxial Graphene Samples: Large area epitaxial graphene films are grown on the Si face of 6H silicon carbide (0001) substrates (II–VI Inc) by the thermal decomposition method.[14] The first carbon layer on the Si-face of SiC is called the buffer layer and this layer is

partially covalently bonded to the SiC surface (≈30% sp^3 bonded carbon atoms[27]). The layers on top of the buffer layer have carbon atoms in sp^2 configuration. Therefore, when we refer to single layer graphene, it is a structure comprised of a graphene layer and buffer layer. The quasi-free standing bilayer graphene is prepared from single layer epitaxial graphene sample by intercalation in hydrogen atmosphere at an approximate pressure of 1000 mbar with hydrogen flow at 3.0 slph. Hydrogen atoms saturate Si–C bonds between SiC surface and buffer layer, which create Si–H bonds and turn sp^3 bonded carbon atoms into sp^2 configuration. More details about the growth procedure can be found in Reference.[15,16] Schemes of the structures are presented in Figure 1a.

Nanoindentation Measurements: Nanoindentation experiments are performed on Hysitron TI 950 Triboindenter with a diamond Berkovich tip. The typical radius of curvature of a Berkovich tip, $R_{tip,}$ is ≈150 nm at room temperature and in humid atmosphere. The Berkovich tip indents the sample surface at a constant rate until the set maximum load is achieved, then is held for 5 s. The loading time for this process is 62 s. Finally, the tip is unloaded linearly in time within 5 s (see Figure 1c). The used maximal load varied from 300 µN to 10 mN. The sensitivity of measurement is <30 nN and <0.2 nm for load and displacement, respectively.

The unloading part of the load indentation depth curve is analyzed and the hardness H and elastic modulus E can be determined. The hardness H is defined by the following equation

$$\mathrm{H} = \frac{P_{\max}}{A_{\mathrm{p}}} \tag{2}$$

where P_{max} is the maximal applied load and A_p is the projected area of the indenter in sample surface. For the Berkovich tip, the projected area is equal to

$$A_{\mathrm{p}} = 24.5 h_c^2 \tag{3}$$

Here h_c is the contact depth which can be calculated from the maximal indentation depth h_{max}, the maximal applied load P_{max}, the contact stiffness S, and a geometric factor ϵ (for Berkovich tip, $\epsilon = 0.75$) by

$$h_{\mathrm{c}} = h_{\max} - \varepsilon \frac{P_{\max}}{S} \tag{4}$$

At large contact depths the ideal tip area function, mentioned in Equation 3 can yield accurate results, whereas at low contact depths the actual tip geometry must be considered to get accurate results, due to the presence of an indentation size effect. The indentation size effect can be caused by several factors, such as the presence of residual stresses and friction/adhesion between the sample surface and the indenter.[28,29] We therefore use the following equation to describe the projected area

$$A\ (h_c) = C_0\ h_c^2 + C_1 h_c + C_2 h_c^{1/2} + C_3 h_c^{1/4} + C_4 h_c^{1/8} + C_5 h_c^{1/16} \tag{5}$$

The parameters in Equation 5 are obtained through a fitting procedure of the experimental data of the bare SiC (see Figure S5, Supporting Information) with the parameter C_0 kept at 24.56, describing the ideal Berkovich diamond indenter.

Contact stiffness S is defined as $S = dP/dh$, which can be obtained from the unloading part of a load-displacement curve as shown in Figures S2–S4 (Supporting Information). Then the reduced elastic modulus E_r is

$$E_{\mathrm{r}} = \frac{\sqrt{\pi}}{2\beta} \frac{S}{\sqrt{A_{\mathrm{p}}}} \tag{6}$$

where β is a correction factor =1.034 for a Berkovich tip. The reduced elastic modulus is given by

$$\frac{1}{E_{\mathrm{r}}} = \frac{1-\nu^2}{E} + \frac{1-\nu_{\mathrm{i}}^2}{E_{\mathrm{i}}} \tag{7}$$

where E_i= 1140 GPa and ν_i= 0.07 are the known elastic modulus and Poisson's ratio of the indenter, and E and ν are the same parameters of the sample.

AFM Nanoindentation Experiments: The AFM nanoindentation experiments are performed on a Bruker Multimode 8 AFM using a diamond AFM probe (Micro Star Technologies, tip radius ≈10 nm, normal spring constant 152 N m^{-1}) in ambient conditions. The normal forces between 0 and 200 µN are used to indent a sample's surface. The investigated area is scanned before and after indentation experiment with the same tip in a tapping mode, to distinguish if the residual indentation was created or not.

Conductive AFM experiments: The conductive AFM measurements are performed with a Bruker Multimode 8 AFM using a sharp conductive diamond probe (Adama innovation, tip radius ≈10 nm, normal spring constant 74 N m^{-1}) in ambient conditions. The current dependency on normal load is measured at forces between 0 and 250 nN.

Supporting Information

Supporting Information is available from the Wiley Online Library or from the author.

Acknowledgements

This work was supported by the U.S. Department of Energy, Office of Science, Basic Energy Sciences, MSE Division under the Award # DE-SC0018924 and by the U.S. Army Research Office under the Award # W911NF2020116. The authors also acknowledge Prof. Walt de Heer and Dr. Claire Berger for providing some epitaxial graphene samples.

Conflict of Interest

The authors declare no conflict of interest.

Data Availability Statement

The data that support the findings of this study are available in the supplementary material of this article.

Keywords

diamene, epitaxial graphene, SiC, hardness, Young's modulus

Received: August 9, 2022
Revised: December 7, 2022
Published online: January 4, 2023

[1] C. Lee, X. Wei, J. W. Kysar, J. Hone, *Science* **2008**, *321*, 385.
[2] F. Scarpa, S. Adhikari, A. Srikantha Phani, *Nanotechnology* **2009**, *20*, 065709.
[3] B. Zhang, L. Mei, H. Xiao, *Appl. Phys. Lett.* **2012**, *101*, 121915.
[4] A. Zandiatashbar, G. H. Lee, S. J. An, S. Lee, N. Mathew, M. Terrones, T. Hayashi, C. R. Picu, J. Hone, N. Koratkar, *Nat. Commun.* **2014**, *5*, 3186.
[5] J. W. Suk, R. D. Piner, J. An, R. S. Ruoff, *ACS Nano* **2010**, *4*, 6557.
[6] S.-Y. Park, Y.-C. Kim, R. S. Ruoff, J.-Y. Kim, *APL Mater.* **2019**, *7*, 031106.
[7] F. Cellini, F. Lavini, C. Berger, W. de Heer, E. Riedo, *2D Mater.* **2019**, *6*, 035043.

[8] M. Hammad, J. J. Adjizian, C. H. Sacré, B. Huet, J. C. Charlier, J. P. Raskin, T. Pardoen, *Carbon* **2017**, *122*, 446.
[9] Y. Gao, T. Cao, F. Cellini, C. Berger, W. A. de Heer, E. Tosatti, E. Riedo, A. Bongiorno, *Nat. Nanotechnol.* **2018**, *13*, 133.
[10] F. Cellini, F. Lavini, T. Cao, W. De Heer, C. Berger, A. Bongiorno, E. Riedo, *FlatChem* **2018**, *10*, 8.
[11] F. Lavini, M. Rejhon, E. Riedo, *Nat. Rev. Mater.* **2022**, *7*, 814.
[12] F. Cellini, Y. Gao, E. Riedo, *Sci. Rep.* **2019**, *9*, 4075.
[13] M. Kuhn, D. Tierney, M. Simmers, *American Ceramic Society Bulletin* **2017**, *96*, 38.
[14] J. Kunc, M. Rejhon, E. Belas, V. Dedic, P. Moravec, J. Franc, *Phys. Rev. Appl.* **2017**, *8*, 044011.
[15] J. Kunc, M. Rejhon, P. Hlidek, *AIP Adv.* **2018**, *8*, 045015.
[16] M. Rejhon, J. Kunc, *J. Raman Spectrosc.* **2018**, *50*, 465.
[17] W. C. Oliver, G. M. Pharr, *J. Mater. Res.* **2011**, *19*, 3.
[18] P. Chai, S. Li, Y. Li, L. Liang, X. Yin, *Micromachines* **2020**, *11*, 102.
[19] A. Datye, U. Schwarz, H.-T. Lin, *Ceramics* **2018**, *1*, 198.
[20] J. L. Henshall, C. A. Brookes, *J. Mater. Sci. Lett.* **1985**, *4*, 783.
[21] P. T. B. Shaffer, *J. Am. Ceram. Soc.* **1964**, *47*, 466.
[22] B. Jönsson, S. Hogmark, *Thin Solid Films* **1984**, *114*, 257.
[23] V. V. Brazhkin, A. G. Lyapin, R. J. Hemley, *Philos. Mag. A* **2002**, *82*, 231.
[24] H. Kitahara, Y. Noda, F. Yoshida, H. Nakashima, N. Shinohara, H. Abe, *J. Ceram. Soc. Jpn.* **2001**, *109*, 602.
[25] M. Lucas, K. Gall, E. Riedo, *J. Appl. Phys.* **2008**, *104*, 113515.
[26] W. D. Nix, H. Gao, *J. Mech. Phys. Solids* **1998**, *46*, 411.
[27] K. V. Emtsev, F. Speck, T. Seyller, L. Ley, J. D. Riley, *Phys. Rev. B* **2008**, *77*, 155303.
[28] M. Sakai, S. Shimizu, T. Ishikawa, *J. Mater. Res.* **1999**, *14*, 1471.
[29] H. Li, A. Ghosh, Y. H. Han, R. C. Bradt, *J. Mater. Res.* **1993**, *8*, 1028.

ADVANCED ELECTRONIC MATERIALS
Open Access
www.advelectronicmat.de

Effect of Molecular Weight on the Morphology of a Polymer Semiconductor–Thermoplastic Elastomer Blend

Amnahir Peña-Alcántara, Shayla Nikzad, Lukas Michalek, Nathaniel Prine, Yunfei Wang, Huaxin Gong, Elisa Ponte, Sebastian Schneider, Yilei Wu, Samuel E. Root, Mingqian He, Jeffrey B.-H. Tok, Xiaodan Gu, and Zhenan Bao**

Polymer semiconductors (PSCs) are essential active materials in mechanically stretchable electronic devices. However, many exhibit low fracture strain due to their rigid chain conformation and the presence of large crystalline domains. Here, a PSC/elastomer blend, poly[((2,6-bis(thiophen-2-yl)-3,7-bis(9-octylnonadecyl)thieno[3,2-b]thieno[2′,3′:4,5]thieno[2,3-d]thiophene)-5,5′-diyl)(2,5-bis(8-octyloctadecyl)-3,6-di(thiophen-2-yl)pyrrolo[3,4-c]pyrrole-1,4-dione)-5,5′-diyl]] (P2TDPP2TFT4) and polystyrene-*block*-poly(ethylene-ran-butylene)-*block*-polystyrene (SEBS) are systematically investigated. Specifically, the effects of molecular weight of both SEBS and P2TDPP2TFT4 on the resulting blend morphology, mechanical, and electrical properties are explored. In addition to commonly used techniques, atomic force microscopy-based nanomechanical images are used to provide additional insights into the blend film morphology. Opposing trends in SEBS-induced aggregation are observed for the different P2TDPP2TFT4 molecular weights upon increasing the SEBS molecular weight from 87 to 276 kDa. Furthermore, these trends are seen in device performance trends for both molecular weights of P2TDPP2TFT4. SEBS molecular weight also has a substantial influence on the mesoscale phase separation. Strain at fracture increases dramatically upon blending, reaching a maximum value of 640% ± 20% in the blended films measured with film-on-water method. These results highlight the importance of molecular weight for electronic devices. In addition, this study provides valuable insights into appropriate polymer selections for stretchable semiconducting thin films that simultaneously possess excellent mechanical and electrical properties.

1. Introduction

Polymer semiconductors (PSCs) are a promising class of materials for creating flexible and stretchable electronic devices, such as organic field-effect transistors (OFETs),[1–4] organic light-emitting diodes,[5–7] and organic solar cells.[8–10] These PSCs are solution-processable, allowing lightweight, large-area, and low-cost electronic devices to be conformable to various surfaces, such as on the human body.[11,12] However, despite the relatively low crystallinity of high-performance PSCs, their rigid molecular structures limit the intrinsic flexibility and stretchability, which suffer from fracture under strain below 10%.[13,14] To date, several methods have been employed to improve PSC mechanical properties, such as: 1) synthesizing stretchable PSCs with new molecular design concepts,[15–19] 2) blending PSCs with an insulating elastic polymer matrix,[16,20–22] 3) employing structural engineering,[23] such as wrinkles, buckling or porous structures, and 4) incorporating small molecule additives.[24–27]

Blending a PSC with an elastomer is an appealing strategy as it is capable of

A. Peña-Alcántara, E. Ponte
Department of Materials Science and Engineering
Stanford University
Stanford, CA 94305, USA

S. Nikzad, L. Michalek, H. Gong, Y. Wu, S. E. Root, J. B.-H. Tok, Z. Bao
Department of Chemical Engineering
Stanford University
Stanford, CA 94305, USA
E-mail: zbao@stanford.edu

The ORCID identification number(s) for the author(s) of this article can be found under https://doi.org/10.1002/aelm.202201055.

DOI: 10.1002/aelm.202201055

N. Prine, Y. Wang, X. Gu
School of Polymer Science and Engineering
The University of Southern Mississippi
Hattiesburg, MS 3940, USA
E-mail: xiaodan.gu@usm.edu

S. Schneider
Department of Chemistry
Stanford University
USA

M. He
Corning Incorporated
Corning, New York, NY 14831, USA

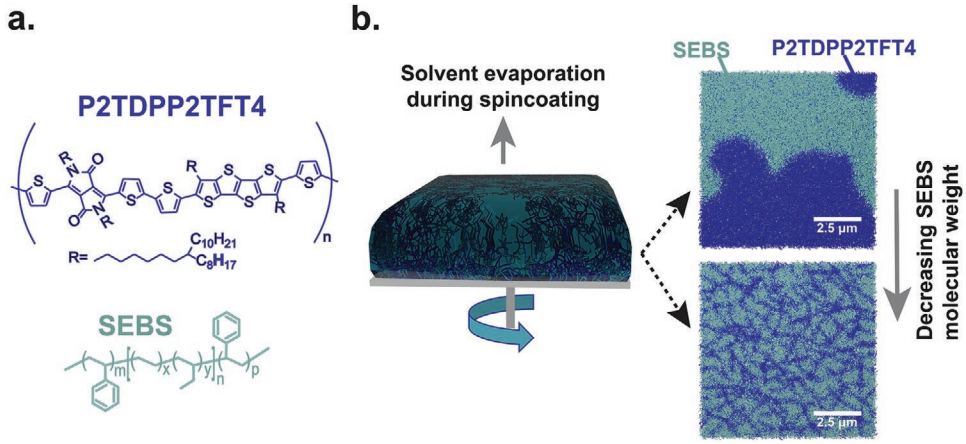

Figure 1. a) Chemical structure of P2TDPP2TFT4 and SEBS. b) Schematic rendering showing solvent evaporation during spin-coating from solution to thin film of the P2TDPP2TFT4/SEBS blends. Two distinctive mesoscale morphologies are represented in a schematic micrograph for the 95k-DPP/82k-SEBS and 95k-DPP/276k-SEBS blends, respectively. P2TDPP2TFT4 is represented by dark blue and SEBS in light blue.

not only improving a film's mechanical properties but also of decreasing the consumption of the costly PSC component and does not require additional synthetic efforts. Moreover, it has been found that with a proper selection of elastic insulating polymer, improved charge transport capabilities of the blend film can be achieved relative to the neat PSC film.[16,20,22] The improved charge-transport property in PSC/elastomer blends has been attributed to optimized film morphologies such as increased PSC backbone planarization and aggregation, more favorable polymer chain alignment along the long axis of nanostructured aggregates, and a well interconnected PSC nanostructure network.[16,20–22] Many previous studies used polystyrene (PS) as the insulating polymer.[28–30] However, recent work showed thermoplastic elastomers can have the added benefits of improving the softness and mechanical robustness of the PSC composite films[20] as PS is typically glassy and has a brittle nature.[31]

Due to the applicability of diketopyrrolopyrrole (DPP)-based PSCs in various fabrication methods,[32,33] we use a DPP-based PSC as our model system, poly[((2,6-bis(thiophen-2-yl)-3,7-bis(9-octylnonadecyl)thieno[3,2-b]thieno[2′,3′:4,5]thieno[2,3-d]thiophene)-5,5′-diyl)(2,5-bis(8-octyloctadecyl)-3,6-di(thiophen-2-yl)pyrrolo[3,4-c]pyrrole-1,4-dione)-5,5′-diyl]] (P2TDPP2TFT4), blended with a thermoplastic elastomer, polystyrene-*block*-poly(ethylene-ran-butylene)-*block*-polystyrene (SEBS). We chose P2TDPP2TFT4 as the PSC because its synthesis has been carefully studied for solution processability and tuning of the molecular weight.[34] DPP-based PSCs are typically semi-crystalline, donor-acceptor type conjugated polymers with a strong tendency for aggregation due to π–π stacking and have been reported to show high charge carrier mobilities in thin film transistor devices.[13,35] Although there has been success in improving electronic and mechanical performance through blending of different elastomers (i.e., polydimethylsiloxane (PDMS) and polyethylene),[16] SEBS was chosen as the insulating elastomer matrix due to its similar surface energy compared to DPP polymers.[20] It was observed previously that DPP-based/ SEBS polymer blends have nanoscale phase-separated morphology of interconnected PSC nanofibrils with reduced conformational defects compared to the neat polymer.[20] A previous study reported that blending another DPP-based PSC, poly-[2,5-bis(7-decylnonadecyl)pyrrolo[3,4-c]pyrrole-1,4-(2 H,5 H)-dione-(E)-(1,2-bis(5-(thiophen-2-yl)selenophen-2-yl)ethene) (DPPDTSE), with SEBS resulted in a 50% higher field effect mobility compared to the neat DPPDTSE.[20] However, a detailed understanding of the effect of SEBS molecular weight is still missing. Specifically, we hypothesize that SEBS molecular weight may affect the phase separation and microstructure of the blended films, and these morphological parameters will affect the resulting thin-film mechanical and charge transport properties.

The polymer blend solution is a ternary system, which experiences phase separation upon spin-coating as the solvent evaporates. In a polymer blend, morphology and phase separation are influenced by various parameters, such as solvent choice,[36] coating conditions,[21,22] polymer concentration,[37] and polymer molecular weight.[22,26,38–40] Phase separation, dominated either by spinodal decomposition or nucleation and growth, occurs due to polymer–polymer immiscibility depending upon the enthalpic and entropic contributions to the free energy of mixing.[16] In addition, substrate surface energy will influence vertical stratification, which has been used to create self-encapsulated films and enables a one-step process in creating the dielectric and active PSC layers.[16]

The effect of PSC molecular weight on the film morphology in P2TDPP2TFT4/SEBS blends with a constant SEBS molecular weight of 125 kDa was previously studied by our group.[22] We found that aggregation-induced molecular ordering in these blend films was strongly correlated to the molecular weight of the semiconducting component. The higher the molecular weight of PSC used to blend with SEBS, the greater the observed ratio of polymer aggregation, resulting in improved charge transport in OFETs.[22] Prompted by this initial preliminary study, in this current work, we systematically investigate the effects of varying SEBS molecular weight in addition to PSC molecular weight, and test their effects on the blend-film morphology, mechanical properties, and OFET performances. Specifically, P2TDPP2TFT4/SEBS blended films (**Figure 1**a,b) with several combinations of molecular weights (**Table 1**) were analyzed using ultraviolet-visible (UV–vis) absorption spectroscopy, grazing incidence X-ray diffraction (GIXD), X-ray photoelectron

Table 1. Molecular weight, dispersity (*Đ*), and styrene content (wt%) of the different polymers.

Polymer	M_n [kDa]	*Đ*	Styrene content [wt%]
95k-DPP	95	2.49	–
48k-DPP	48	1.91	–
276k-SEBS	276	1.17	28
158k-SEBS	158	1.18	32
82k-SEBS	82	1.01	28
18%ps-93k-SEBS	93	1.09	18
42%ps-72k-SEBS	72	1.10	42

spectroscopy (XPS), atomic force microscopy (AFM), AFM-based infrared-spectroscopy (AFM-IR), and optical microscopy (OM). The mechanical properties of the polymer blends were investigated through film-on-water tensile tests and AFM based nanomechanical mapping. The charge transport properties were measured by characterizing the corresponding OFETs. A schematic of the film formation and final morphology for varying molecular weights is shown in Figure 1b. We observed that the molecular weight of SEBS did not significantly affect the solution-phase pre-aggregation of P2TDPP2TFT4 but did cause changes to the amount of P2TDPP2TFT4 aggregation in thin film. AFM images revealed substantial differences in mesoscale morphology, while mechanical tests revealed changes in strain at fracture and modulus for P2TDPP2TFT4 blends depending on the SEBS molecular weight. Last of all, the field-effect mobility trends, as a measure of charge transport in OFETs, should corelate with the aggregation trends based on the molecular weight of SEBS.

2. Results and Discussion

2.1. Morphology

We first investigated the thin film morphology of blends of various P2TDPP2TFT4 and SEBS molecular weights as well as the styrene content in SEBS (Table 1). Chemical structures of P2TDPP2TFT4 and SEBS are shown in Figure 1a. The films were prepared by spin coating a chlorobenzene solution containing P2TDPP2TFT4: SEBS with 3:7 weight ratio (final P2TDPP2TFT4 concentration of 2 mg mL^{-1} in chlorobenzene) on octadecyltrimethoxylsilane (OTS)-modified silicon wafer[41] or optically clean glass substrates. This weight ratio was chosen as it was previously found to be the typical optimal ratio for several PSC/SEBS blends to give both high charge carrier mobilities and good stretchability, given the maximum amount of aggregation and ideal nanofiber structure being present at this ratio.[20–22]

The absorption spectrum measured by UV–vis spectroscopy allows for determination of changes in the aggregation behaviors of the PSC.[42,43] For P2TDPP2TFT4, typically the absorption band from UV–vis exhibits a broad π–π^* transition of the monomer unit at ≈450 nm. The charge transfer absorption band between 600 and 900 nm shows two vibronic peaks, one at higher energy (0–1 transition) and one at lower energy (0–0 transition), which is normally attributed to polymer aggregation.[42,43] A larger (0–0) to (0–1) peak intensity ratio and bathochromic shift is attributed to a higher fraction of aggregated structures. The red shift of the aggregation peak would be related to either planarization or long-range order.[42–44]

As seen from **Figure 2**a, all blended P2TDPP2TFT4/ SEBS solutions used for film deposition exhibited a similar increase in the (0–0):(0–1) ratio as compared to that of the neat solution of P2TDPP2TFT4. However, no significant bathochromic shift was observed in the solution. The changes in (0–0):(0–1) ratio indicates a slight change in the amount of aggregation; however, there is not much of a difference based on the SEBS molecular weight. Consistent with prior reports,[20–22] all our blend films showed an increased (0–0):(0–1) ratio (aggregation ratio) and a bathochromic red shift of the (0–0) transition, ≈8 nm, as compared to the neat film. This increased ratio and bathochromic shift suggest that blending P2TDPP2TFT4 with SEBS led to more aggregation formation, longer range ordered aggregates, and/or backbone planarization.

We observed that the molecular weight of SEBS gave a weak opposing trend for the ratio of (0–0) to (0–1) transition peaks from the absorption profile for the two molecular weights of P2TDPP2TFT4. In the case of 95k-DPP, decreasing the SEBS molecular weight increased the PSC aggregation ratio in blend thin films, which suggested an increase in the amount of aggregation formation (Figure 2b). On the other hand, for the 48k-DPP, decreasing the molecular weight of SEBS resulted in a slight decrease in aggregation ratio (Figure 2b). We hypothesize that the opposing effects of SEBS molecular weight on aggregation are the product of the interplay between the kinetic trapping caused by the fast solidification rates in spin-coating and thermodynamic interactions. Previous studies have indicated that the kinetics of crystallization will influence the final film morphology.[45] In addition, increasing the molecular weight of a polymer delayed the solidification and crystallization rates of film formation.[46,47] The influence of kinetics (solvent evaporation rate, etc.) on the final film have not been studied in detail for this project; however, future studies should further investigate this phenomenon.

The crystalline structure of the thin films was further investigated using GIXD to observe the impact of molecular weight on the polymer crystallinity. As crystalline packing coherence length (L_C) can influence charge transport;[48] here, we estimated L_C using the Scherrer equation (Equation (1)),

$$L_C = \frac{2\pi K}{\Delta_q} \tag{1}$$

where K is a shape factor and Δ_q is the full-width half-maximum of a diffraction peak.[48] A higher L_C is an indication of a longer range order.[49] In this system, L_C of the (200) reflection was observed to increase when P2TDPP2TFT4 was blended with SEBS (**Figure 3**a, **Table 2**; Figure S1, Supporting Information), as previously reported.[22] L_C from the (200) reflection increased by up to 30% from the 95k-DPP neat film to blends, while it increased by up to 60% for the 48k-DPP blends compared to its neat film. The slightly larger increase in (200) L_C for blended 48k-DPP films (≈1.6-fold) as compared to 95k-DPP films (≈1.3-fold) could be caused by the higher tendency for conformational disorder in the higher molecular weight 95k-DPP compared to

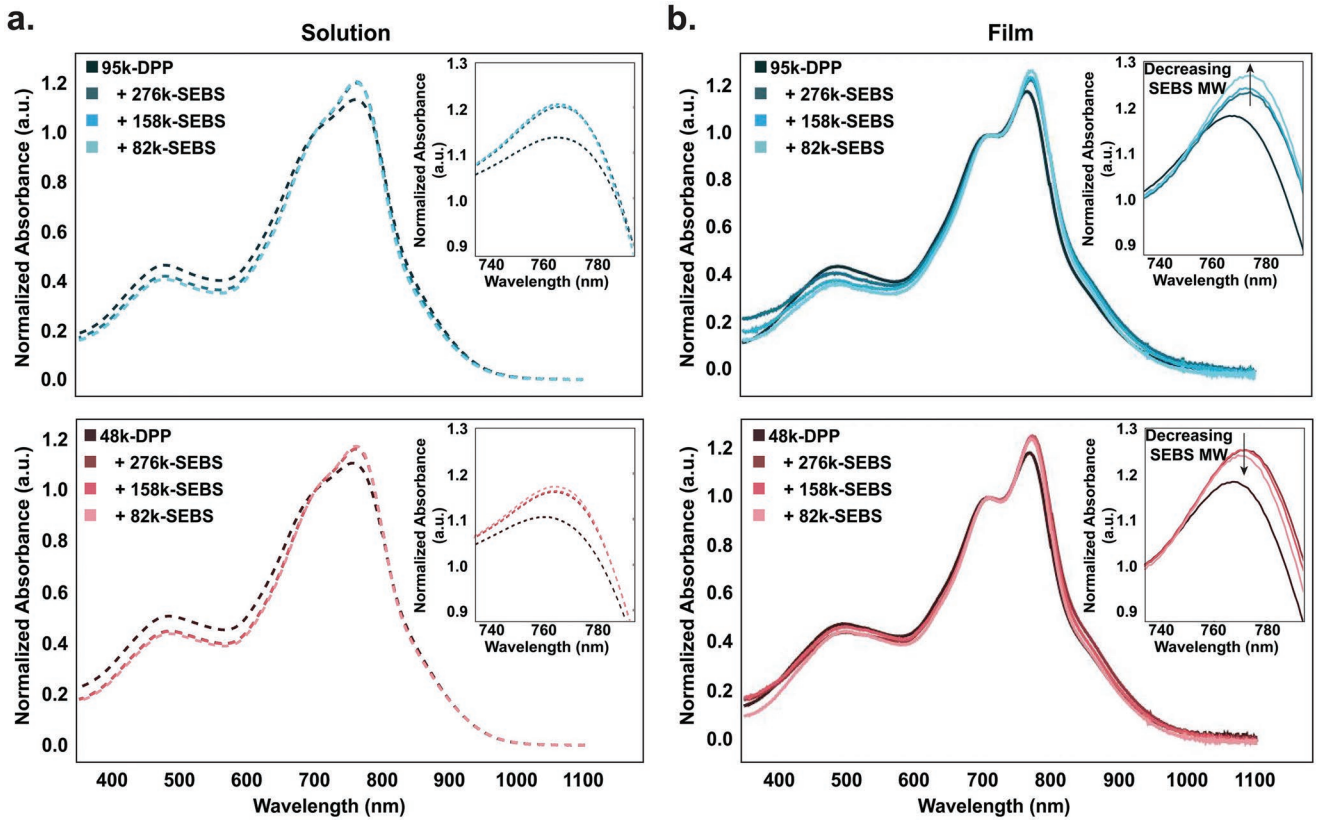

Figure 2. a) Solution UV–vis spectrum of 95k-DPP and 48k-DPP and their blends of variable SEBS molecular weights prepared from solutions with chlorobenzene as the solvent. b) UV–vis spectrum of 95k-DPP and 48k-DPP thin films (chlorobenzene (CB) as the solvent) and their blends of variable SEBS molecular weights annealed at 150 °C for 1 h.

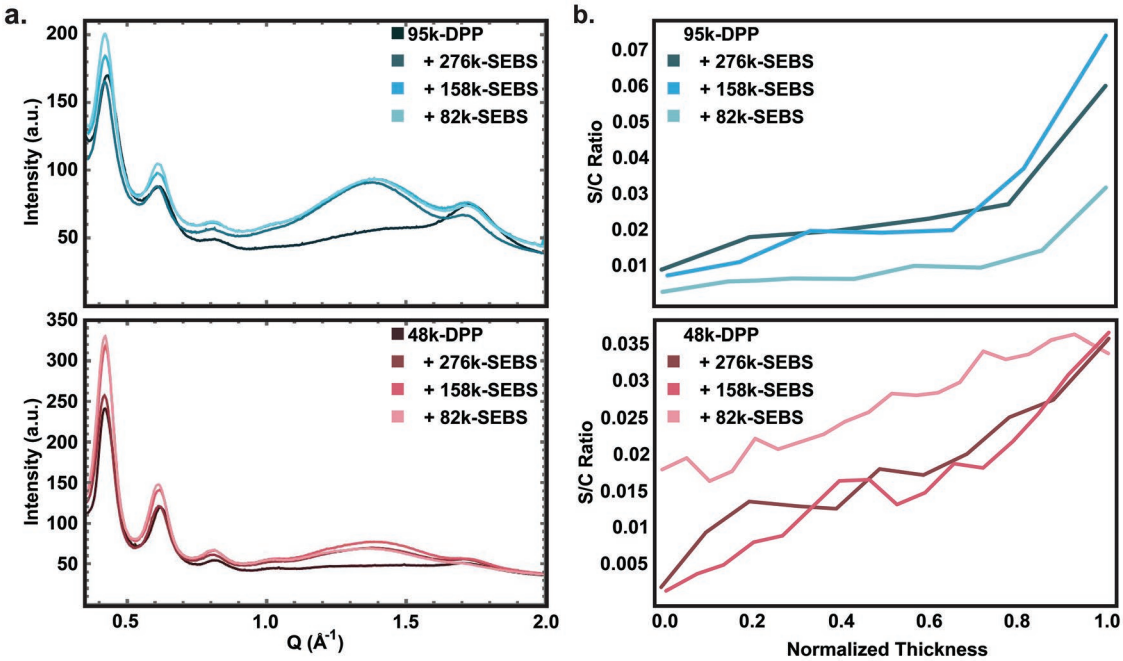

Figure 3. a) 1D GIXD profiles extracted from 2D GIXD patterns for the out-of-plane direction (q_z) of 95k-DPP and 48k-DPP thin film blends of various SEBS molecular weights. b) The ratio of the S 2p to C 1s peak for the 95k-DPP and 48k-DPP polymer blends of different SEBS molecular weights at different depths against their normalized thickness. 1.0 represents the air film interface, while 0 represents the dielectric film interface.

Table 2. Lamellar-spacing, π-stacking distance, and coherence length (L_C) of 95k-DPP and 48k- DPP with their blends with 276k-SEBS, 158k-SEBS, and 82k-SEBS, obtained from GIXD spectrum.

Polymer semiconductor	Elastomer	Lamellar-spacing [Å]	(200) L_C [nm]	π-Stacking [Å]	(010) L_C [nm]
95k-DPP	–	30.2	14.8	3.61	3.27
95k-DPP	276k-SEBS	30.7	19.4	3.63	3.62
95k-DPP	158k-SEBS	30.3	16.3	3.60	4.08
95k-DPP	82k-SEBS	30.6	19.6	3.60	3.37
48k-DPP	–	30.0	16.5	3.68	5.00
48k-DPP	276k-SEBS	30.6	26.1	3.65	5.02
48k-DPP	158k-SEBS	30.4	19.3	3.63	4.46
48k-DPP	82k-SEBS	30.5	22.9	3.66	4.96

the 48k-DPP. On the other hand, the 158k-SEBS gave lower L_c for both molecular weights of P2TDPP2TFT4 compared to the other two SEBS even though this trend was not seen in the UV–vis ratio of the (0–0) and (0–1) transitions. This suggests the blend morphology may be altered by the molecular weight of the SEBS.

The film morphology was further analyzed using a combination of XPS, AFM, AFM-IR, and OM. XPS-based depth profiling was performed to determine the vertical distribution of P2TDPP2TFT4 along the height direction of the blend film. By monitoring the sulfur S(2p) signals (unique to the P2TDPP2TFT4 polymer) and carbon C(1s) signal, we can estimate the Sulphur to Carbon (S/C) ratio; hence, allowing identification as to how P2TDPP2TFT4 was distributed throughout the thickness of the film. Previous SEBS blend studies have found the DPP-based PSC located on both the top and bottom surfaces of the film.[20] However, Tran et al. found that the solubility of a DPP-based PSC impacts the vertical phase separation.[50] Through side-chain engineering, the solubility of the DPP-based PSC is varied. In the case of the more soluble DPP-based PSC, the PSC is concentrated on both the top and bottom surface of the film. On the other hand, with a lower solubility, the DPP-based polymer is found to be concentrated on the top surface.[50] We observed that our blend films have P2TDPP2TFT4 primarily on the air–solid interface (top surface) as opposed to at the semiconductor–dielectric interface (Figure 3b; Figure S2, Supporting Information). There is a gradual change in the concentration of P2TDPP2TFT4 from the air to dielectric interface. The S/C ratio in the thin film at the air interface is 11.8 and 23 times the S/C ratio at the dielectric interface for 95k-DPP and 48k-DPP, respectively (Table S1, Supporting Information). This indicates that the DPP-polymer is concentrated at the top surface of the blend film. This finding is consistent with those published by Tran et al.[50] This is so, given that the molecular weight of P2TDPP2TFT4 (48 and 95 kDa) is large; thus, influencing their solubility and the vertical phase separation.[20]

AFM phase images of both the bottom (**Figure 4**a; Figure S3, Supporting Information) and top (Figure S4, Supporting Information) surfaces of thin films showed island-like structures for P2TDPP2TFT4 when blended with 276k-SEBS that transitioned to uniform nanofibers as SEBS molecular weight decreased to 82k with both 48k-DPP and 95k-DPP. These changes in mesoscale structures can be explained by the changes in miscibility of the polymer blends as well as possibly being influenced by the kinetics of film formation. As molecular weight increases, there is a larger driving force for phase separation due to a smaller entropic gain to the free energy of mixing.[16,40] Indeed, by increasing P2TDPP2TFT4's concentration from 2 to 10 mg mL^{-1} while keeping the weight ratio of P2TDPP2TFT4/SEBS the same (Figure S5, Supporting Information), even in the solution, precipitates were observed in the 95k-DPP/ 276k-SEBS blend, while none were observed in the 95k-DPP/ 82k-SEBS blend. In addition, contact angle measurements (Figure S6 and Table S2, Supporting Information) were conducted to determine the surface energy and estimate the free energy of mixing of the polymer blends. Based on the calculated free energy of mixing (Table S3, Supporting Information), which was dominated by the overall entropy change, increasing the molecular weight of either the P2TDPP2TFT4 or the SEBS increased the driving force for phase separation. The free energy of mixing provides the thermodynamic consideration on the miscibility of the two polymers. However, during film formation, the solution is a ternary system. Future work will be needed on the more complex ternary system.

The SEBS block copolymer microstructure (shown in Figure S7, Supporting Information) also changed in the blended films as its molecular weight varies. SEBS was clearly seen with regularly spaced PS nano-domains surrounding the P2TDPP2TFT4 islands in the 276k-SEBS blends. These PS nano-domains were also visible in the 158k SEBS but became less visible as the SEBS molecular weight decreased to 82k-SEBS. There is a possibility that the SEBS morphology was interrupted due to lower entropic driving force for phase separation with P2TDPP2TFT4 for the lower molecular weight SEBS.

AFM-IR combines AFM with infrared spectroscopy (IR) (FTIR spectra shown in Figure S8, Supporting Information). This experimental tool scans an AFM probe across the sample surface while simultaneously illuminating the area under the probe with a pulsed, tunable infrared laser. When the laser is tuned to the unique infrared absorption bands of the sample, rapid thermal expansion occurs in the material. While in tapping mode, the slight variations in tapping frequency caused by the rapid thermal expansion near the tip are detected as cantilever deflection and can be translated by Fourier transform. Therefore, the technique can distinguish materials in blends by their unique infrared absorption response and map the sample

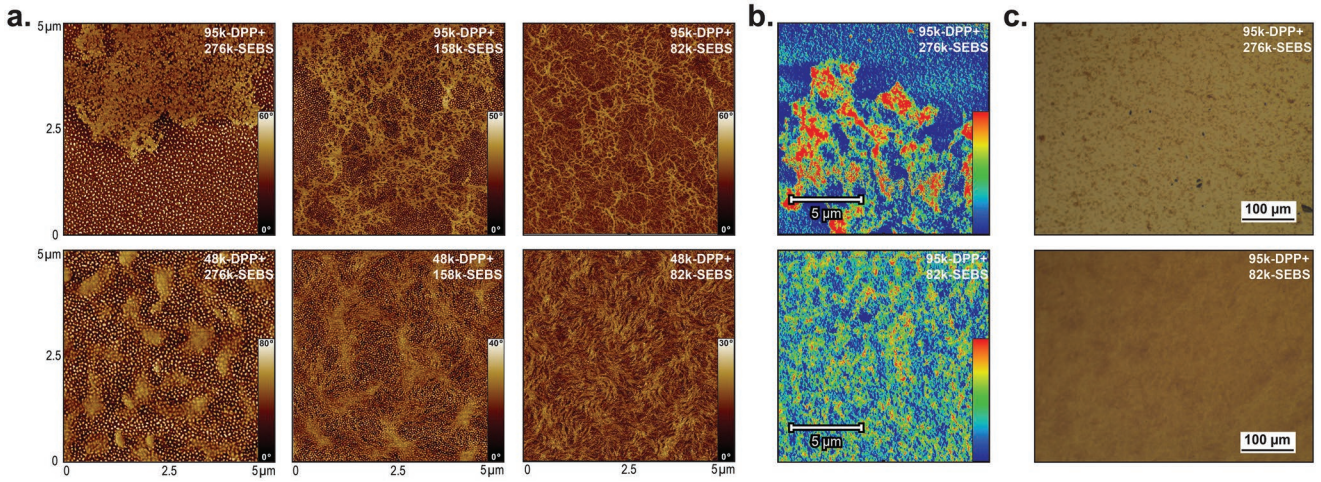

Figure 4. a) Phase AFM images of the bottom surface of 95k-DPP and 48k-DPP polymer blend films with different SEBS molecular weights. b) AFM-IR images of the bottom surface of 95k-DPP blended with 276k-SEBS and 82k-SEBS with an FTIR wavelength of 1659 cm^{-1}. Red regions are those with a larger concentration of DPP while blue regions are those with a lower concentration of DPP. c) OM images of the bottom surface of 95k-DPP blended with 276k-SEBS and 82k-SEBS.

surface as a function of chemical composition.[51] AFM-IR was utilized as a qualitative technique allowing the determination of areas of high concentrations of P2TDPP2TFT4 throughout the film surface. AFM-IR images confirmed that the island-like structures and nanofibers from AFM phase images were regions of higher P2TDPP2TFT4 concentration (Figure 4b; Figures S9 and S10, Supporting Information).

The obtained AFM-IR images further highlighted larger regions of high P2TDPP2TFT4 concentration with increasing P2TDPP2TFT4 and SEBS molecular weights, as seen through the larger clustered green to red regions (5–15 µm in width) of higher concentration of 95k-DPP when blended with 276k-SEBS (Figure 4b; Figure S10, Supporting Information). While in the 95k-DPP and 82k-SEBS blends, there was a more uniform amount of P2TDPP2TFT4 on the surface, seen through the green to red regions. The large islands in 95K-DPP blend films were also visible using OM. Specifically, OM images of 95k-DPP/ 276k-SEBS blended films showed micron-sized domains, which were not present in the smooth films of 95k-DPP/ 82k-SEBS blends (Figure 4c; Figure S11, Supporting Information). We note that despite observing micron-scale P2TDPP2TFT4 enriched domains, our AFM-IR results indicated the presence of a continuous P2TDPP2TFT4 network in 95k-DPP/276k-SEBS films (Figures S7, S9, and S10, Supporting Information).

To investigate whether the observed morphological changes are also dependent on the amounts of PS in SEBS, ≈82 kDa SEBS with different styrene contents was next investigated (Table 1). We observed there was still an increase in the (0–0)/(0–1) ratio and a bathochromic red shift, ≈7 nm, of P2TDPP2TFT4 when blended with this group of various SEBS. However, there was no obvious trend in the (0–0)/(0–1) ratio (Figure S12, Supporting Information), bathochromic shift (Figure S12, Supporting Information), or (200) L_C (Figure S13 and Table S4, Supporting Information) correlated to the styrene content in the SEBS (Figure S12, Supporting Information). AFM phase images (Figures S14 and S15, Supporting Information) and optical images (Figure S16, Supporting Information) were nearly identical regardless of styrene content. Last, P2TDPP2TFT4 was again seen to be primarily concentrated at the air interface rather than the dielectric interface by XPS depth profile (Figure S17, Supporting Information). These results suggest that the molecular weight of SEBS was the dominating factor in impacting P2TDPP2TFT4/SEBS morphology and the PS content in the SEBS played a less significant role. However, we should note that here the effect of styrene content was only studied for ≈82 kDa SEBS. Most SEBS employed in previous studies had a molecular weight of 125 kDa; and thus, the effect of the styrene content at this higher molecular weight may be different.[20–22] We did not use it for our study as there are no commercially available ones with different PS contents for SEBS 125 kDa.

2.2. Mechanical Properties

We next investigated the effect of SEBS molecular weight and the concomitant morphological changes on the film's mechanical properties. The mechanical properties were studied by conducting film-on-water tensile tests and AFM based nanomechanical imaging. Stress–strain curves for the neat and blended films (**Figure 5**a) show large changes in the stress–strain behavior, modulus, and fracture strain. The stress–strain curves of films of the neat P2TDPP2TFT4 (Figure 5a), neat SEBS (Figure S18, Supporting Information), and blends (Figure 5a) show significant differences in stress–strain behavior. Originally, we expected that SEBS would dominate the mechanical properties, given the film composition being majority (70 wt%) SEBS. However, the blend films do not exhibit the pronounced strain stiffening present in neat SEBS (Figure S18, Supporting Information). Thus, the stress–strain behavior is influenced by both the P2TDPP2TFT4 and SEBS. The SEBS has a large influence on the modulus (Figure 5b; Table S5, Supporting Information). The modulus decreases by up to 84% and 75% for 95k-DPP and 48k-DPP, respectively, upon blending. Last of all,

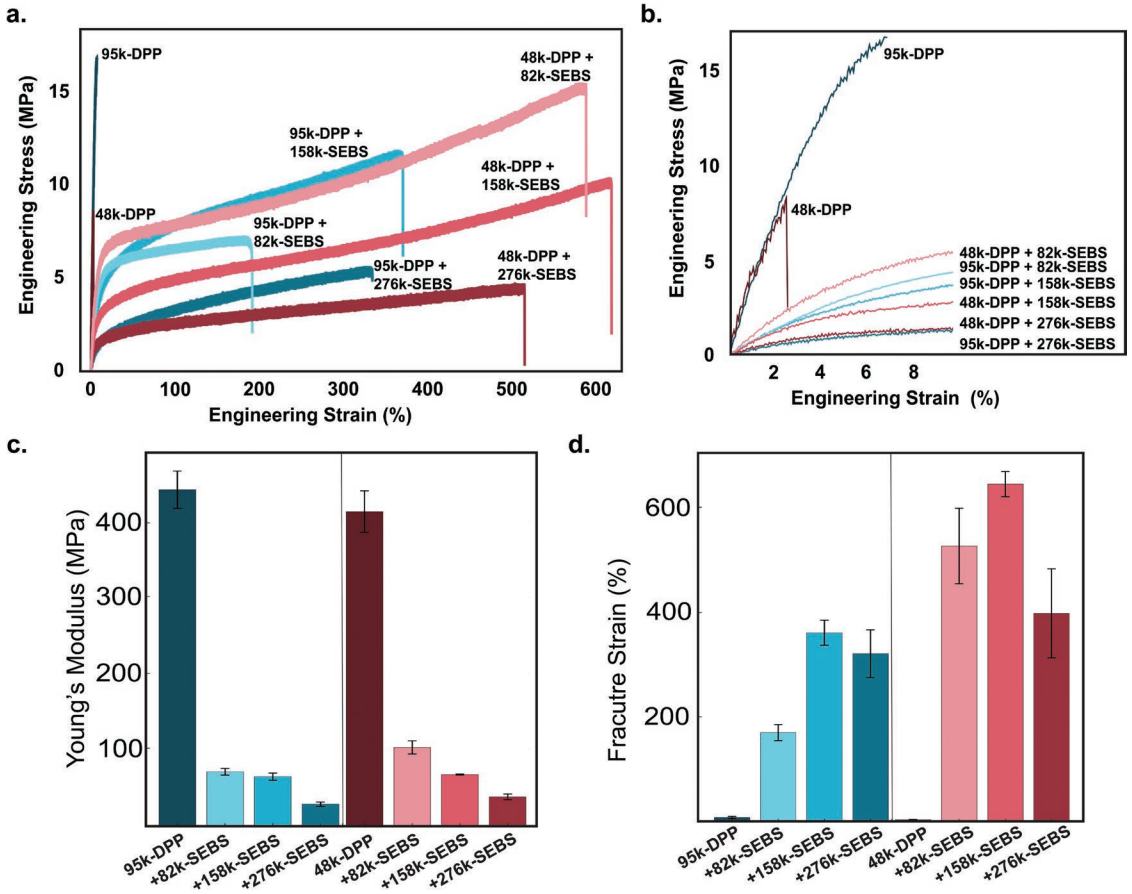

Figure 5. a) Representative stress–strain curves of 95k-DPP and 48k-DPP neat and blended films obtained through film on water tensile tests. b) Zoom in on low strain region of the stress–strain curves of 95k-DPP and 48k-DPP neat and blended films obtained through film on water tensile tests. c) Bar chart showing the Young's modulus of each film. d) Bar chart showing the fracture strain of each film. The error bars represent the standard deviation obtained from three to five different samples.

the fracture strain (Figure 5b; Table S5, Supporting Information) increases by up to 52 and 245 times in the blended films as compared to the neat 95k-DPP and 48k-DPP, respectively.

In terms of the effect of molecular weight, increasing the molecular weight of SEBS decreases the film moduli in both neat SEBS and blend (Table S5, Supporting Information). There are no trends in fracture strain with increasing SEBS molecular weight. However, the fracture strain trends mimic those of the neat SEBS. A complete understanding of the micromechanical failure mechanism and stress–strain behavior is beyond the scope of this paper and should be investigated in future work.

To further investigate the mechanical properties of the blended films, specifically relative to their mesoscale phase separation, AFM based nanomechanical images were collected. For the measurement, a soft cantilever was oscillated through intermittent contact onto the samples surface with a fixed force setpoint to generate force-spectra. With the calibration of the cantilever mechanics and tip radius, the measured force-spectra could be translated into quantitative nanomechanical images, including adhesion, DMT (Derjaguin–Muller–Toporov Model) modulus, deformation (indentation), and dissipation.[52] The nanomechanical property map is in the typical high spatial resolution of an AFM and provides rich information about the blend film, when compared to standard oscillation mode with an amplitude setpoint. In particular, nanomechanical imaging allows for differentiation between properties representing the surface (adhesion and dissipation) and subsurface (modulus and indentation). During the approaching of the cantilever toward the film, if the AFM tip penetrates the sample surface, it would probe the subsurface properties; therefore, providing determination of the DMT modulus and tip indentation depth. However, when the cantilever retracted from the film, the adhesion and dissipation were measured, which were predominantly influenced by the uppermost surface layer.[52]

Nanomechanical images of P2TDPP2TFT4/ SEBS blend films of various P2TDPP2TFT4 molecular weights can be seen in **Figure 6**a (and also in Figures S19 and S20, Supporting Information). The film morphology for all the films is consistent with those imaged in the standard AFM oscillating mode (Figure 4a). However, the modulus and dissipation images provide an increased contrast between P2TDPP2TFT4 and SEBS due to their mechanical differences. Specifically, the P2TDPP2TFT4 regions have a higher modulus (bright green color in modulus map) and lower dissipation (dark blue color in dissipation map) when compared to SEBS regions. Yet, as seen from the oscillating mode AFM images (Figure 4a), the nano-phase

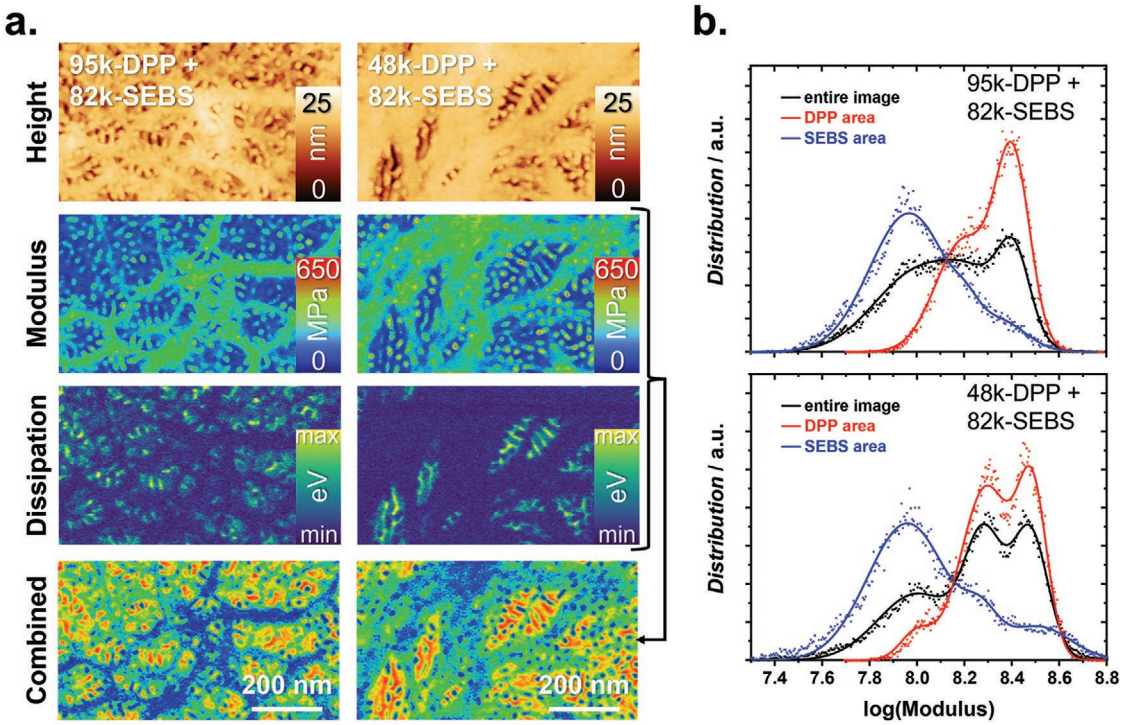

Figure 6. a) Height, DMT modulus, dissipation, and combined (modulus + dissipation) nanomechanical images generated via AFM of the top surface of 95k-DPP/82k-SEBS and 48k-DPP/82k-SEBS. b) Histograms of modulus images (plotted logarithmically) for the entire image (black curves), DPP areas (red curves), and SEBS areas (blue curve).

separation in SEBS can be seen clearly as small dots from the polystyrene domains in Figure 6a (and also in Figures S19 and 20, Supporting Information). In contrast to previous work,[20–22] the SEBS morphology, that is, the dotted features, can even be seen below the P2TDPP2TFT4 regions in the modulus image as it samples the subsurface properties. Specifically, in the 48k-DPP/ 82k-SEBS blend, the SEBS morphology is seen below the P2TDPP2TFT4 fibers in the modulus image but is not visible in the dissipation image. To amplify the difference between the subsurface (modulus) and surface (dissipation) features, the images were arithmetically combined. The resulting images (Figure 6a) displayed contrasting mechanical behaviors for the 95k-DPP/ 82k-SEBS and 48k-DPP/ 82k-SEBS blends. While the 95k-DPP blend showed dark blue fibrous regions, the 48k-DPP blend contained brighter blue and green regions with a visible SEBS morphology. The difference between these two systems indicates that the 95k-DPP/ 82k-SEBS blend consists of relatively thicker P2TDPP2TFT4 fibers on the surface, when compared to the 48k-DPP blend, because no subsurface features of the SEBS morphology could be observed below the fibers of 95k-DPP. To further validate this hypothesis, histograms for the P2TDPP2TFT4 regions, SEBS regions, and the complete image of the modulus images were generated (Figure 6b; Figure S19, Supporting Information). The plotted data for the P2TDPP2TFT4 region (red curves) also indicates a larger contribution of the underlying SEBS morphology (blue curve) for the 48k-DPP blend, which can be explained by a lower thickness of the 48k-DPP fibers on surface when compared to 95k-DPP blends.

Through a similar analysis of the visibility of the SEBS morphology beneath the P2TDPP2TFT4 domains, trends in the relative thickness of PT2DPP2TFT4 regions on the surface of the blended films are also present with variable SEBS molecular weight. In the 95k-DPP blends, as the SEBS molecular weight increases, the surface P2TDPP2TFT4 regions become thinner (Figure 6a; Figure S19a–c, Supporting Information). However, in the 48k-DPP blends, surface P2TDPP2TFT4 regions becomes relatively thicker with increasing SEBS molecular weight (Figure 6a; Figure S19d–f, Supporting Information). A continuous percolation pathway of the PSC is necessary for charge transport. As such, the relative thickness of the P2TDPP2TFT4 regions on the surface (for top contact/bottom gate [TCBG] OFETs) and the connections between these regions will ultimately impact the final device performance. From these experimental results, we hypothesize the relatively thicker top-surface P2TDPP2TFT4 regions will have increased connections with P2TDPP2TFT4 regions deeper within the film; and thus, better device performance.

2.3. FET Characteristics

OFETs were next fabricated to investigate the effect of the characterized morphologies discussed above on the field effect mobility. Both bottom contact/bottom gate (BCBG) (Figure S21, Supporting Information) and TCBG (**Figure 7**) OFET devices were fabricated to account for the possibilities of having vertical gradients of the semiconductor in the film.[53] All output curves are shown in Figure S22, Supporting Information. When compared to previous studies on neat P2TDPP2TFT4 with TCBG devices, our devices had similar mobilities (Figure 7b,c).

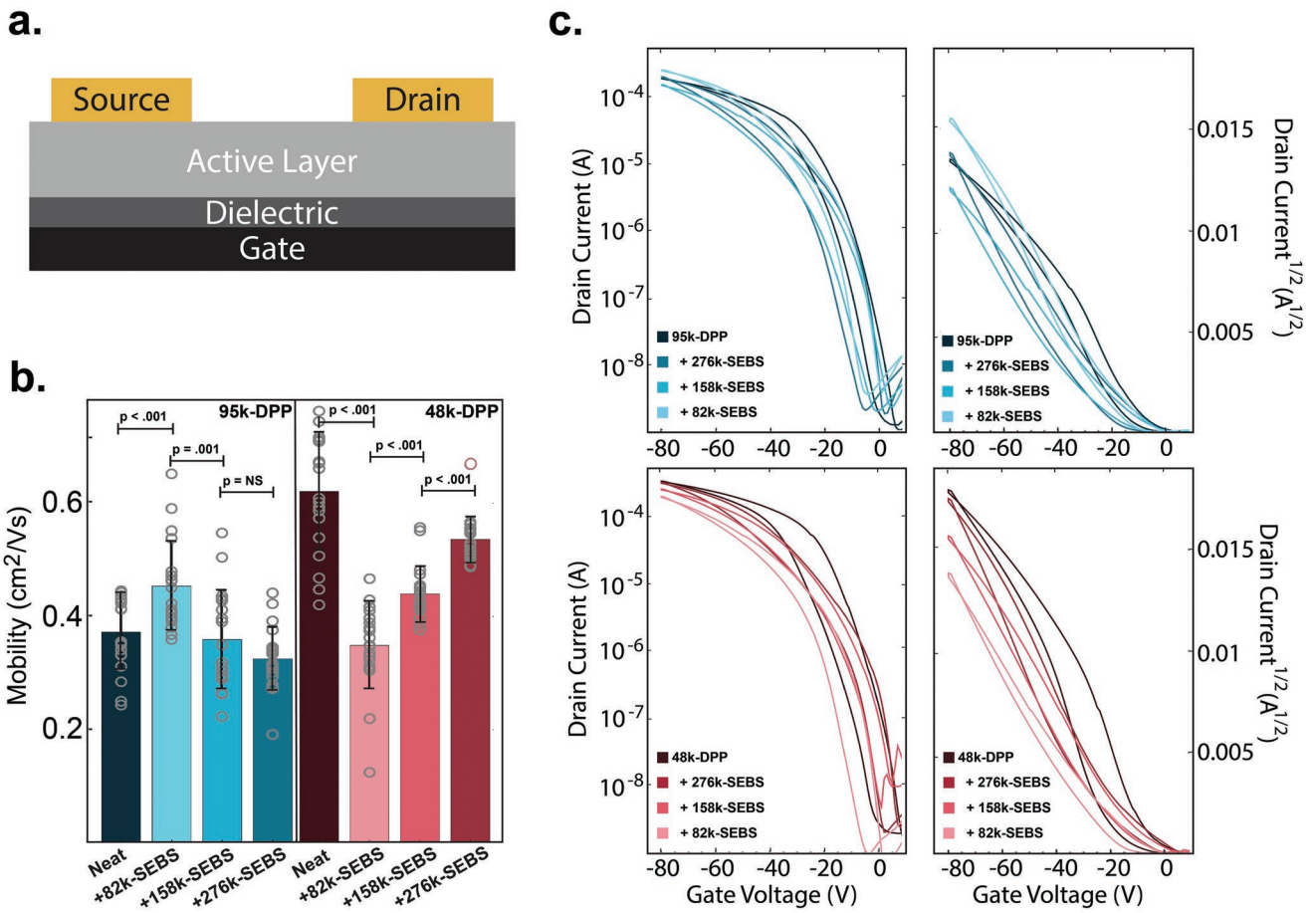

Figure 7. a) Diagram of the top contact/bottom gate OFET. b) Average saturation hole mobility values extracted from OFET. The mobility values obtained for each film are represented by circles. c) Transfer curves of sample OFET for 95k-DPP and 48k-DPP neat and blended films with SEBS of different molecular weights. For each field effect mobility reported, a total of 20 channels on four separate wafers were measured. The source-to-drain voltage was set to −60 V.

Specifically, the previously reported mobility values of 97 kDa P2TDPP2TFT4, extracted from the entire gate voltage regime, were ≈0.35 cm^2 Vs^{-1}, which was comparable to our obtained value of 0.37 cm^2 Vs^{-1}.[34] A mobility value of ≈0.76 cm^2 Vs^{-1} was shown for ≈50 kDa P2TDPP2TFT4, a value close to our 0.62 cm^2 Vs^{-1} for 48 kDa.

Devices fabricated in the BCBG configuration had lower mobilities for both neat and blend films than the corresponding TCBG devices. However, the BCBG devices still showed almost a threefold increase in mobility for blend films as compared to their neat counterpart (Figure S21 and Tables S6 and S7, Supporting Information), indicating there was still an improvement in charge transport in the blend films compared to the neat P2TDPP2TFT4 films, consistent with other previous reports.[20–22] However, given the higher concentration of P2TDPP2TFT4 on the top surface from earlier characterization results, we focused our analysis on TCBG devices. In addition, TCBG devices typically benefit from improved charge injection due to a larger contact area from the source and drain electrodes as compared to the BCBG devices.[54]

In the TCBG devices, only the 95k-DPP/82k-SEBS blended film shows improved charge carrier mobilities as compared to its neat P2TDPP2TFT4 counterpart (Figure 7b,c and **Table 3**). The blend film has a mobility 25% larger than the neat 95k-DPP. All the other blends have comparable or lower mobilities than their neat counterpart (up to 1.74 times lower for the blended film compared to neat). Previous literature reported that blending with a different type of SEBS (125 kDa SEBS with 12 wt PS) resulted in an increase in charge carrier mobility in BCBG device structures, similar to our observed trend.[20,22]

Table 3. Average mobility (μ), on/off current ratio, and threshold voltage of 95k-DPP and 48k-DPP with their blends with 276k-SEBS, 158k-SEBS, and 82k-SEBS, obtained from TCBG devices.

Polymer Semiconductor	Elastomer	μ [cm^2 Vs^{-1}]	On/off current ratio	Threshold voltage [V]
95k-DPP	–	0.37 ± 0.06	10^5	−0.048 ± 5
95k-DPP	276k-SEBS	0.32 ± 0.06	10^4	−1.4 ± 5
95k-DPP	158k-SEBS	0.36 ± 0.09	10^4	0.63 ± 6
95k-DPP	82k-SEBS	0.45 ± 0.08	10^4	0.77 ± 5
48k-DPP	–	0.62 ± 0.1	10^5	−0.44 ± 7
48k-DPP	276k-SEBS	0.54 ± 0.04	10^5	−2.6 ± 5
48k-DPP	158k-SEBS	0.44 ± 0.05	10^5	−3.3 ± 5
48k-DPP	82k-SEBS	0.35 ± 0.08	10^4	−4.5 ± 4

We hypothesized that the lack of improved charge transport in TCBG devices can be explained by the vertical phase separation in the blended films (Figure 3b). Due to the staggered structure of TCBG devices, the charge injection occurs at the top surface (air interface) with the channel still present at the bottom surface (dielectric interface); thus, the charge must travel through the entire film thickness.[54] As such, the vertical phase separation will ultimately affect charge transport throughout the depth of the film. The AFM based nanomechanical imaging results (Figure 7c,d) highlight the difference in thickness and connectivity of the P2TDPP2TFT4 islands/fibers on the surface, which could affect the charge injection and mobility through TCBG devices. The difference in P2TDPP2TFT4 island/fiber thickness is consistent with the 95k-DPP/ 82k-SEBS blends having larger mobility values than the 48k-DPP/ 82k-SEBS blends, given the thin formation and worse continuity of 48k-DPP fibers on the top surface as opposed to the thicker 95k-DPP fibers, suggesting the differences in SEBS impact the device performance. A schematic of the charge transport is shown in **Figure 8**a,b, highlighting the influence vertical phase separation has on the device performance.

Moreover, the mobility trends mimic the trends in the ratio of the (0–0) and (0–1) transition seen by UV–vis, suggesting the small changes in P2TDPP2TFT4 aggregation affected by the addition of various SEBS molecular weights sensitively impact the thin film charge transport. Although the field effect mobility change is small, almost all (except for the difference between 95k-DPP/158k-SEBS and 95k-DPP/276k-SEBS blends) of the trends are statistically significant with a *p*-value less than 0.01. In addition, given the importance in the film formation conditions on final thin film morphology, future work should focus on understanding the kinetics of solvent evaporation and film solidification during film formation.

Last, devices were fabricated from blends with SEBS of various styrene content while keeping the molecular weight of the SEBS comparable. In TCBG devices, it was observed that films with decreasing styrene content had increased mobilities regardless of P2TDPP2TFT4 molecular weight (Figures S23 and S24 and Table S8, Supporting Information), with the highest mobility obtained with 18 wt% styrene content. Even though the origin of this trend is not clearly understood, this observation is consistent with previous literatures that have typically used SEBS with a styrene content of 12 wt% and observed improved charge transport capabilities within blended films of different styrene contents.[20–22]

3. Conclusion

A detailed and systematic study on the effects of polymer molecular weight on the morphology, mechanical behavior, and transistor performance of P2TDPP2TFT4/ SEBS blends was conducted. The influence of SEBS and P2TDPP2TFT4 molecular weight on the final film morphology, mechanical properties, and electronic properties can be summarized as follows: 1) Through UV–vis spectroscopy, we observed that the aggregation and planarization of the higher-MW P2TDPP2TFT4 (95k-DPP) slightly decreased upon increasing the SEBS molecular weight (from 82 to 158 and 276 kDa), while an oppositing trend was observed for the lower molecular weight P2TDPP2TFT4 (48k-DPP). 2) AFM and AFM-IR images showed that both high and low molecular-weight P2TDPP2TFT4 formed fibrillar networks in blends with the low-MW SEBS (82 kDa) blend. Both types of P2TDPP2TFT4 exhibited larger island-like domains with the high-MW SEBS (295 kDa). This is due to a larger driving force for phase separation for the higher molecular weight SEBS associated to less entropic gain in the free energy of mixing. 3) The modulus decreased and fracture strain increased upon blending. Compared to the corresponding neat P2TDPP2TFT4 polymer, our blended films reached a fracture strain greater than 600%. 4) The AFM based nanomechanical imaging determined relative surface thickness of the P2TDPP2TFT4 fibers or islands in 95k-DPP versus 48k-DPP blends had opposing trends with increasing SEBS molecular weight. 95k-DPP blends had increasing thickness as SEBS molecular weight decreased, while the opposite was true for 48k-DPP blends. 5) Despite differences in large-scale phase separation, we also observed that device performances matched well with their corresponding aggregation trends. Previous work studied the molecular weight of the DPP-based polymer and found a large influence on final film morphology and device performance. Our results here add information on the effect of the molecular weight of the elastomers on the final blend film morphology and properties. This work shows that molecular weight and composition of the elastomer can be utilized to finely control and optimize the mechanical and

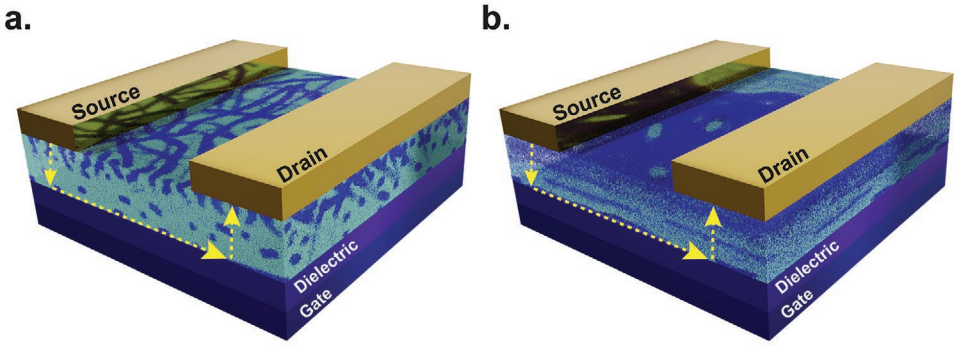

Figure 8. Schematic of the TCBG devices fabricated with a) 82k-SEBS and b) 276k-SEBS. P2TDPP2TFT4 is represented by dark blue and SEBS in light blue. The charge transport pathway is shown through the yellow dashed arrows.

electrical properties of PSC/insulating-polymer blends. These understandings will aid in further improving PSC/elastomer blends for flexible and wearable electronics. Based on the results in this study, future work is still needed on understanding the kinetic process of film formation on PSC/elastomer blends.

4. Experimental Section

Materials: P2TDPP2TFT4 was provided from Corning, Inc. The synthesis for these polymers was reported by Niu et. al.[34] SEBS of variable molecular weights and styrene content (G1633: 276 kDa, G1654: 158 kDa, 1652: 82k Da) and a styrene content 30 wt% were purchased from Kraton, Inc. SEBS of variable styrene content was purchased from Asahi Kasei (Tuftec H1062: 18 wt% St, H1051: 42 wt% St). Gel permeation chromatography of all of the polymers is shown in Figures S25–S30, Supporting Information.

Thin Film Preparation: P2TDPP2TFT4 solution was prepared by dissolving 3 mg in 1 mL of CB, which was heated overnight at 100 °C. Previous studies focused on blended solutions with a final P2TDPP2TFT4 concentration of 3 mg mL^{-1} in CB.[20–22] However, because the 95k-DPP formed precipitates when blended with the 276k-SEBS at the previously used concentration (Figure S1, Supporting Information), in this study, a lower concentration was used. In addition, the SEBS used for this study had a higher styrene content (≈30 wt%) than those previously studied (≈12 wt%)[20–22] because commercially available SEBS of different molecular weights were available only with a higher styrene content. 14.1 mg mL^{-1} solutions of SEBS were created in CB at room temperature and then filtered through a 0.2 µm PTFE filter. Blended solutions were created by mixing 0.66 mL of P2TDPP2TFT4 solution with 0.33 mL of SEBS solution to create 2 mg mL^{-1} DPP solutions with 3:7 weight ratio of P2TDPP2TFT4 : SEBS. Neat and blended solutions were then spin-cast onto OTS-modified[41] silicon wafer (1.5 cm × 1.5 cm). Spin coating was conducted in an N_2-filled glovebox at 1000 rpm for 1 min. The film samples were then annealed at 150 °C for 1 h and slowly cooled to room temperature.

Morphology Characterization: UV–vis spectroscopy was conducted on thin films spin-cast on glass slides using an Agilent Cary 6000i UV/vis/NIR spectrometer. X-ray diffractograms (GIXD) were collected from thin films spin-cast on OTS modified Si wafers at beamline 11-3 in the Stanford Synchrotron Radiation Light Source (SSRL) with a beam energy of 12.7 keV. All the measurements were collected in a helium-purged environment with an X-ray incident angle of 0.12°. AFM images were collected in tapping mode from the Veeco Multimode with a drive frequency of ≈300 kHz and a Tap300Al tip from BudgetSensors (Bulgaria). The bottom sample was measured by using a PDMS stamp to transfer the film. Optical imaging was collected from a Leica DM4000 M light-emitting diode microscope. XPS spectrum was collected from samples spincast on OTS-modified Si wafer using a PHI VersaProbe 3. XPS depth profile was achieved by gas cluster ion beam (GCIB) sputtering with a power of 5 kV 20 nA. Spin cast films were measured using a nanoIR3 AFM-IR from Bruker Instruments (USA) coupled to a MIRcat-QT quantum cascade, mid-infrared laser (frequency range of 917–1700 cm^{-1} and 1900–2230 cm^{-1} using a range of pulse frequencies between 355 and 1382 kHz). AFM-IR data were collected in tapping mode using a gold-coated AFM probe (spring constant [k]: 40 N m^{-1} and resonant frequency [f_o]: 300 kHz) sourced from Bruker. The pulsed mid-IR laser was tuned to frequencies unique to each component as determined by FTIR characterization. Acquired images were flattened using Analysis Studio software.

Mechanical Properties Characterization: For film-on-water tensile tests, Si wafers were initially spincoated with a water soluble poly(sodium 4-styrenesulfonate) (PSS) layer. After that, the neat and blended films were spuncast onto the PSS layer at 1000 rpm for 1 min before being annealed at 150 °C for 1 h and slowly cooled to room temperature. The thickness of the films was measured with an interferometer (Filmetrics Inc. UVX). A oxygen plasma etcher (Diener electronics Inc.) was used to etch the films into a dog-bone shape, and they were then dipped in a water bath to float the dog-bone shaped neat or blended film. The films were then bonded to two aluminum tensile grips coated with a thin layer of PDMS. A high-resolution load cell (KYOWA Inc.) then monitored the force exerted on the film while various strains were applied through a motorized linear stage with a digital encoder (Micronix Inc.). Stress–strain curves were calculated from the force-displacement curves. The stress is equivalent to the force divided by the cross-section area of the dog-bone shaped thin film. The strain is calculated by the displacement in the sample length divided by the original length of the film. Free-standing tensile tests were conducted on Instron 5565.

Nanomechanical imaging was performed on a Bruker Dimension Icon atomic force microscope. NSC19/Al-BS cantilevers were calibrated and used for the measurements. The cantilevers (Estonia) have a nominal resonant frequency of 60 kHz, force constant of 0.5 N m^{-1} and tip radius of 8 nm. The force constant was calibrated by thermal tuning (k = 1.09 N m^{-1}). The deflection sensitivity and tip radius were calibrated on sapphire and Ti reference samples, resulting in a tip radius of 4.1 nm (Bruker-Nanoscope Software – Tip qualification). Force modulation measurements were conducted at a setpoint of 600 pN, peak force frequency of 2 kHz, and an amplitude of 150 nm. The scan resolution and scan rate were set to 256 × 256 pixels and 0.7 Hz. The data were analyzed and depicted with Gwyddion SPM software. The histograms were generated in Gwyddion with a 1D statistical function of masked images.

Contact angle images were taken with a Prosilica GC camera and analyzed using a First Ten Angstroms (FTA32) goniometer. Surface energy was calculated using the Owens–Wendt method:[55]

$$\gamma_s = \gamma_s^p + \gamma_s^d \tag{2}$$

$$(1+\cos\theta_l)\,\gamma_l = 2\left(\sqrt{\gamma_l^d\gamma_s^d} + \sqrt{\gamma_l^p\gamma_s^p}\right) \tag{3}$$

γ_s, γ_s^d, and γ_s^p are the total surface energy, dispersive, and polar component of surface energy of the film, respectively. γ_l, γ_l^d, and γ_l^p are the total surface energy, dispersive, and polar component of surface energy of the test liquid, respectively. For the test liquids used, γ_{water} = 72.8 mJ m^{-2}, γ_{water}^d = 21.8 mJ m^{-2}, γ_{water}^p = 51 mJ m^{-2}, $\gamma_{diiodomethane}$ = 50.8 mJ m^{-2}, $\gamma_{diiodomethane}^d$= 50.8 mJ m^{-2}, and $\gamma_{diiodomethane}^p$ = 0 mJ m^{-2}. The solubility parameter was calculated from:

$$\delta = K\sqrt{\gamma_s} \tag{4}$$

where K is the proportionality constant (K = 116 × 10^3 m$^{-1/2}$).[56] The Flory–Huggins interaction parameter (χ) was estimated with the following equation:[56,57]

$$\chi_{ij} = \frac{V_0}{RT}\left(\delta_i - \delta_j\right)^2 \tag{5}$$

where χ_{ij} is the Flory–Huggins interaction parameter between polymers i and j, V_0 is the geometric mean of the polymer segment molar volume, R is the gas constant, T is the temperature, and δ is the solubility parameter for each polymer. To calculate V_0, the density of P2TDPP2TFT4 was estimated to be 1.05 g cm^{-3}, assuming a similar density to other DPP polymers.[47] The free energy of mixing (ΔG_m) was calculated from the following equation:[58]

$$\Phi G_m = RT\left(\frac{\Phi_i}{N_i}\ln\Phi_i + \frac{1-\Phi_i}{N_j}\ln(1-\Phi_i) + \chi_{ij}\Phi_i(1-\Phi_i)\right) \tag{6}$$

where Φ is the volume fraction and N is the degree of polymerization.

OFET Fabrication and Characterization: For bottom contact/bottom gate devices, Cr/Au (3 nm/40 nm thicknesses) electrodes (width: 4000 µm, length: 200 µm) were evaporated onto the OTS modified SiO_2 wafers. To decrease the contact resistance between the electrodes and the active layer, the electrodes were modified with pentafluorothiophenol.[59] The active layer was then spin-cast onto the electrodes with specifications listed in thin film preparation. For top contact/bottom gate devices, the active layer was spincast on OTS

modified SiO_2 wafers with specifications listed in thin film preparations. MoO_x/Au (3 nm/40 nm thicknesses) electrodes (width: 1000 µm, length: 50 µm) were directly evaporated onto the active layer. OFET transfer and output curves were taken in an N_2-filled glovebox with a Keithley 4200-SCS. Mobility values are average values taken from 8–12 devices. Sample slopes used for the calculation of mobility from the transfer curves are shown in Figure S31, Supporting Information. The source-to-drain voltage was −60 V for all devices. Saturation mobility values (μ) were calculated with the following equation:

$$\mu = \frac{2L}{WC}\frac{\delta\sqrt{I_D}}{\delta V_G} \quad (7)$$

L is the channel length (50 µm), W is the channel width (1000 µm), and C is the gate-channel capacitance per unit area (300 nm SiO_2 dielectric layer) (10.9 nF cm^{-2}). P-values for the field-effect mobilities were calculated using a Student's t-test.

Supporting Information

Supporting Information is available from the Wiley Online Library or from the author.

Acknowledgements

A.P.A. acknowledges support from the National Science Foundation Graduate Research Fellowship Program under Grant No. DGE-1656518 as well as the Stanford Knight–Hennessy Scholarship and the Stanford Enhancing Diversity in Graduate Education Doctoral Fellowship. N.P. and X.G. are thankful for the financial support from NSF (DMR-2047689) for enabling the morphology characterization of stretchable films. L.M. gratefully acknowledges funding through the Walter Benjamin Fellowship Program by the Deutsche Forschungsgemeinschaft (DFG 456522816). The GIXD measurements were made at beamlines 11-3 of the Stanford Synchrotron Radiation Light Source, which are supported by the Director, Office of Science, Office of Basic Energy Sciences, of the US Department of Energy (DE-AC02-76SF00515). Part of this work was performed at the Stanford Nano Shared Facilities (SNSF), supported by the National Science Foundation under award ECCS-2026822. Any opinion, findings, and conclusions or recommendations expressed in this material are those of the authors(s) and do not necessarily reflect the views of the National Science Foundation. This work is supported by US Department of Energy, Office Basic Energy Sciences, Division of Material Science and Engineering, Program on Physical Behaviors of Materials (DE-SC0016523).

Conflict of Interest

The authors declare no conflict of interest.

Data Availability Statement

The data that support the findings of this study are available from the corresponding author upon reasonable request.

Keywords

elastomer, organic field effect transistors, polymer blend, polymer semiconductors

Received: September 29, 2022
Revised: November 19, 2022
Published online:

[1] A. A. Virkar, S. Mannsfeld, Z. Bao, N. Stingelin, *Adv. Mater.* **2010**, *22*, 3857.
[2] M. Chang, G. T. Lim, B. Park, E. Reichmanis, *Polymers* **2017**, *9*, 212.
[3] J. C. Yang, J. Mun, S. Y. Kwon, S. Park, Z. Bao, S. Park, *Adv. Mater.* **2019**, *31*, 1904765.
[4] A. C. Arias, J. D. MacKenzie, I. McCulloch, J. Rivnay, A. Salleo, *Chem. Rev.* **2010**, *110*, 3.
[5] H. Yin, Y. Zhu, K. Youssef, Z. Yu, Q. Pei, *Adv. Mater.* **2022**, *34*, 2106184.
[6] A. Salehi, X. Fu, D.-H. Shin, F. So, *Adv. Funct. Mater.* **2019**, *29*, 1808803.
[7] N. Sun, C. Jiang, Q. Li, D. Tan, S. Bi, J. Song, *J. Mater. Sci.: Mater. Electron.* **2020**, *31*, 20688.
[8] H. Yin, C. Yan, H. Hu, J. K. W. Ho, X. Zhan, G. Li, S. K. So, *Mater. Sci. Eng., R* **2020**, *140*, 100542.
[9] R. Xue, J. Zhang, Y. Li, Y. Li, *Small* **2018**, *14*, 1801793.
[10] G. Wang, F. S. Melkonyan, A. Facchetti, T. J. Marks, *Angew. Chem., Int. Ed.* **2019**, *58*, 4129.
[11] S. Lai, A. Zucca, P. Cosseddu, F. Greco, V. Mattoli, A. Bonfiglio, *Org. Electron.* **2017**, *46*, 60.
[12] S. Wang, J. Xu, W. Wang, G.-J. N. Wang, R. Rastak, F. Molina-Lopez, J. W. Chung, S. Niu, V. R. Feig, J. Lopez, T. Lei, S.-K. Kwon, Y. Kim, A. M. Foudeh, A. Ehrlich, A. Gasperini, Y. Yun, B. Murmann, J. B.-H. Tok, Z. Bao, *Nature* **2018**, *555*, 83.
[13] C. B. Nielsen, M. Turbiez, I. McCulloch, *Adv. Mater.* **2013**, *25*, 1859.
[14] Y. Zheng, S. Zhang, J. B.-H. Tok, Z. Bao, *J. Am. Chem. Soc.* **2022**, *144*, 4699.
[15] G.-J. N. Wang, L. Shaw, J. Xu, T. Kurosawa, B. C. Schroeder, J. Y. Oh, S. J. Benight, Z. Bao, *Adv. Funct. Mater.* **2016**, *26*, 7254.
[16] B. Kang, F. Ge, L. Qiu, K. Cho, *Adv. Electron. Mater.* **2017**, *3*, 1600240.
[17] J. Mun, Y. Ochiai, W. Wang, Y. Zheng, Y.-Q. Zheng, H.-C. Wu, N. Matsuhisa, T. Higashihara, J. B.-H. Tok, Y. Yun, Z. Bao, *Nat. Commun.* **2021**, *12*, 3572.
[18] D. Liu, J. Mun, G. Chen, N. J. Schuster, W. Wang, Y. Zheng, S. Nikzad, J.-C. Lai, Y. Wu, D. Zhong, Y. Lin, Y. Lei, Y. Chen, S. Gam, J. W. Chung, Y. Yun, J. B.-H. Tok, Z. Bao, *J. Am. Chem. Soc.* **2021**, *143*, 11679.
[19] J. Y. Oh, S. Rondeau-Gagné, Y.-C. Chiu, A. Chortos, F. Lissel, G.-J. N. Wang, B. C. Schroeder, T. Kurosawa, J. Lopez, T. Katsumata, J. Xu, C. Zhu, X. Gu, W.-G. Bae, Y. Kim, L. Jin, J. W. Chung, J. B.-H. Tok, Z. Bao, *Nature* **2016**, *539*, 411.
[20] J. Xu, S. Wang, G.-J. N. Wang, C. Zhu, S. Luo, L. Jin, X. Gu, S. Chen, V. R. Feig, J. W. F. To, S. Rondeau-Gagn´e, J. Park, B. C. Schroeder, C. Lu, J. Y. Oh, Y. Wang, Y.-H. Kim, H. Yan, R. Sinclair, D. Zhou, G. Xue, B. Murmann, C. Linder, W. Cai, J. B.-H. Tok, J. W. Chung, Z. Bao, *Science* **2017**, *355*, 59.
[21] J. Xu, H.-C. Wu, C. Zhu, A. Ehrlich, L. Shaw, M. Nikolka, S. Wang, F. Molina-Lopez, X. Gu, S. Luo, D. Zhou, Y.-H. Kim, G.-J. N. Wang, K. Gu, V. R. Feig, S. Chen, Y. Kim, T. Katsumata, Y.-Q. Zheng, H. Yan, J. W. Chung, J. Lopez, B. Murmann, Z. Bao, *Nat. Mater.* **2019**, *18*, 594.
[22] S. Nikzad, H.-C. Wu, J. Kim, C. M. Mahoney, J. R. Matthews, W. Niu, Y. Li, H. Wang, W.-C. Chen, M. F. Toney, M. He, Z. Bao, *Chem. Mater.* **2020**, *32*, 897.
[23] M. Kaltenbrunner, M. S. White, E. D. Głowacki, T. Sekitani, T. Someya, N. S. Sariciftci, S. Bauer, *Nat. Commun.* **2012**, *3*, 770.
[24] J. Mun, J. Kang, Y. Zheng, S. Luo, Y. Wu, H. Gong, J.-C. Lai, H.-C. Wu, G. Xue, J. B.-H. Tok, Z. Bao, *Adv. Electron. Mater.* **2020**, *6*, 2000251.
[25] J. Mun, J. Kang, Y. Zheng, S. Luo, H.-C. Wu, N. Matsuhisa, J. Xu, G.-J. N. Wang, Y. Yun, G. Xue, J. B.-H. Tok, Z. Bao, *Adv. Mater.* **2019**, *31*, 1903912.
[26] J. Xu, H.-C. Wu, J. Mun, R. Ning, W. Wang, G.-J. N. Wang, S. Nikzad, H. Yan, X. Gu, S. Luo, D. Zhou, J. B.-H. Tok, Z. Bao, *Adv. Mater.* **2022**, *34*, 2104747.

[27] M. Nikolka, I. Nasrallah, B. Rose, M. K. Ravva, K. Broch, A. Sadhanala, D. Harkin, J. Charmet, M. Hurhangee, A. Brown, S. Illig, P. Too, J. Jongman, I. McCulloch, J.-L. Bredas, H. Sirringhaus, *Nat. Mater.* **2017**, *16*, 356.
[28] L. Qiu, X. Wang, W. H. Lee, J. A. Lim, J. S. Kim, D. Kwak, K. Cho, *Chem. Mater.* **2009**, *21*, 4380.
[29] Y. Lei, P. Deng, J. Li, M. Lin, F. Zhu, T.-W. Ng, C.-S. Lee, B. S. Ong, *Sci. Rep.* **2016**, *6*, 24476.
[30] Z. He, Z. Zhang, S. Bi, *Mater. Adv.* **2022**, *3*, 1953.
[31] S. Goffri, C. Müller, N. Stingelin-Stutzmann, D. W. Breiby, C. P. Radano, J. W. Andreasen, R. Thompson, R. A. J. Janssen, M. M. Nielsen, P. Smith, H. Sirringhaus, *Nat. Mater.* **2006**, *5*, 950.
[32] Y.-Q. Zheng, Y. Liu, D. Zhong, S. Nikzad, S. Liu, Z. Yu, D. Liu, H.-C. Wu, C. Zhu, J. Li, H. Tran, J. B.-H. Tok, Z. Bao, *Science* **2021**, *373*, 88.
[33] Y. Lee, J. Y. Oh, W. Xu, O. Kim, T. R. Kim, J. Kang, Y. Kim, D. Son, J. B.-H. Tok, M. J. Park, Z. Bao, T.-W. Lee, *Sci. Adv.* **2018**, *4*, eaat7387.
[34] W. Niu, H.-C. Wu, J. R. Matthews, A. Tandia, Y. Li, A. L. Wallace, J. Kim, H. Wang, X. Li, K. Mehrotra, Z. Bao, M. He, *Macromolecules* **2018**, *51*, 9422.
[35] Z. Wang, Z. Liu, L. Ning, M. Xiao, Y. Yi, Z. Cai, A. Sadhanala, G. Zhang, W. Chen, H. Sirringhaus, D. Zhang, *Chem. Mater.* **2018**, *30*, 3090.
[36] L. Qiu, W. H. Lee, X. Wang, J. S. Kim, J. A. Lim, D. Kwak, S. Lee, K. Cho, *Adv. Mater.* **2009**, *21*, 1349.
[37] Q.-Y. Li, Z.-F. Yao, J.-Y. Wang, J. Pei, *Rep. Prog. Phys.* **2021**, *84*, 076601.
[38] H. Yang, G. Zhang, J. Zhu, W. He, S. Lan, L. Liao, H. Chen, T. Guo, *J. Phys. Chem. C* **2016**, *120*, 17282.
[39] W. H. Lee, Y. D. Park, *Polymers* **2014**, *6*, 1057.
[40] L. J. Richter, D. M. DeLongchamp, A. Amassian, *Chem. Rev.* **2017**, *117*, 6332.
[41] Y. Ito, A. A. Virkar, S. Mannsfeld, J. H. Oh, M. Toney, J. Locklin, Z. Bao, *J. Am. Chem. Soc.* **2009**, *131*, 9396.
[42] M. Kirkus, L. Wang, S. Mothy, D. Beljonne, J. Cornil, R. A. J. Janssen, S. C. J. Meskers, *J. Phys. Chem. A* **2012**, *116*, 7927.
[43] F. C. Spano, *Acc. Chem. Res.* **2010**, *43*, 429.
[44] S. Wood, J. Wade, M. Shahid, E. Collado-Fregoso, C. Bradley, D. D. C. , J. R. Durrant, M. Heeney, J.-S. Kim, *Energy Environ. Sci.* **2015**, *8*, 3222.
[45] Y.-J. Kim, N.-K. Kim, W.-T. Park, C. Liu, Y.-Y. Noh, D.-Y. Kim, *Adv. Funct. Mater.* **2019**, *29*, 1807786.
[46] D. T. Duong, V. Ho, Z. Shang, S. Mollinger, S. C. B. Mannsfeld, J. Dacuna, M. F. Toney, R. Segalman, A. Salleo, *Adv. Funct. Mater.* **2014**, *24*, 4515.
[47] J. Y. Na, B. Kang, Y. D. Park, *J. Phys. Chem. C* **2019**, *123*, 17102.
[48] J. Rivnay, S. C. B. Mannsfeld, C. E. Miller, A. Salleo, M. F. Toney, *Chem. Rev.* **2012**, *112*, 5488.
[49] D. Choi, M. Chang, E. Reichmanis, *Adv. Funct. Mater.* **2015**, *25*, 920.
[50] H. Tran, V. R. Feig, K. Liu, H.-C. Wu, R. Chen, J. Xu, K. Deisseroth, Z. Bao, *ACS Cent. Sci.* **2019**, *5*, 1884.
[51] A. Dazzi, C. B. Prater, *Chem. Rev.* **2017**, *117*, 5146.
[52] K. Xu, W. Sun, Y. Shao, F. Wei, X. Zhang, W. Wang, P. Li, *Nanotechnol. Rev.* **2018**, *7*, 605.
[53] K. Zhao, O. Wodo, D. Ren, H. U. Khan, M. R. Niazi, H. Hu, M. Abdelsamie, R. Li, E.r. Q. Li, L. Yu, B. Yan, M. M. Payne, J. Smith, J. E. Anthony, T. D. Anthopoulos, S. T. Thoroddsen, B. Ganapathysubramanian, *Adv. Funct. Mater.* **2016**, *26*, 1737.
[54] D. Natali, M. Caironi, *Adv. Mater.* **2012**, *24*, 1357.
[55] D. K. Owens, R. C. Wendt, *J. Appl. Polym. Sci.* **1969**, *13*, 1741.
[56] S. Pang, R. Zhang, C. Duan, S. Zhang, X. Gu, X. Liu, F. Huang, Y. Cao, *Adv. Energy Mater.* **2019**, *9*, 1901740.
[57] P. J. Flory, *Principles of Polymer Chemistry*, Cornell University Press, Ithaca, NY **1953**.
[58] M. M. Coleman, C. J. Serman, D. E. Bhagwagar, P. C. Painter, *Polymer* **1990**, *31*, 1187.
[59] D. J. Gundlach, J. E. Royer, S. K. Park, S. Subramanian, O. D. Jurchescu, B. H. Hamadani, A. J. Moad, R. J. Kline, L. C. Teague, O. Kirillov, C. A. Richter, J. G. Kushmerick, L. J. Richter, S. R. Parkin, T. N. Jackson, J. E. Anthony, *Nat. Mater.* **2008**, *7*, 216.

ADVANCED FUNCTIONAL MATERIALS
www.afm-journal.de

Intrinsic Mechanical Compliance of 90° Domain Walls in $PbTiO_3$

*Cam-Phu Thi Nguyen, Peggy Schoenherr, and Jan Seidel**

Functionality of domain walls and other topological defects in ferroelectrics is being widely investigated for applications in electronic devices. While the intrinsic electronic properties of a wall have been considered, its inherent mechanical properties remain explored very little, despite the fact that coupling between strain and polarization is prevalent in many of these materials. Herein, an in-depth study of variations in nanomechanical properties at 90° domain walls and their adjacent domains in single-crystalline lead titanate ($PbTiO_3$) is presented as a prototypical ferroelectric material using a combination of various atomic force microscopy (AFM)-based methods. Considerable variations of elastic moduli are found at 90° domain walls extending up to ~100 nm into the domain areas. AFM nanoindentation also allows to extract local domain wall hardness and plastic and elastic deformation energies. These findings have implications for the design of ferroelectric domain wall functionality that incorporates the intrinsic elastic compliance of a domain wall.

1. Introduction

The study of domain walls in ferroelectrics and multiferroic materials has seen considerable interest over the last years, which in part is driven by their intrinsic different properties compared to the bulk material. Significant changes at domain walls range from altered electronic properties,[1,2] localized superconductivity,[3] and chemical changes,[4] to altered magnetism and magnetoelectric coupling in multiferroics.[5,6] Such altered properties make domain walls locally susceptible to external perturbations, such as light illumination, electric and magnetic fields, etc.[7] Because of their intrinsic width of only a few nanometers, they represent the ultimate functional features that can potentially be exploited for new concepts in information storage and processing, sensing, and actuating.[8]

Considering various types of domain walls found in ferroelectric systems, the ferroelastic 90° domain walls are interesting as they are formed due to the reorientation of the crystal structure. The rotation of the *c*-axis of the material by 90° causes the twinning of the material, and hence, 90° domain walls are also ferroelastic twin domain walls (twin boundaries). These ferroelastic domains exhibit intrinsic strain on both sides of the wall with the two sides of the 90° twin domain walls showing an intrinsic difference.[9] Thus, the mechanical properties of those twin domain walls are expected to be different compared to their surrounding domains. The functionality of such twin walls has been investigated using molecular dynamics simulation.[10–15] Zhao et al. argue that the intersection of the twin domains and twin boundaries shows elastic softening due to the existence of local strain profiles,[16,17] i.e., the walls associated with surface ridges, where the surface layer swells, are softer than the valley area. This effect relates to the surface deformation caused by the twin geometry shear. With the experimental results, some authors have investigated the mirror electron microscopy (MEM) method that showed the contrast between the dark lines at the valley and the bright lines at the ridge, reflecting different positive and negative surface charges near the domain walls.[18–20] The method confirmed that the twin walls are polar and piezoelectric. Nevertheless, the twin domains showed no contrast as those domains have the same surface charge. However, the MEM method is very sensitive and influenced by many factors, including polarity, surface topography, and charge, and hence, the results are prone to artifacts. Thus, there is still a lack of experimental research, especially regarding the mechanical properties of the twin walls compared to their surrounding domains.

The diversity of mechanical properties in ferroelectric domain walls directly depends on the type of domain wall. The sensitivity of atomic force microscopy (AFM) to mechanical properties, even though it has so far only detected induced mechanical change at 180° domain walls,[21] presents the possibilities for investigating multiple order parameters and phases of such complicated ferroic structures. For example, Stefani et al.[22] reported that the local stress induced due to the applied force on the AFM tip during the scanning process is associated

C.-P. T. Nguyen, P. Schoenherr, J. Seidel
School of Materials Science and Engineering
UNSW Sydney
Sydney, NSW 2052, Australia
E-mail: jan.seidel@unsw.edu.au
P. Schoenherr, J. Seidel
ARC Centre of Excellence in Future Low-Energy Electronics Technologies (FLEET)
UNSW Sydney
Sydney 2052, Australia
The ORCID identification number(s) for the author(s) of this article can be found under https://doi.org/10.1002/adfm.202211906.

DOI: 10.1002/adfm.202211906

with the "strain dip" and the local material deformation that led to a shift of 180° domain walls. The energy that needs to move domain walls is lower than that of the deformation of a domain, and hence, the domain wall shows a softness in mechanical properties. Another possible mechanism corresponds to the electrostatic energy of the deformation. The total polarization at the domain wall is zero, leading to zero electrostatic energy, thus making the material easier to deform in this region. Furthermore, a similar trend occurred in ferroelectric lead zirconate titanate ceramics, reported by Tsuji et al.[23,24] The authors show the contact stiffness of the domain wall was ≈10% lower than the surrounding domains using the ultrasonic atomic force microscopy (UAFM) method. The softening of the domain wall might be because the switching of the domain accompanies the domain wall movement. In general, the contact area between the AFM tip and sample in the UAFM method is smaller than the domain size, and, hence, it only represents a local polarization charge underneath. This may influence the piezoelectric stiffening of the domain. Moreover, the lattice spontaneous polarization is rotated at the domain wall, resulting in a smaller average polarization and stiffening at the domain wall compared to the domains.[24,25] However, those studies only reported the mechanical softening of 180° domain walls compared to their surrounding domains. Thus, more comprehensive studies that focus on the behavior of 90° domain walls compared to their surrounding domains are still needed as well as the use of different AFM modes to access the intrinsic mechanical properties to investigate the big picture of the mechanical properties of the ferroelectric PTO single crystal.

In this work, we determine the local mechanical properties as well as polarization and topography corresponding to *a* and *c* domains separated by 90° twin domain walls in lead titanate as a prototypical ferroelectric material. To access these individual domain wall structures with widths of 1–10 nm[9,26–28] we use AFM-based methods to determine their local elastic moduli, hardness, and plastic and elastic deformation energies; these methods include contact resonance force microscopy (CRFM), force-distance maps (F–D maps), and AFM-based nanoindentation using solid diamond probes.

2. Results and Discussion

Figure 1a shows a typical 3D topography and Figure 1b shows the corresponding polarization image acquired by PFM of our $PbTiO_3$ crystal containing *a* and *c* domain structures. The stripe-like structure is a result of a zig-zag pattern from the *a* and *c* domains. The ridges and valleys have an angle that differs by 3° from 180° which is similar to previous reports of such twins.[29–31] The difference between *a* and *c* domains is a rotation of the *c*-axis of the material by 90°. This leads to the twinning of the material and twin boundaries separating *a* and *c* domains. Due to the ferroelectric properties of the material, each domain has a distinct polarization direction. The PFM phase image shows different contrast in the stripes

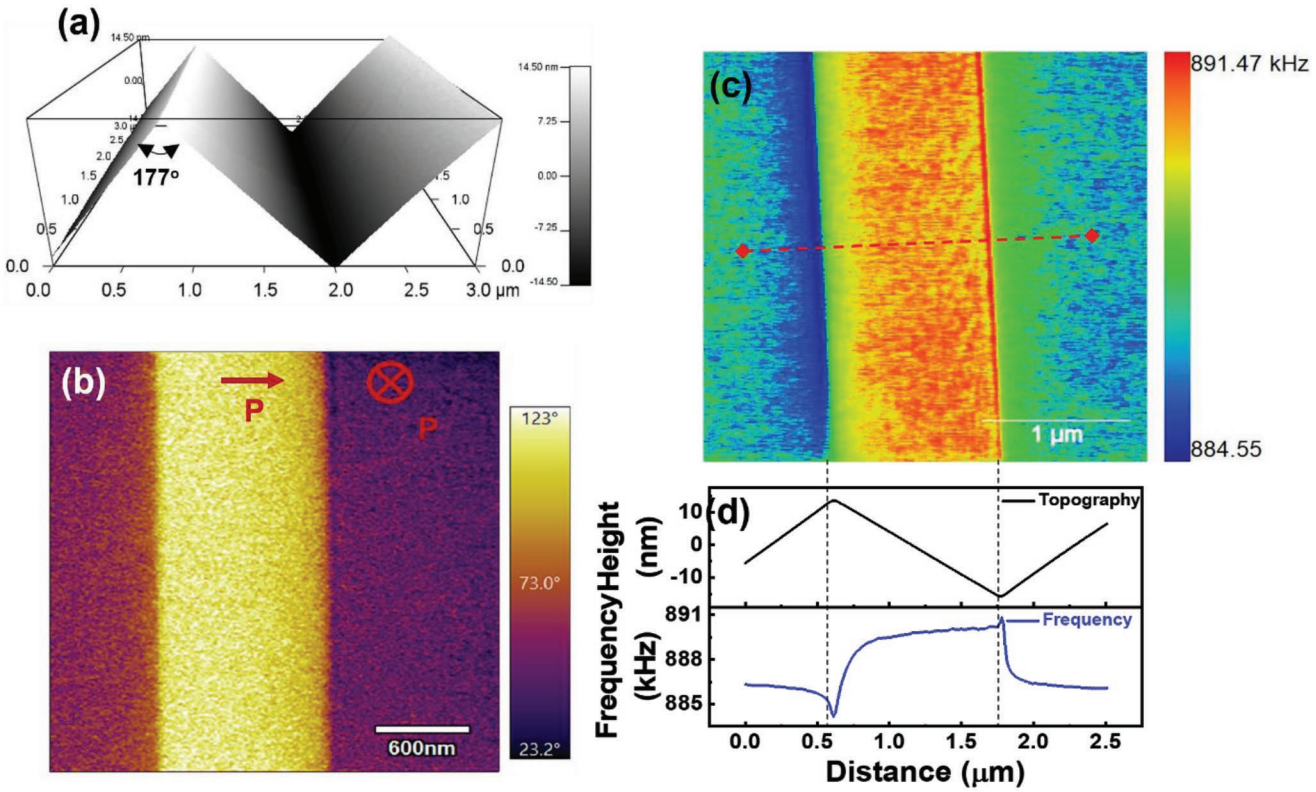

Figure 1. a) Topography of $PbTiO_3$ presented in 3D. The angle between the *a* and *c* domains is ≈ 177°. b) Vertical PFM phase images of 90° *a*–*c* domains. c) Contact-resonant force microscopy map, d) Horizontal line cut along the red line in the image c) additional to the topography line cut at the same location.

corresponding to in- and out-of-plane polarization belonging to the *a* and *c* domains, respectively, and that the twin boundaries coincide with the ferroelectric domain walls.

In the next step, we investigate the mechanical properties of the *a*- and *c*-domains and the twin boundaries separating them. To access the small scales of the twin boundaries we use CRFM which has been shown to reveal mechanical properties on the nanometer scale.[32–34] CRFM detects changes in the resonance frequency of the AFM cantilever which correspond to changes in sample stiffness. Figure 1c shows our CRFM results generated by mechanically exciting the sample with an actuator. The CRFM image is at the same location as the images in Figure 1a,b. The CRFM image shows a clear domain contrast with higher frequencies in the in-plane polarized areas (orange-red contrast) than in the out-of-plane areas (green-blue areas). A higher resonance frequency corresponds to a higher elastic modulus, which shows that the in-plane polarized areas are mechanically harder. This agrees with our other measurements and further literature. Additional CRFM contrast can be found at the twin domain boundaries with a higher contact resonance frequency at the valleys and a lower signal at the ridges compared to the domains. Figure 1d shows a line cut along the red line in Figure 1c (average over 50 lines) with an additional topography line cut at the same location that highlights the changes in CRFM signal in the domains and twin boundaries. The contact resonance frequency values in the line cut have been converted to elastic modulus values following the method by D. C. Hurley.[32–34] The elastic modulus of the in-plane and out-of-plane domains are 58.6 ± 3.8 GPa and 48.3 ± 3.6 GPa, respectively. The ridge domain boundary has the lowest elastic modulus of 43.5 ± 1.8 GPa whereas the valley boundary reaches the highest value of 60.7 ± 4.2 GPa. This is a difference in elastic modulus between the twin boundaries of 17.2 GPa (28.4%). When comparing the elastic modulus value to the topography we observe that the highest and lowest values are exactly at the ridge and valley, but their impact extends up to 100 nm into the domain. These mechanical changes at the boundaries thus stretch much further than the width of the twin boundaries. As CRFM measurements are very sensitive to topography and the tip-surface contact area, it is important to exclude any impact from the zig-zag pattern on the elastic modulus changes. A recent paper showed that their CRFM measurements were impacted by the topography, where a valley-like structure led to an increase of 20% in elastic modulus at the bottom of a dip due to an increase in tip-surface contact.[35] Compared to our measurements (an elastic modulus increase of 3.6% in the valley boundary compared to the in-plane domain), their topography had a tilt angle of 30° whereas ours only has a change in slope by 3° (see Figure 1a), which thus does not explain the increase in elastic modulus at our valleys. Additionally, our increase of elastic modulus at the twin boundaries extends much further than the tip radius. Thus, we can conclude that our elastic modulus changes at the domain boundary are not purely induced by the topography but are due to intrinsic material properties or other contributions.

Further mechanical measurements were done at the twin boundaries to support our CRFM findings. **Figure 2** shows our mechanical results from the force-distance curves. Figure 2a,b shows the height maps of a ridge (left) and a valley (right), whereas Figure 2c,d depicts the corresponding elastic modulus maps. Those maps are determined by force-distance curves taken over a grid of 60 × 60 points with a loading force of 1000 nN. The elastic modulus is determined by fitting all force-distance curves using the Hertzian model which is embedded in the Asylum software (version 16.05.193). The elastic modulus values of the in-plane domain (blue contrast) are higher than the out-of-plane domain (red contrast) as seen in both elastic modulus maps c) and d). The average elastic modulus of the in- and out-of-plane domains are 63.0 ± 4.7 GPa and 50.3 ± 3.1 GPa, respectively, and are determined by fitting the histograms extracted from the elastic modulus maps (histograms in Figure 2g,h).

As in the CRFM measurements, there is an additional contrast at the twin boundaries. To extract the signal at the boundary, Figure 2e,f shows the line cuts across the height (white line) and force curve maps (black line). A clear contrast in elastic modulus can be seen between the ridge (red) and valley (blue/white) compared to the surrounding areas whereas the ridge has the smallest elastic modulus of 44.3 ± 4.4 GPa and the valley shows the highest value of 67.5 ± 5.9 GPa (values are determined by fitting the histograms). These results are consistent with the trend observed in the CRFM measurements.

After generating consistent measurement results with two different AFM modes, we wanted to test what results in a more invasive method would give. AFM-based nanoindentation is thus used to also determine hardness (*H*) and elastic modulus (*E*) values of the *a* and *c* domains, as well as the twin walls. **Figure 3**a shows the $PbTiO_3$ surface topography before and after applying a loading force of 30 µN with indentations in the domains as well as at the twin boundaries. The topography profile extracted along the black arrow in Figure 3a is depicted in Figure 3b and clearly shows the ridge and valley structure of our measurement area. The *H* and *E* values are extracted by the Oliver-Pharr and Hertz models from the nanoindentation load-displacement curves.[36,37] The hardness and elastic modulus of the in-plane domain (*a* domain) in Figure 3c are larger than the out-of-plane domain (*c* domain) with $H = 6.6 \pm 0.4$ GPa and $E = 71.9 \pm 2.5$ GPa compared to $H = 5.5 \pm 0.3$ GPa and $E = 54.2 \pm 1.5$ GPa. This is the same trend as for the CRFM and FM measurements. However, both the ridge and valley boundaries exhibit different properties than in the other experiments where they both have similar values of $H = 6.6 \pm 0.6$ GPa and $E = 71.7 \pm 2.5$ GPa (ridge) and $H = 6.7 \pm 0.5$ GPa and $E = 73.3 \pm 1.5$ GPa (valley).

Furthermore, nanoindentation allows for the extraction of energy scales related to plastic and elastic deformations (U_P and U_E). The results are shown in Figure 3d (calculations are given in our last study[38]). Similar to the mechanical values, the in-plane domain has similar values to the twin boundaries independent if it is at a ridge or valley with $U_P = 0.84 \pm 0.13 \times 10^{-4}$ nJ, $0.82 \pm 0.19 \times 10^{-4}$ nJ, $0.85 \pm 0.17 \times 10^{-4}$ nJ, and $U_E = 2.46 \pm 0.22 \times 10^{-4}$ nJ, $2.51 \pm 0.25 \times 10^{-4}$ nJ, $2.52 \pm 0.12 \times 10^{-4}$ nJ, respectively. In contrast, the out-of-plane domains have higher plastic energies ($1.64 \pm 0.21 \times 10^{-4}$ nJ) and lower elastic energies ($2.00 \pm 0.29 \times 10^{-4}$ nJ) indicating that the out-of-plane domains have a higher plastic deformation and thus lower hardness/stiffness compared to the other areas.

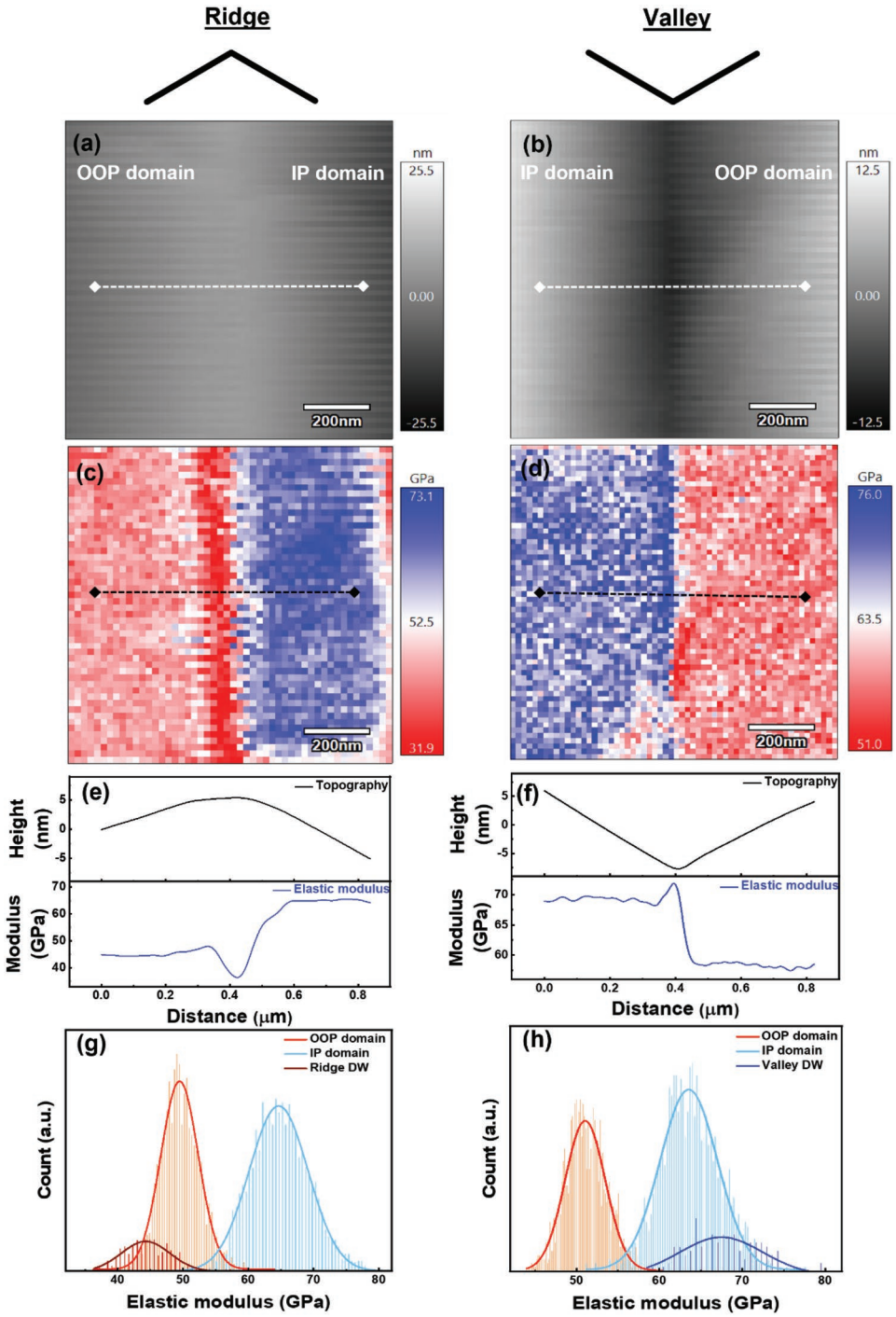

Figure 2. a,b) Height mapping, c,d) elastic modulus mapping by force-distance curves of a ridge and valley. e,f) Horizontal line cut along the white and black lines in the image a–d), respectively. g,h) Histogram corresponding to the elastic maps in c,d), respectively.

To compare and get a better understanding of the mechanical measurements all elastic modulus values are summarized in **Table 1**. in addition to the energy values from the nanoindentation shown in **Table 2**. For the domain walls, only the results of the CRFM and FM are in agreement with each other, showing low elastic modulus values for the ridges and high values for the valleys whereas the nanoindentation shows similar values for both twin boundaries and in-plane domain. The main reason for that could be the difference in measuring mode, where both CRFM and FM only press onto the surface without changing it compared to the permanent indents the indentation induces. Moreover, the nanoindentation technique involves the mechanical measurement at local area of the material while the other methods scan across the sample surface,

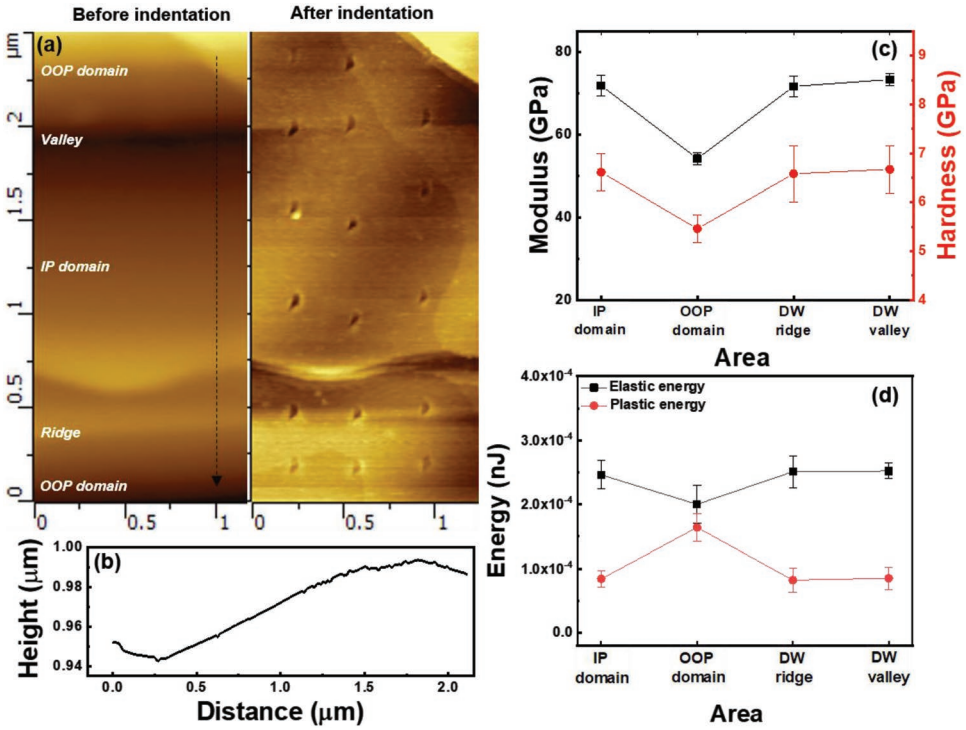

Figure 3. a) Topography of $PbTiO_3$ before and after indentation at 30 μN. b) Vertical line cut along the black arrow in a) to show the zig-zag topography. c) elastic modulus and hardness; d) corresponding elastic and plastic energies of the IP and OOP domains, and ridge and valley DWs.

and the elastic moduli are calculated from the mapping histogram. Those results might lead to the difference in elastic modulus between nanoindentation and CRFM/FM methods. Even though we would expect different elastic modulus values at the domain walls due to the intrinsic strain, it is surprising that they are so different at the ridges and valleys. It occurs that the polarization on both sides of the domain walls is different. Therefore, the intrinsic strain which influences the ridges and valleys walls is also different.

Additionally, as Zhao et al. reported,[16,17] the difference in elastic modulus of ridge and valley domains is associated with the surface deformation by the twin geometry shear. Another reason for the elastic modulus difference could come from the fact that the domain walls are not vertical but are tilted by ≈ 45° (see **Figure 4**d) to the surface. This means that when measuring a domain wall, additional contributions from the domain below could impact the results.

To determine if the tilt of the domain walls has an impact on the measured elastic modulus values, we also looked at 90° domains on another facet of the crystal where two in-plane polarizations meet under a 90° angle, and the domain wall is vertical to the surface. The topography of $PbTiO_3$ on the new facet has no zigzag shape, as shown in Figure 4a. The schematic in Figure 4b shows the *a1/a2* domains structure on the front polarization structure of the new facet. It depicts that the polarization is fully in-plane and at an angle of 90° to each other with the domain walls perpendicular to the surface. The corresponding off-resonance PFM phase signals are presented in Figure 4c,d. As expected, there is almost no contrast in the vertical PFM image with small differences that can be associated with buckling of the cantilever (buckling: an in-plane signal can lead to buckling of the cantilever and thus show up as an out-of-plane signal in the measurement). However, as seen by the lateral PFM image (Figure 4d), the area has predominantly in-plane polarization. White arrows indicate the orientation of the in-plane polarization with the domain walls being 90°. The results indicate that the new facet has in-plane polarization with *a1/a2* domains.

Mechanical measurements are done by CRFM and FM and are shown in Figure 4e,f. Both images are very similar with the main contrast coming from the topography (horizontal lines)

Table 1. Summary of experimentally determined elastic modulus values from different measurement methods.

Specific area	Elastic modulus [GPa]		
	CRFM	FM	Nanoindentation
IP domain	58.6 ± 3.8	63.0 ± 4.7	71.9 ± 2.5
OOP domain	48.3 ± 3.6	50.3 ± 3.1	54.2 ± 1.5
DW ridge	43.5 ± 1.8	44.3 ± 4.4	71.7 ± 2.5
DW valley	60.7 ± 4.2	67.5 ± 5.9	73.3 ± 1.5

Table 2. Mechanical parameters extracted from nanoindentation measurement.

Specific area	Elastic energy [nJ]	Plastic energy [nJ]
IP domain	$2.46 \pm 0.22 \times 10^{-4}$	$0.84 \pm 0.13 \times 10^{-4}$
OOP domain	$2.00 \pm 0.29 \times 10^{-4}$	$1.64 \pm 0.21 \times 10^{-4}$
DW ridge	$2.51 \pm 0.25 \times 10^{-4}$	$0.82 \pm 0.19 \times 10^{-4}$
DW valley	$2.52 \pm 0.12 \times 10^{-4}$	$0.85 \pm 0.17 \times 10^{-4}$

and a few additional spots that align with the dark and bright spots in the vertical PFM image. However, there is no contrast difference between the *a1/a2* domains and domain in both the CRFM image and elastic maps. As discussed in previous reports,[22–24] there is no change in elastic modulus across the in-plane domains and domain walls in CRFM measurements. The domain wall softening is anisotropic as the mechanical resonance frequency is lower in c domains (out-of-plane polarization) but unchanged in the same in-plane polarization across the *a* domains. Interestingly, the elastic maps show a similar trend to the CRFM measurements, as there is no obvious signal across the *a1/a2* domains and domain walls. As both CRFM and FM induce a considered pressure onto the sample surface, especially FM, the mechanical response should be similar in both techniques. Zhao et al.[16] designed molecular dynamics simulations with two ionic sublattices for 2 × 3 lattice units to derive surface polarity at the ferroelastic 90° and 45° domain boundaries. They identified that three main factors affect the surface polarity, including charge, geometry, and dipoles. The intersection of the twin domains and twin boundaries contains elastic softening due to the existence of local strain profiles.[16,17] The walls associated with ridges, where the surface layer swells, are softer than the valley area. This effect relates to the surface deformation caused by the twin angle's geometry shear. In the case of *a1/a2* twin configuration, and a surface with no ridge and valley structure existing, all dipoles are parallel to the surface and give rise to the in-plane polarization. This result is in good agreement with our experiment in Figure 4d which presents in-plane in polarization in *a1/a2* domains.

After finishing elastic modulus measurements on all kinds of different domain walls in PTO, we realized that especially the AFM-based nanoindentation experiments deviated from the CRFM and FM measurements (only at the domain walls). Thus, we wanted to investigate the propagation behavior (dislocation and cracks) of the indentation in the material to see if we can find further insight. Figure S4 (Supporting Information) shows our HRTEM results with two indents marked by arrows in Figure S4a (Supporting Information). The interface of the Pt layer and the PTO crystal is indicated by the darker line in the HRTEM image (the dark line is a thin graphene layer to increase the adhesion between the Pt and PTO). The thickness of the impacted PTO region is ≈ 280 nm, which includes two main areas: 1) Dense region of defects with high stacking fault density and some cracking with a thickness of ≈ 130 nm, and 2) sparse region of defects (thickness of 150 nm) with dislocations and stacking faults in the {110} planes. There are no defects below 280 nm (area 3)). This can be seen in the zoomed-in area of Figure S4a (Supporting Information) marked by the red dotted square and shown in Figure S4b (Supporting Information). The HRTEM image shows stacking faults on {100} and {110} planes and extended dislocation with several micro-crack regions, suggesting an extensive amount of affected area below the indented area. A confirmation of the extent of deformation the indents induce is shown in the diffraction pattern in Figure S4c (Supporting Information). There is an angle of 4.6° between the diffraction pattern of the original crystal structure to additional diffraction points coming from the distortions of the indent. This amount of impact from the indents to a depth of 280 nm as well as to a lateral extension of ≈500 nm is large

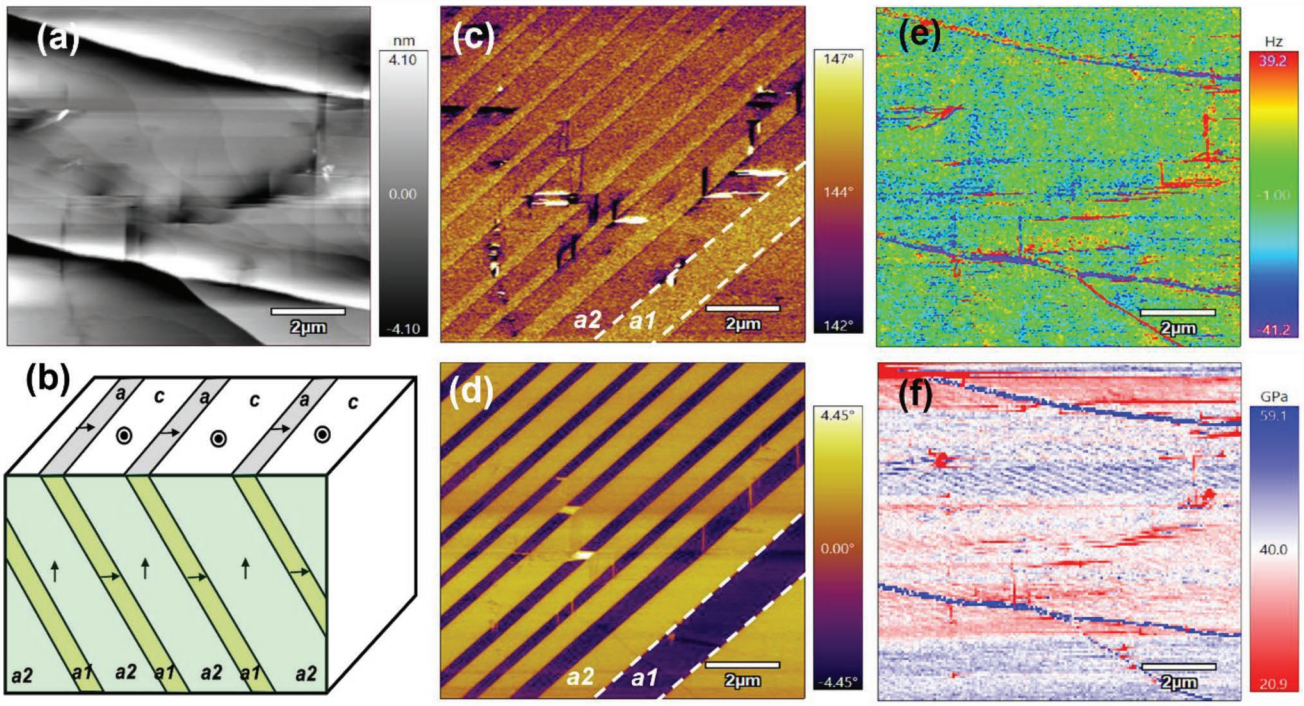

Figure 4. a) Topography, b) Schematic diagram of the *a1/a2* domains of $PbTiO_3$ single crystal in different facets (green tinted facet is the measured one here). c,d) Vertical and lateral off-resonance PFM phase signals, e) CRFM, and f) Elastic map at the same location in a) another facet of the $PbTiO_3$ sample.

compared to their size of 200 nm in width and 30 nm in depth. An indent at the domain wall thus impacts large sections of the wall and its surroundings leading to a shift or destruction of the domain wall. This large-scale impact is also different from CRFM and FM, and could explain the vast differences in results.

3. Conclusion

The study of mechanical properties of ferroelectric materials using various investigative methods based on the SPM measurements provides a unique tool to access these material structures at the nanometer scale. The sensitivity and selectivity of AFM techniques open new pathways for characterizing the numerous order parameters and phases of the ferroic materials' complex structure. This work presents the difference in mechanical properties at the domain walls compared to their surrounding domains. The validity of the experiments is strengthened by the combination of three different AFM-based methods to compare and verify our results. A clear contrast in CRFM and elastic modulus maps can be seen between the *a* and *c* domains, the ridge and valley domain walls, and the *a*/*c* domains and DWs. We observe that the *a* domains have higher modulus compared to the *c* domains, while the highest and lowest elastic modulus values are at the ridge and valley DWs. On the contrary, the AFM-based nanoindentation shows the similarity in elastic moduli in *a* domain and both DWs and the lowest elastic modulus in the *c* domain. The increase of elastic modulus at the valley DWs can be detected up to 100 nm away from the valley, which is larger than the tip radius. Thus, we can conclude that our elastic modulus changes at the domain boundaries are not a measurement artifact. Moreover, the CRFM and elastic map that are measured on another facet do not show any contrast between the domains and domain walls. Overall, our work shows the complexity of mechanical behavior at domain walls and the need for further investigations to fully understand its mechanism.

4. Experimental Section

Lead titanate ($PbTiO_3$) single crystals were grown from PbO and TiO_2 precursors (Sigma-Aldrich, high-purity 5N (99.999%). The precursors had been first ground to powder in an agate mortar. The mixture of PbO and TiO_2 powder was then synthesized in a sealed quartz crucible at a pressure of 10^{-6} mbar in a horizontal muffle for 48 h at 850 °C. The $PbTiO_3$ powder was then put into a platinum crucible with additional PbO in molar ratios of 1:1 to 1:3. The crucible was covered to avoid PbO evaporation during crystal growth. The whole system was then placed in a cubic muffle furnace and heated up to 1200 °C in 10 h and cooled down to 550 °C for a duration of 60 h. Further cooling to room temperature was performed at a cooling rate of 1 °C h^{-1} to avoid cracking at the phase transition from cubic to tetragonal (490 °C).[39–41] Finally, hot acetic acid was used to disassemble the single crystal $PbTiO_3$ from the PbO molten mass.

Surface morphology and PFM measurements were conducted using an Asylum Infinity SPM system with Ir/Ti coating silicon probes with a spring constant of k = 3.7 N m^{-1} (ASYELEC 01-R2). To determine the IP and OOP polarization, the lateral and vertical PFM signals (LPFM and VPFM, respectively) off-resonance (47.77 – 77.77 kHz) were detected using an AC voltage of 7 V. Out and in-plane PFM signals were confirmed on a standard PPLN ($LiNbO_3$) sample, as shown in Figure S1 (Supporting Information). Both VPFM and LPFM were performed off-resonance to determine the polarization direction of the PPLN domains. The CRFM experiments were performed using uncoated AC160TSA-R3 silicon probes with a spring constant of k = 33 N m^{-1} (Asylum Research, USA). The F–D maps and AFM-based nanoindentation experiments were performed using an NM-RC-C diamond probe with a force constant k = 470 N m^{-1} (Bruker, USA). The precise spring constant of each cantilever was determined using the thermal-noise technique[42,43] and the values were mentioned in the result section for each measurement. To determine the accuracy of the mechanical characteristics of each cantilever, the cantilevers were calibrated on a PPLN sample (CRFM measurement) and a fused-silica standard sample (*F–D* curve and nanoindentation), the detailed calibration results were summarized in the Supporting Information.

Supporting Information

Supporting Information is available from the Wiley Online Library or from the author.

Acknowledgements

The authors acknowledge support by the Australian Research Council through Discovery Grants and the ARC Centre of Excellence in Future Low Energy Electronics Technologies (FLEET). C.P.T.N. acknowledges support from an Australian Government Research Training Program Scholarship.

Open access publishing facilitated by University of New South Wales, as part of the Wiley - University of New South Wales agreement via the Council of Australian University Librarians.

Conflict of Interest

The authors declare no conflict of interest.

Data Availability Statement

The data that support the findings of this study are available from the corresponding author upon reasonable request.

Keywords

domain walls, ferroelectrics, mechanical properties, scanning probe microscopy

Received: October 14, 2022
Revised: November 15, 2022
Published online: January 17, 2023

[1] J. Seidel, L. W. Martin, Q. He, Q. Zhan, Y.-H. Chu, A. Rother, M. E. Hawkridge, P. Maksymovych, P. Yu, M. Gajek, N. Balke, S. V. Kalinin, S. Gemming, F. Wang, G. Catalan, J. F. Scott, N. A. Spaldin, J. Orenstein, R. Ramesh, *Nat. Mater.* **2009**, *8*, 229.
[2] P. S. Bednyakov, B. I. Sturman, T. Sluka, A. K. Tagantsev, P. V. Yudin, *NPJ Comput. Mater.* **2018**, *4*, 65.

[3] A. Aird, E. K. H. Salje, *J. Phys.: Condens. Matter* **1998**, *10*, L377.
[4] S. Farokhipoor, C. Magén, S. Venkatesan, J. Íñiguez, C. J. M. Daumont, D. Rubi, E. Snoeck, M. Mostovoy, C. De Graaf, A. Müller, M. Döblinger, C. Scheu, B. Noheda, *Nature* **2014**, *515*, 379.
[5] Y. Geng, N. Lee, Y. J. Choi, S. W. Cheong, W. Wu, *Nano Lett.* **2012**, *12*, 6055.
[6] M. Giraldo, Q. N. Meier, A. Bortis, D. Nowak, N. A. Spaldin, M. Fiebig, M. C. Weber, T. Lottermoser, *Nat. Commun.* **2021**, *12*, 3093.
[7] F. Rubio-Marcos, A. Del Campo, P. Marchet, J. F. Fernández, *Nat. Commun.* **2015**, *6*, 6594.
[8] P. Sharma, P. Schoenherr, J. Seidel, *Materials* **2019**, *12*, 2927.
[9] B. Meyer, D. Vanderbilt, *Phys. Rev. B* **2002**, *65*, 104111.
[10] Y. Frenkel, N. Haham, Y. Shperber, C. Bell, Y. Xie, Z. Chen, Y. Hikita, H. Y. Hwang, E. K. H. Salje, B. Kalisky, *Nat. Mater.* **2017**, *16*, 1203.
[11] H. Yokota, H. Usami, R. Haumont, P. Hicher, J. Kaneshiro, E. K. H. Salje, Y. Uesu, *Phys. Rev. B* **2014**, *89*, 144109.
[12] H. Yokota, S. Matsumoto, E. K. H. Salje, Y. Uesu, *Phys. Rev. B* **2018**, *98*, 104105.
[13] L. Goncalves-Ferreira, S. A. T. Redfern, E. Artacho, E. K. H. Salje, *Phys. Rev. Lett.* **2008**, *101*, 097602.
[14] J. F. Scott, E. K. H. Salje, M. A. Carpenter, *Phys. Rev. Lett.* **2012**, *109*, 187601.
[15] G. F. Nataf, M. Guennou, J. M. Gregg, D. Meier, J. Hlinka, E. K. H. Salje, J. Kreisel, *Nat. Rev. Phys.* **2020**, *2*, 634.
[16] Z. Zhao, N. Barrett, Q. Wu, D. Martinotti, L. Tortech, R. Haumont, M. Pellen, E. K. H. Salje, *Phys. Rev. Mater.* **2019**, *3*, 043601.
[17] E. K. H. Salje, *Minerals* **2021**, *11*, 478.
[18] G. F. Nataf, M. Guennou, J. Kreisel, P. Hicher, R. Haumont, O. Aktas, E. K. H. Salje, L. Tortech, C. Mathieu, D. Martinotti, N. Barrett, *Phys. Rev. Mater.* **2017**, *1*, 074410.
[19] G. F. Nataf, P. Grysan, M. Guennou, J. Kreisel, D. Martinotti, C. L. Rountree, C. Mathieu, N. Barrett, *Sci. Rep.* **2016**, *6*, 33098.
[20] N. Barrett, J. Dionot, D. Martinotti, E. K. H. Salje, C. Mathieu, *Appl. Phys. Lett.* **2018**, *113*, 022901.
[21] K. Cordero-Edwards, N. Domingo, A. Abdollahi, J. Sort, G. Catalan, *Adv. Mater.* **2017**, *29*, 1702210.
[22] C. Stefani, L. Ponet, K. Shapovalov, P. Chen, E. Langenberg, D. G. Schlom, S. Artyukhin, M. Stengel, N. Domingo, G. Catalan, *Phys. Rev. X* **2020**, *10*, 041001.
[23] T. Tsuji, H. Ogiso, J. Akedo, S. Saito, K. Fukuda, K. Yamanaka, *Jpn. J. Appl. Phys.* **2004**, *43*, 2907.
[24] T. Tsuji, S. Saito, K. Fukuda, K. Yamanaka, H. Ogiso, J. Akedo, Y. Kawakami, *Appl. Phys. Lett.* **2005**, *87*, 071909.
[25] P. Avouris, B. Bhushan, D. Bimberg, K. von Klitzing, H. Sakaki, R. Wiesendanger, *Acoustic Scanning Probe Microscopy* (Eds.: F. Marinello, D. Passeri, E. Savio), Springer, Berlin, Heidelberg **2013**.
[26] R. K. Behera, C.-W. Lee, D. Lee, A. N. Morozovska, S. B. Sinnott, A. Asthagiri, V. Gopalan, S. R. Phillpot, *J. Phys.: Condens. Matter* **2011**, *23*, 175902.
[27] T. Shimada, S. Tomoda, T. Kitamura, *J. Phys.: Condens. Matter* **2010**, *22*, 355901.
[28] J. Park, J. Mangeri, Q. Zhang, M. H. Yusuf, A. Pateras, M. Dawber, M. V. Holt, O. G. Heinonen, S. Nakhmanson, P. G. Evans, *Nanoscale* **2018**, *10*, 3262.
[29] Y. G. Wang, J. Dec, W. Kleemann, *J. Appl. Phys.* **1998**, *84*, 6795.
[30] P. Lehnen, J. Dec, W. Kleemann, *J. Phys. D: Appl. Phys.* **2000**, *33*, 1932.
[31] H. Okino, T. Ida, H. Ebihara, H. Yamada, K. Matsushige, T. Yamamoto, *Jpn. J. Appl. Phys.* **2001**, *40*, 5828.
[32] D. C. Hurley, *Applied Scanning Probe Methods XI*, Springer, Berlin, Heidelberg **2009**, pp. 97–138.
[33] D. C. Hurley, M. Kopycinska-Müller, E. D. Langlois, A. B. Kos, N. Barbosa, *Appl. Phys. Lett.* **2006**, *89*, 021911.
[34] D. C. Hurley, M. Kopycinska-Müller, A. B. Kos, R. H. Geiss, *Meas. Sci. Technol.* **2005**, *16*, 2167.
[35] X. Zhou, H. Miao, F. Li, *Nanoscale* **2013**, *5*, 11885.
[36] W. C. Oliver, G. M. Pharr, *J. Mater. Res.* **2004**, *19*, 3.
[37] W. C. Oliver, G. M. Pharr, *J. Mater. Res.* **1992**, *7*, 1564.
[38] C.-P. T. Nguyen, P. Schoenherr, L. Juli, J. Seidel, *Nanoscale* **2021**, *13*, 16959.
[39] C. C. Chou, C. M. Wayman, *Mater. Trans., JIM* **1992**, *33*, 306.
[40] G. Shirane, S. Hoshino, K. Suzuki, *Phys. Rev.* **1950**, *80*, 1105.
[41] N. Faraji, C. Yan, J. Seidel, *Appl. Phys Lett.* **2017**, *110*, 213108.
[42] J. P. Cleveland, S. Manne, D. Bocek, P. K. Hansma, *Rev. Sci. Instrum.* **1993**, *64*, 403.
[43] J. E. Sader, J. W. M. Chon, P. Mulvaney, *Rev. Sci. Instrum.* **1999**, *70*, 3967.